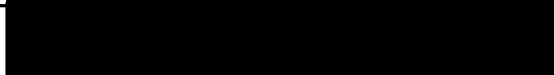


AN ABSTRACT OF THE THESIS OF

Kenneth Malcolm Glibert for the Ph. D. in Physics
(Name) (Degree) (Major)

Date thesis is presented November 16, 1965

Title GAMMA- AND BETA-RAY SPECTROSCOPY STUDIES OF THE
RADIOACTIVE DECAY OF Mn-51 TO Cr-51

Abstract approved 
(Major professor)

The decay scheme of Mn^{51} has been investigated using gamma-ray and beta-ray scintillation spectrometers and a fast coincidence spectrometer. A half-life value of 46.5 ± 0.2 minutes was determined for Mn^{51} which decays predominantly to the ground state of Cr^{51} by the emission of positons with an experimentally measured end-point energy of 2.21 ± 0.02 MeV. Weak branching to the 761-keV and 1170-keV levels of Cr^{51} , however, has been inferred from the measured 761 ± 11 -keV and 1170 ± 15 -keV gamma-ray energies observed in the Mn^{51} gamma-ray spectrum. Relative intensities for these weak gamma-rays have been determined experimentally as 0.70 ± 0.10 and 0.48 ± 0.12 percent of the positons, respectively. An 11 ± 1 nsec mean-life has been obtained for the 761-keV level of Cr^{51} while an upper-limit of 1 nsec has been given to the 1170-keV level. Using these experimental results coupled with theory, a spin and parity assignment of $\frac{5-}{2}$ was given to the ground state of Mn^{51} .

a spin assignment which is not in agreement with the $\frac{7^-}{2}$ value expected from the shell model prediction.

GAMMA- AND BETA-RAY SPECTROSCOPY STUDIES OF THE
RADIOACTIVE DECAY OF Mn-51 TO Cr-51

by

KENNETH MALCOLM GLIBERT

A THESIS

submitted to

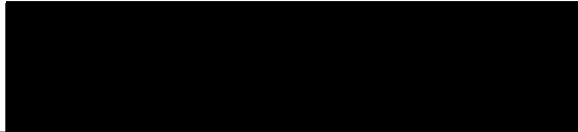
OREGON STATE UNIVERSITY

in partial fulfillment of
the requirements for the
degree of

DOCTOR OF PHILOSOPHY

June 1966

APPROVED:

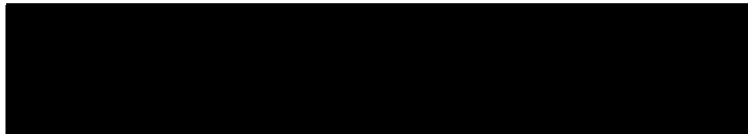


Associate Professor of Physics

In Charge of Major



Acting Chairman of the Department of Physics



Dean of the Graduate School

Date thesis is presented November 16, 1965

Typed by Marion F. Palmateer

ACKNOWLEDGMENTS

This author wishes to take this opportunity to express his gratitude to the following individuals whose kind and generous assistance made this investigation possible: (1) Dr. H. T. Easterday, research director and major professor, for proposing the problem and for the many enlightening discussions pertaining to all aspects of this investigation, (2) Dr. E. A. Yunker for his continued encouragement and support of the project, (3) Dr. R. W. Sommerfeldt for his assistance in measuring the mean-life times of the first two excited levels of Cr^{51} , (4) Mr. Thomas L. Yates and the staff of the Oregon State University Computing Laboratory and Mr. William Anderson and the staff of Western Data Processing Center, University of California, Los Angeles, California, for their assistance in the data analysis, (5) Mr. Jack McKenzie of the staff of the Oregon State University cyclotron for his help in producing the Mn^{51} isotope, and (6) Mr. Dale Weeden of the Oregon State University Physics Electronics shop for designing and constructing the dwell advance timer used in the half-life measurement and his conscientious attention to maintaining the electronic apparatus.

TABLE OF CONTENTS

	<u>Page</u>
INTRODUCTION	1
HALF-LIFE MEASUREMENT	11
Source Production	11
Apparatus	11
Experimental Results	15
GAMMA-RAY ENERGY MEASUREMENT	18
Apparatus	18
Experiment and Results	18
GAMMA-RAY RELATIVE INTENSITY MEASUREMENT	26
Apparatus	26
Experiment and Results	26
END-POINT ENERGY MEASUREMENT	40
Apparatus	40
Experiment and Results	43
MEAN-LIFE TIMES OF THE 761-keV AND 1170-keV LEVELS OF Cr-51	59
Apparatus	59
Experiment and Results	59
CONCLUSIONS	63
BIBLIOGRAPHY	84
APPENDICES	88
Appendix I Source Preparation	88
Appendix II Weighted Least Squares Fit Program	90
Appendix III Polynomial Curve Fitting	99
Appendix IV Backscatter Correction and Kurie Function Calculation	108

LIST OF FIGURES

<u>Figure</u>		<u>Page</u>
1	Decay scheme of Mn^{51} and the low-lying levels of Cr^{51} as summarized in the Nuclear Data Sheets.	9
2	Block diagram of a gamma-ray scintillation spectrometer.	13
3	Source-detector geometry for half-life analysis and gamma-ray energy measurement.	14
4	Decay curve for Mn^{51} .	16
5	Gamma-ray pulse-height spectra for energy calibration sources.	19
6	Energy calibration for gamma-ray pulse-height spectra.	21
7	Gamma-ray pulse-height spectrum for Mn^{51} .	22
8	Gamma-ray spectrum for Cs^{137} .	28
9	Peak-to-total ratios for a 7.6 x 7.6 cm NaI(Tl) crystal with a 10 cm source-to-detector distance.	29
10	Mn^{51} gamma-ray spectrum.	31
11	Y^{90} Bremsstrahlung distribution.	33
12	Gamma-ray spectra for Cs^{137} , Cr^{51} , Mn^{54} , and Zn^{65} sources.	34
13	Na^{22} gamma-ray spectrum.	35
14	Coincidence sum-spectrum for 511-keV annihilation radiation.	37
15	Block diagram of a beta-gamma coincidence spectrometer.	41

<u>Figure</u>		<u>Page</u>
16	Beta-ray spectra for Cs ¹³⁷ and Bi ²⁰⁷ and energy calibration.	44
17	Beta-ray coincidence spectrum for Cs ¹³⁷ K-conversion electrons and the fit of the response function R(E, E')	45
18	Beta-ray coincidence spectrum for Bi ²⁰⁷ 991-keV conversion electrons and the fit of the response function R(E, E').	48
19	Beta-ray coincidence spectrum for Bi ²⁰⁷ 499-keV conversion electrons and the fit of the response function R(E, E').	49
20	Kurie plots for P ³² with and without correcting the experimental spectrum for the detector response.	54
21	Kurie plots for Y ⁹⁰ with and without correcting the experimental spectrum for the detector response.	55
22	Mn ⁵¹ experimental beta-spectrum and the calculated true energy spectrum.	57
23	Mn ⁵¹ Kurie plot and energy calibration curve.	58
24	Delayed coincidence spectrum for the 761-keV level of Cr ⁵¹ and the prompt coincidence curve for Na ²² .	60
25	Delayed coincidence spectrum for the 1170-keV level of Cr ⁵¹ and the prompt coincidence curve for Na ²² .	62
26	Decay scheme for Mn ⁵¹ (present investigation).	66
27	Shell model nuclear level structure with spin-orbit coupling.	75
28	Comparison of experimentally determined half-lives for Mn ⁵¹ .	81

LIST OF TABLES

<u>Table</u>		<u>Page</u>
1	Experimentally determined half-life values of Mn ⁵¹ .	15
2	Experimental results of gamma-ray energy measurements of Mn ⁵¹ .	23
3	Relative intensities of the 761-keV and 1170-keV gamma-rays to the 511-keV annihilation radiation for Mn ⁵¹ .	39
4	Experimental results of the end-point energy measurement for Mn ⁵¹ .	56
5	Ratios of transition probabilities for electron capture and positron emission.	67
6	Branching intensities for transitions to the ground state and first two excited levels of Cr ⁵¹ .	69
7	Comparative half-periods and log ft values.	70
8	Theoretical branching intensities.	71
9	Theoretical mean-life times for the 761-keV and 1170-keV levels of Cr ⁵¹ for various gamma-ray multipolarities.	73
10	Ground state configurations for nuclei in the 1f _{7/2} region.	76

GAMMA- AND BETA-RAY SPECTROSCOPY STUDIES OF THE RADIOACTIVE DECAY OF Mn-51 TO Cr-51

INTRODUCTION

As the theory of nuclear level structure becomes increasingly refined, more precise and extensive knowledge concerning individual nuclei becomes necessary. The recent improvements in the experimental techniques used in low energy nuclear spectroscopy have provided means for examining nuclear properties with greater accuracy and for extending the number of nuclei available for investigation. In particular, the development of the multichannel analyzer has made feasible the investigation of the level structure of short-lived isotopes, whereas previously, scanning experiments were restricted to longer lived nuclei. As a result, a considerable amount of experimental information concerning the properties of low-lying nuclear levels has been accumulated in recent years. This information of course is utilized by the theoretician in refining existing nuclear models or in formulating new theories.

The atomic nucleus which consists of various discrete energy states is described by a set of nuclear properties. Some of these which characterize the nucleus are the half-life, the angular momentum of the ground state and excited levels, the magnetic dipole moment, the electric quadrupole moment, the relative parity, and

the energy and character of the nuclear transitions. Experimental low energy nuclear physics concerns itself with investigating and measuring these nuclear properties.

The vast amount of experimental information which has been gathered in recent years has been subjected to the test of several nuclear models. These models have been formulated in the absence of a complete understanding of the exact nature of the nuclear force existing between the nucleons within a nucleus. They are used to correlate the experimentally determined properties and hopefully can predict previously unknown nuclear parameters. One such model is the nuclear shell model which was conceived independently by Mayer, and by Haxel, Jensen, and Suess. This model is based on the assumption that the nucleons move independently in an average central potential $V(r)$ and furthermore are subjected to a strong inverted spin-orbit interaction proportional to $\vec{S} \cdot \vec{L}$ (Mayer and Jensen, 1955). Strong means that this interaction is an order of magnitude larger than that expected from the analogous spin-orbit interaction calculation for an electron (Eisberg, 1961) where the electron mass is replaced by the nucleon mass and the potential energy function is the total nuclear potential $V(r)$. Inverted spin-orbit interaction means that the nuclear energy is decreased when $\vec{S} \cdot \vec{L}$ is positive and is increased when it is negative in contrast to the opposite situation for the electron interaction energy. The shell

model was formulated originally to explain the magic numbers and their consequences. In addition, however, it is able to explain the spin angular momentum of the ground state of almost all odd A nuclei. The investigation of the decay of Mn^{51} was performed as an additional test of the nuclear shell model in which hopefully the model could explain the spin and parity of the ground state of Mn^{51} and those of the low-lying levels of Cr^{51} .

In the following paragraphs a chronological review is given of the investigations on the decay of Mn^{51} .

Livingood, Fairbrother, and Seaborg (1937) as a result of bombarding chromium oxides with 5.5-MeV deuterons were the first to observe a manganese isotope which emitted positons with a 46 minute half-life. The isotope was positively identified as manganese from chemical analysis, but the assignment of the 46 minute activity to Mn^{51} was not made definite until the following year.

Livingood and Seaborg (1938) pursued the investigation still farther by again bombarding chromium oxides or chrome plated copper targets with a five microampere beam of 5.5-MeV deuterons. Bombardment times were limited to three minutes. The activity of the manganese which was precipitated from the irradiated target by a radiochemical process was followed with a quartz fiber electro-scope. An average half-life of 46 ± 2 minutes from several determinations was reported.

In addition, the range of the positron emitted by the manganese in aluminum was measured to be 0.9 gram/cm² of Al which corresponds to a maximum energy of 2.0 MeV. The gamma-ray present was absorbed to half-value by 5.0 grams/cm² of Pb which is consistent with the 511-keV annihilation radiation expected in positron decay. The presence of the 511-keV gamma-rays strongly supported the idea that the manganese isotope decayed by positron emission rather than electron emission.

The assignment of the 46 minute half-life to Mn⁵¹ was established from the following arguments given by Livingood and Seaborg. The reaction Cr(d, n)Mn could produce the three isotopes Mn⁵¹, Mn⁵³, or Mn⁵⁴ since natural chromium is composed of the Cr⁵⁰, Cr⁵², Cr⁵³, and Cr⁵⁴ isotopes. If Mn⁵⁴ is responsible for the activity, then this same activity should be present following the deuteron bombardment of Fe⁵⁶ through the Fe⁵⁶(d, α)Mn⁵⁴ reaction. However, the latter did not show a 46 minute activity following the bombardment. Furthermore, the bombardment of natural manganese with fast neutrons should produce the activity as a result of the Mn⁵⁵(n, 2n)Mn⁵⁴ reaction, but this too failed to reveal the short-lived activity. The Mn⁵³ isotope can be eliminated on the basis of the decay of Fe⁵³. Radioactive Fe⁵³ decays to Mn⁵³ with a half-life of nine minutes, and ultimately then, the 46 minute activity would appear. However, this has been shown not to occur by

examining the $\text{Cr}^{50}(\alpha, n)\text{Fe}^{53}$ and $\text{Fe}^{54}(n, 2n)\text{Fe}^{53}$ reactions. The possible assignment of the 46 minute activity to Mn^{50} which could be produced by the $\text{Cr}^{50}(d, 2n)\text{Mn}^{50}$ reaction was rejected by studying the excitation function for the proton reactions $\text{Cr}^{50}(p, \gamma)\text{Mn}^{51}$ and $\text{Cr}^{50}(p, n)\text{Mn}^{50}$. The latter of course has a sharp threshold and did not yield the activity of 46 minutes. On the basis of these arguments, Livingood and Seaborg concluded that the 46 minute activity must be assigned to the Mn^{51} isotope.

An additional half-life measurement was performed on Mn^{51} by Miller, Thompson, and Cunningham (1948). They obtained a value of 45 minutes from one bombardment only using a thin window Geiger-Müller counter. No error was listed with their result.

Two years later, Burgus and Kennedy (1950) examined the decay of Mn^{51} which also was produced from the $\text{Cr}^{50}(d, n)$ reaction by bombarding metallic chromium with deuterons. The Mn^{51} was precipitated from the target which had been exposed for 1.5 hours to a beam current of 120 μA . A half-life of 44.3 ± 0.5 minutes resulted from a measurement which extended over eight half-lives using a Geiger counter with a thin mica end-window.

The importance of the investigation of Burgus and Kennedy, however, was not the measurement of the half-life, but was the establishment of the genetic relationship between Mn^{51} and Cr^{51} . Prior to this time it was known that Mn^{51} decayed by the emission

of a beta-ray and it was assumed on the basis of the observed 511-keV radiation that the decay was by positron emission. However, positive identification had not been made. In their experiment Burgus and Kennedy prepared a sample of Mn^{51} which was initially freed of its daughter Cr^{51} and allowed it to decay. Manganese-chromium separations were then made at measured time intervals and the percentage of Cr^{51} activity found in each chromium daughter fraction was compared with the percentage calculated to arise from the decay of a parent with a half-life of Mn^{51} . They found the agreement to be extremely good, and on this basis they concluded that Mn^{51} decayed by positron emission to Cr^{51} with a half-life of 44.3 minutes.

The investigation of the end-point energy of the positron was performed again by Von L. Koester (1954) with a methane flow proportional counter and a set of aluminum absorbers. He obtained an end-point energy of 2.16 ± 0.15 MeV from one measurement along with a half-life value of 45.2 ± 0.4 minutes. The decay was observed over a period of four half-lives to obtain the latter result.

Rudstam (National Research Council, 1955) reported a half-life value of 45.0 ± 0.6 minutes for Mn^{51} from his studies.

Prior to the investigation of Nozawa et al. (1960), the only gamma radiation observed in the decay of Mn^{51} was the annihilation radiation resulting from the positron emission. Examining the decay of Mn^{51} with a NaI scintillation crystal and a multichannel

analyzer, they detected the presence of weak gamma-rays with energies of 740 keV and 1170 keV in addition to the intense annihilation radiation. These weak gamma-rays were identified as belonging to the decay of Mn^{51} since they showed the characteristic half-life of 44 ± 1 minutes. Their relative intensities were estimated by Nozawa et al. as 0.4 ± 0.2 and 0.2 ± 0.1 percent of the positons, respectively. From these, the log ft values for decay to the ground state and the first two excited levels of Cr^{51} were calculated to be 5.2, 7.3, and 6.9, respectively.

The most recent investigation of Mn^{51} was performed by Baskova et al. (1962) with a thin-lens magnetic beta-spectrometer and a gamma-ray scintillation spectrometer. They bombarded chromium enriched targets (87.7 percent Cr^{50}) with deuterons and examined the decay. The Fermi plot of the beta-spectrum in their investigation produced an end-point energy of 2.17 ± 0.05 MeV for the positon decay to the ground state of Cr^{51} in agreement with the result previously given by Koester. In addition, however, a second component with an end-point energy of 600 keV was inferred from the Fermi plot.

The study of the gamma-ray spectrum revealed along with the intense annihilation radiation two weak gamma-rays with energies of 1560 keV and 2030 keV whose intensity decreased with a half-life of 50 ± 10 minutes. The relative intensities of these weak gamma-rays

were calculated to be one percent and one-half percent of the positons, respectively. Baskova et al. concluded that Mn^{51} decays predominantly to the ground state of Cr^{51} by the emission of a positon with an end-point energy of 2.17 MeV and that weak branching occurs to the 1.56-MeV and 2.03-MeV levels of Cr^{51} . They assigned the positon with the 600-keV end-point energy to the 1.56-MeV level and assumed pure electron capture to the 2.03-MeV level. It is interesting to note that in their investigation Baskova et al. make no mention of the weak gamma-rays reported by Nozawa et al.

Figure 1 shows the nuclear levels for Cr^{51} as taken from the Nuclear Data Sheets and the decay scheme for Mn^{51} as inferred from the results previously described. The level structure for Cr^{51} has been determined from several thermal neutron capture studies of Cr^{50} and from (p, n) reaction data on V^{51} . The measured 2.16- and 2.17-MeV end-point energies for the positon transition of Mn^{51} to the ground state of Cr^{51} are low in comparison to the 2.20-MeV value expected from the mass difference of Mn^{51} and Cr^{51} (Howard, 1963). These discrepancies perhaps can be attributed to the uncertainty in the value of the half-life since both of these results depend critically upon the half-life as do the results of any scanning experiment. That is, the experimental data must be corrected to allow for the decay of the isotope. With only two exceptions, it has not been specified in the investigations discussed above whether each

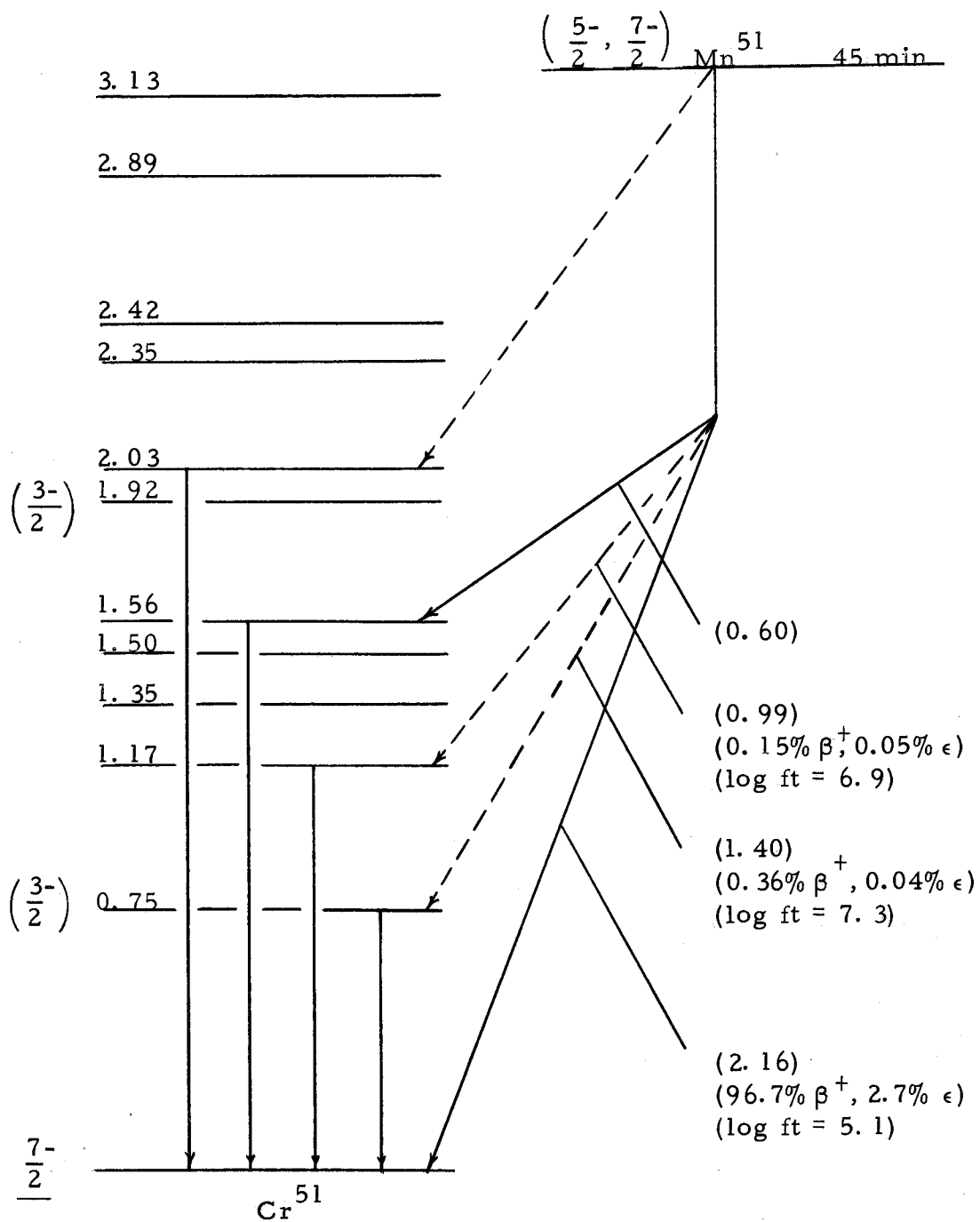


Figure 1. Decay scheme of Mn^{51} and the low-lying levels of Cr^{51} as summarized in the Nuclear Data Sheets.

half-life value is the average of several determinations or the result of a single measurement. Furthermore, no discussion has been given concerning the error listed with each result. Baskova et al. in their beta-analysis did not allow for the energy response of the detector system, an omission of which can lead to an erroneous interpretation of a beta-spectrum. The study to be described utilizes a beta-ray scintillation spectrometer and a multichannel analyzer to measure the end-point energy of the ground state positron transition. This technique eliminates the need for correcting the data for the decay of the isotope. Special consideration also is given to the beta-spectrum to allow for the energy response of the detector system.

The log ft values calculated by Nozawa et al. for transitions to the first two excited levels of Cr^{51} are large in comparison with the value given for the ground state decay, particularly for allowed transitions. These values of course were determined using the estimated relative intensities of the 740-keV and 1170-keV gamma-rays. In the investigation to be described the relative intensities of these weak gamma-rays were experimentally measured and new log ft values were calculated which are consistent with allowed transitions.

Prior to this investigation the spin and parity assignments for the ground state of Mn^{51} and the low-lying levels of Cr^{51} were uncertain. The experimental results of this study together with present theories of nuclear models lead to unambiguous assignments of the spin and parity of these states.

HALF-LIFE MEASUREMENT

Source Production

Sources of Mn^{51} were produced from the $Cr^{50}(d, n)$ reaction by bombarding natural chromium which contains 4.31 percent Cr^{50} with 7-MeV deuterons provided by the Oregon State University cyclotron. Chromium targets 10 mm square by 1 mm thick were exposed for 15 minutes to a 20 μ A beam of deuterons. For the half-life measurement and the gamma-ray analysis the Mn^{51} was not chemically separated from the exposed target since no difference was observed in either the gamma-ray spectrum or the half-life value for separated or non-separated sources. Sources were placed on aluminum holders which have a 1.9 cm aperture and were mounted axially in front of the detector.

Apparatus

Gamma rays were detected by a system consisting of a 7.6 x 7.6 cm NaI(Tl) crystal with an "integral line" mounting on a Dumont-6363 photomultiplier, a Baird Atomic Model 312A Super Stable High-Voltage power supply, a Hamner pre-amplifier and A-8 linear amplifier, and a Technical Measurement Corporation multichannel analyzer operated in the multiscaler mode. The multichannel

analyzer was gated externally by a dwell advance timer in one minute time intervals. A block diagram of the electronics is illustrated by Figure 2. The detector was mounted within a cylindrically shaped Pb-shield, 50 cm inside diameter by 50 cm high with 5 cm wall thickness. A 10 cm Pb-collimator with a 1.5 cm aperture (graded with Cd and Cu) separated the source from the detector. This geometrical arrangement, illustrated by Figure 3, suppressed the room background and optimized the resolution of the detector. The photomultiplier, connected to a voltage divider, was operated at 700 volts positive. The pre-amplifier and the A-8 linear amplifier shaped and amplified the output pulses from the photomultiplier which were then fed to the high-level input of the multichannel analyzer. These pulses were recorded in successive channels in the analyzer in one minute time intervals. Dwell advance gating pulses, separated by one minute time intervals, were supplied by a dwell advance timer, a unit designed and built by the Oregon State Physics Department electronics shop. This timer consists of an electric synchronous motor with a 1 rpm drive connected to a cam which activates a mercury micro-switch once every minute. Closing this switch supplies the dwell advance input of the analyzer with a nine volt positive pulse (from a battery) which advances the analyzer by one channel. Comparison with an electric timer showed the dwell advance unit to have an accuracy of ± 0.1 sec in 72 hours of running time.

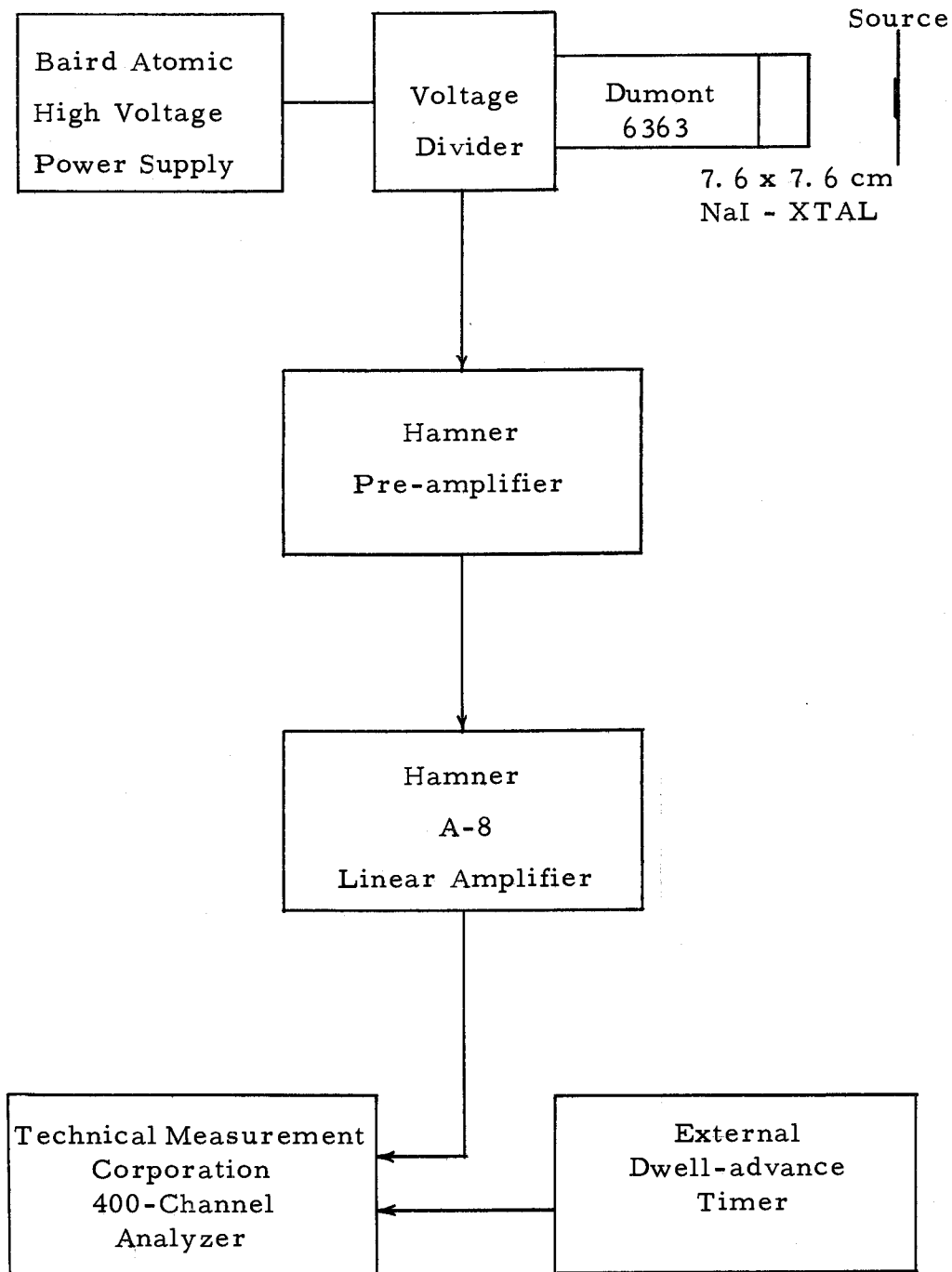


Figure 2. Block diagram of a gamma-ray scintillation spectrometer.

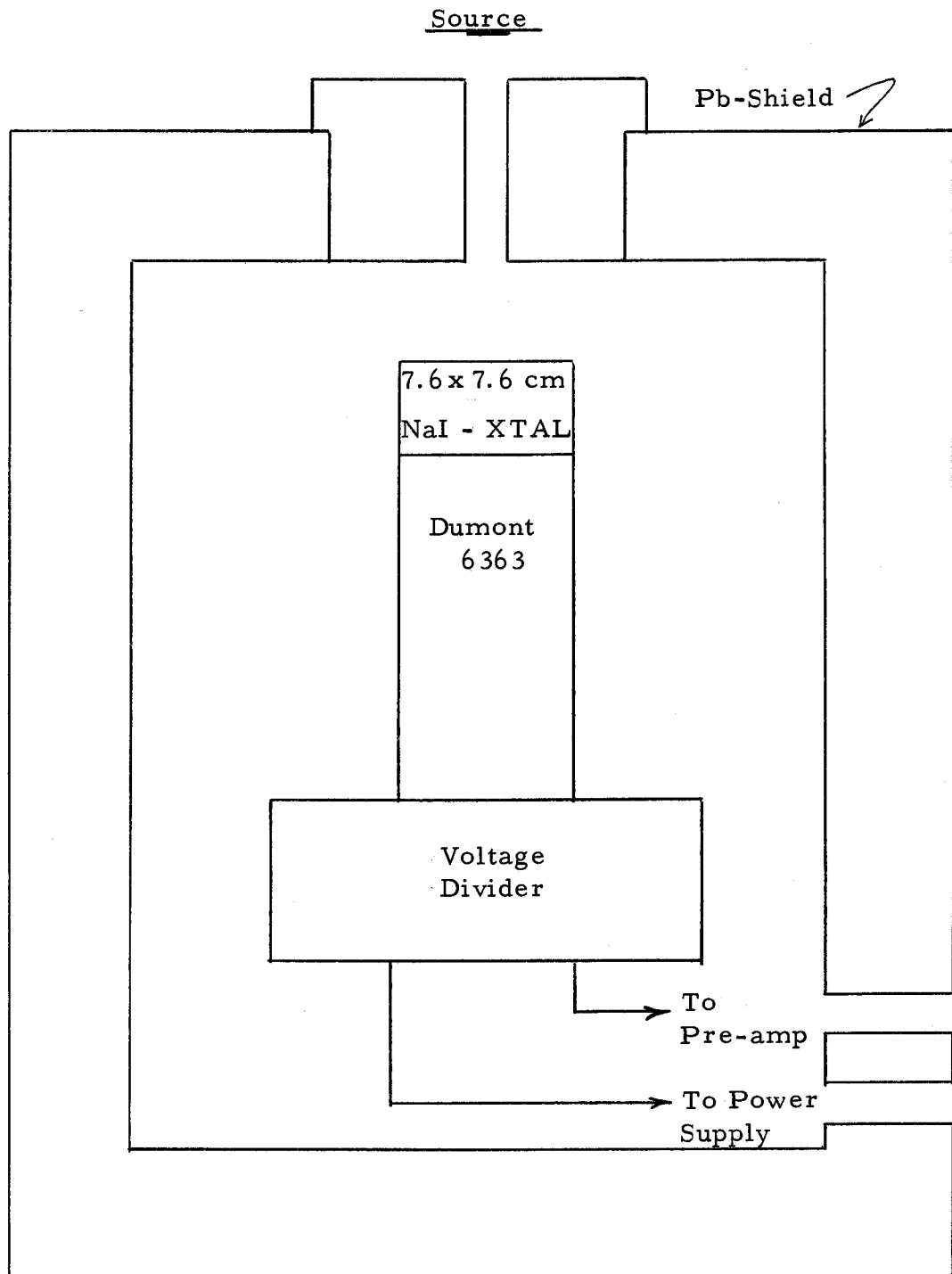


Figure 3. Source-detector geometry for half-life analysis and gamma-ray energy measurement.

Experimental Results

In each half-life measurement the decay of Mn^{51} was followed for 20 half-lives. Figure 4 shows a typical decay curve. After correcting for background and Mn^{54} contamination (identified from the gamma-ray spectrum) the natural logarithms of the counting rates were weighted least squares fitted, as described in Appendix II, to determine the half-life. This calculation was performed on an IBM 1620 computer. The results of 15 measurements are listed in Table 1.

Table 1. Experimentally determined half-life values of Mn^{51} .

Experiment Number	Half-life (minutes)
1	46.15
2	46.74
3	46.68
4	46.57
5	46.53
6	46.63
7	46.71
8	46.59
9	46.28
10	46.50
11	46.50
12	46.39
13	46.54
14	46.40
15	46.55

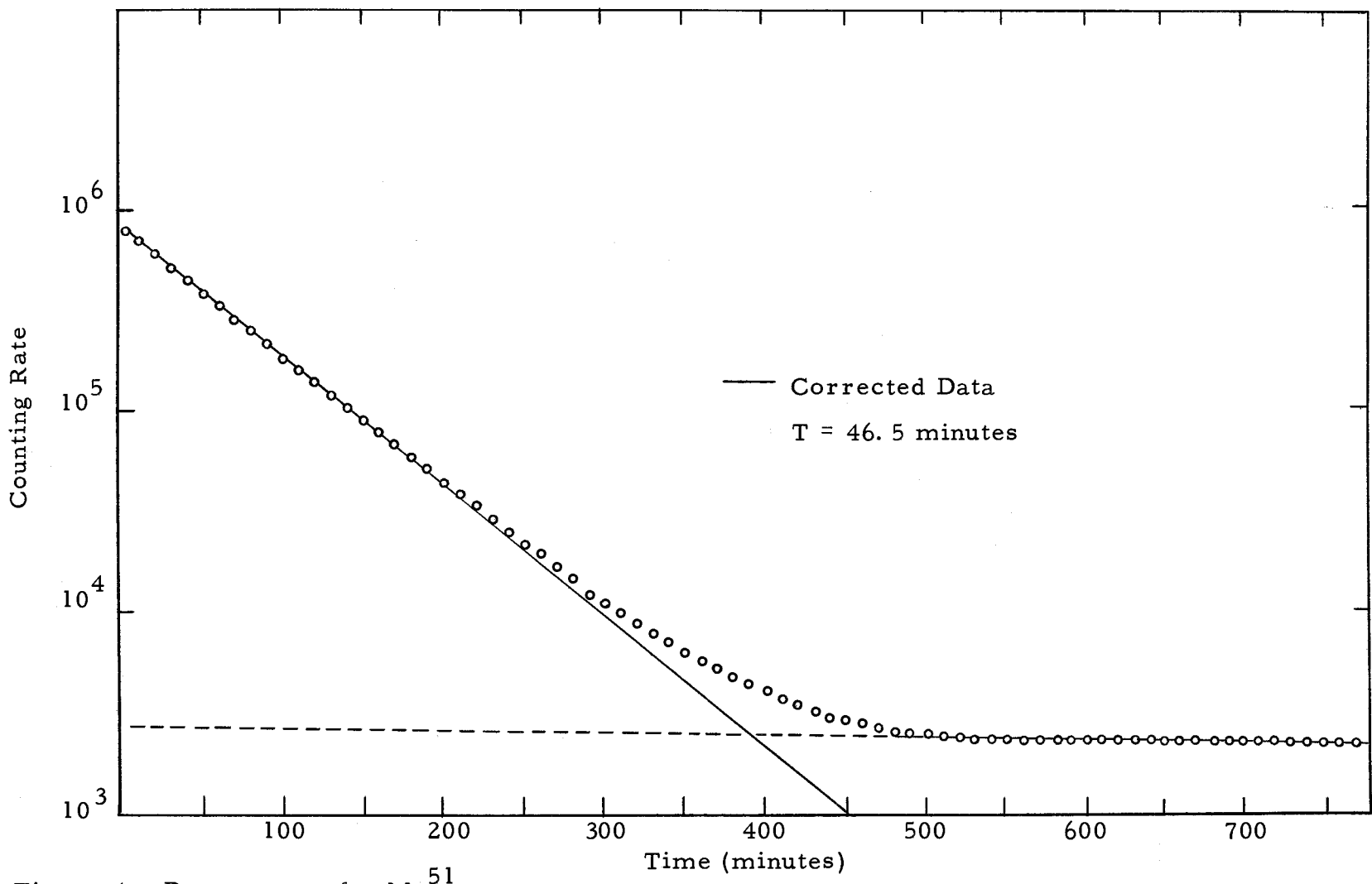


Figure 4. Decay curve for Mn^{51} .

An average half-life value, \bar{T} , and standard deviation, σ , can be determined from the following two equations,

$$\bar{T} = \frac{\sum_{i=1}^N T_i}{N}, \quad (1)$$

$$\sigma^2 = \frac{\sum_{i=1}^N (\bar{T} - T_i)^2}{N}, \quad (2)$$

where N is the number of observations. The result is $\bar{T} = 46.5 \pm 0.2$ minutes.

GAMMA-RAY ENERGY MEASUREMENT

Apparatus

Gamma-ray pulse-height spectra were recorded with the same gamma-ray scintillation spectrometer and source-detector geometry as described in the previous section and illustrated by Figures 2 and 3. However, the analyzer was operated in the PHA mode (pulse-height-analyze mode) rather than the multiscaler mode, and therefore, the dwell advance timer was not required.

Experiment and Results

Energy calibration of the detector system was performed before and after the recording of each Mn^{51} spectrum with sources of Co^{60} , Cs^{137} , Na^{22} , Mn^{54} , and Bi^{207} . In order to account for any drift in the electronics during the recording of the Mn^{51} spectra, the two pulse-height spectra obtained in this procedure for each calibration source were combined channel by channel before plotting. Figure 5 shows the result of one such energy calibration along with the technique used to determine the channel number corresponding to the centroid of the photopeak for each calibration gamma-ray. Plotting these channel numbers (or centroids) vs. the corresponding gamma-ray energies provides the desired energy calibration. In this experiment, however, rather than drawing a line through the calibration

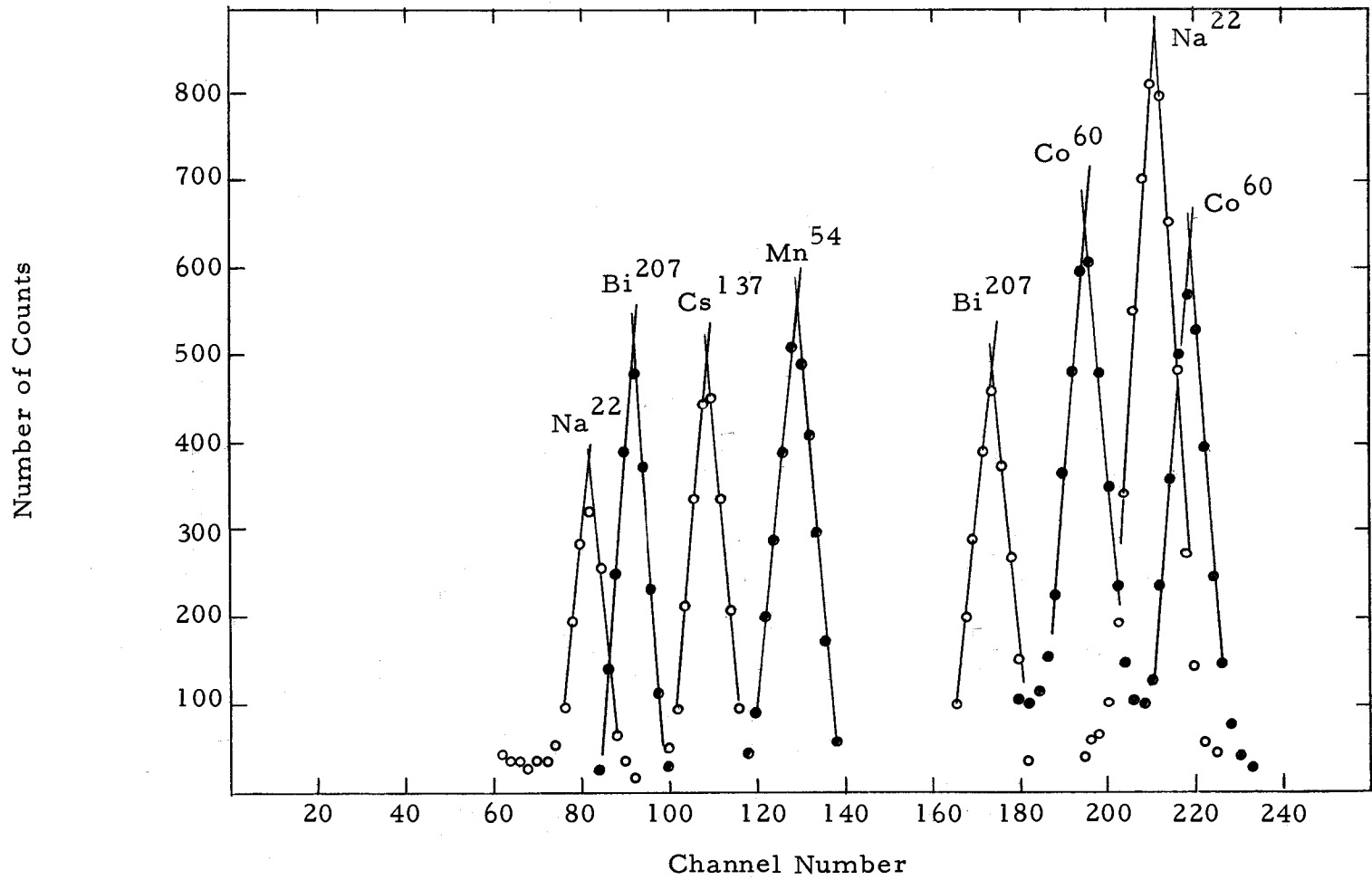


Figure 5. Gamma-ray pulse-height spectra for energy calibration sources.

points, the equation

$$E = aC + b. \quad (3)$$

was fitted to the eight points by the method of least squares (Beers, 1957) to obtain the best fit. Here, E represents the energy of the gamma-ray and C the corresponding channel number while a and b are constants determined in the least squares fit. Figure 6 illustrates graphically the eight calibration points and the resulting fit of equation (3). The gamma-ray energies associated with the decay of Mn^{51} were determined by finding the centroid in terms of a channel number, C , of each photopeak observed in the spectrum and then substituting the result into equation (3). The results of the investigation of the Mn^{51} gamma-ray spectrum are given below.

Figure 7 shows a Mn^{51} gamma-ray spectrum obtained during a 100 minute live-time analysis; room background has been subtracted. The intense gamma-ray has been identified as the 511-keV annihilation radiation which arises from the predominant positron decay of Mn^{51} to the ground state of Cr^{51} . In addition, however, two weak gamma-rays also appear in the spectrum and have measured energies of 761 ± 11 keV and 1170 ± 15 keV. Since these gamma-rays in addition to the annihilation radiation decayed with a half-life characteristic of Mn^{51} , it was inferred that the first two excited levels of Cr^{51} are populated by positron emission and electron capture

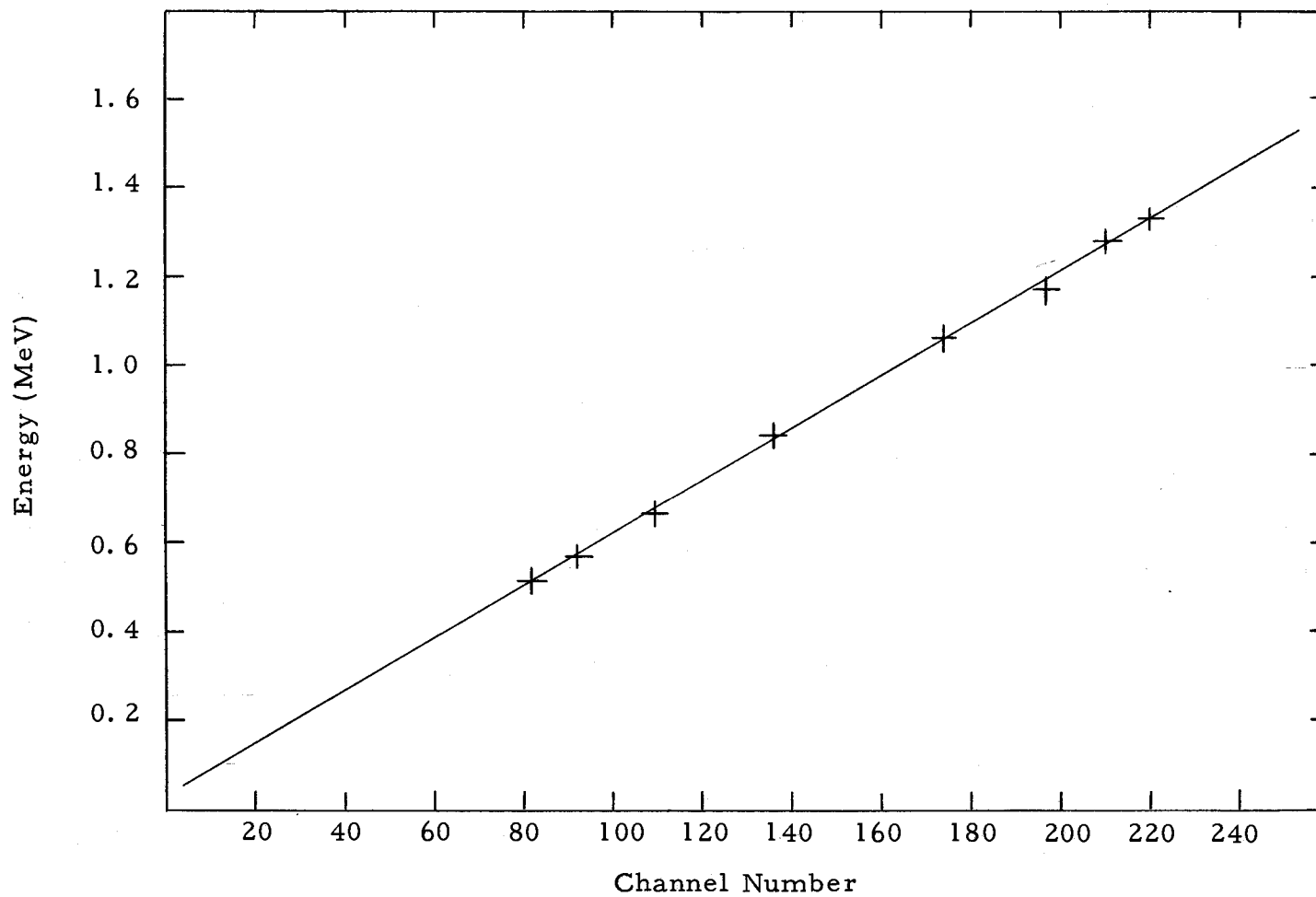


Figure 6. Energy calibration for gamma-ray pulse-height spectra.

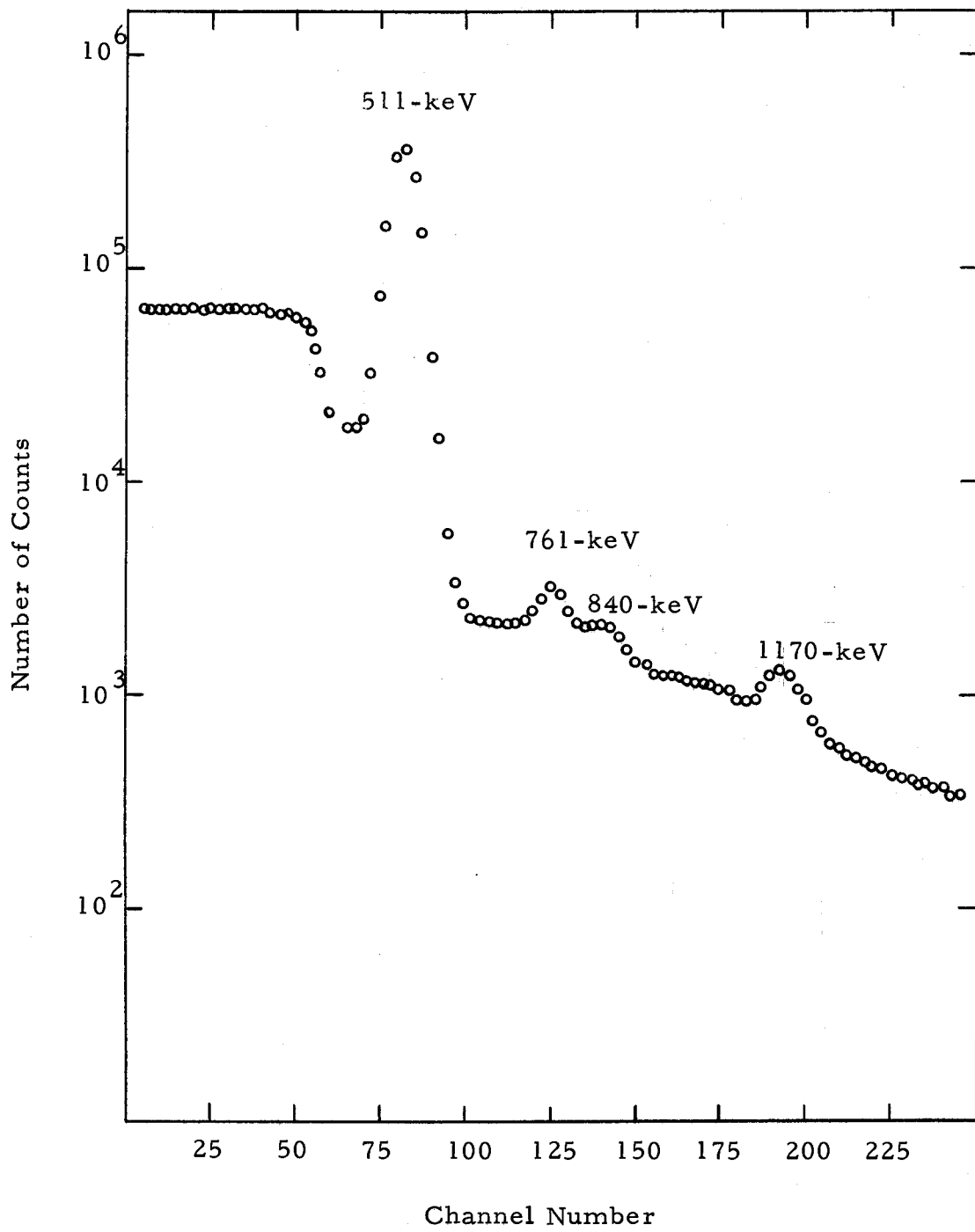


Figure 7. Gamma-ray pulse-height spectrum for Mn^{51} .

from the decay of Mn^{51} . As yet, however, direct observation of the positron-decay to these levels has not been observed. The 840-keV gamma-ray also present in the gamma-ray spectrum is due to Mn^{54} contamination.

Twenty-two sources (obtained in optimizing the time and energy of the bombardments) were analyzed in the energy measurement of these weak gamma-rays. Table 2 lists the experimental results.

Table 2. Experimental results of gamma-ray energy measurements of Mn^{51} .

Experiment Number	Gamma-ray 1 (keV)	Gamma-ray 2 (keV)
1	773 ± 10	1177 ± 12
2	755 ± 10	1161 ± 13
3	752 ± 9	1158 ± 15
4	766 ± 10	1188 ± 13
5	768 ± 13	1183 ± 20
6	752 ± 11	1156 ± 17
7	769 ± 12	1183 ± 18
8	763 ± 14	1171 ± 21
9	766 ± 12	1180 ± 16
10	761 ± 14	1170 ± 21
11	767 ± 11	1181 ± 18
12	771 ± 11	1178 ± 18
13	766 ± 16	1176 ± 18
14	764 ± 13	1170 ± 20
15	769 ± 15	1181 ± 16
16	752 ± 15	1163 ± 17
17	756 ± 14	1165 ± 15
18	757 ± 7	1170 ± 13
19	761 ± 8	1166 ± 14
20	760 ± 9	1161 ± 16
21	758 ± 14	1162 ± 15
22	756 ± 9	1162 ± 10

Associated with each energy measurement listed in Table 2 is an error, S_e , which is obtained as follows: The coefficients a and b appearing in equation (3) have errors S_a and S_b , respectively, resulting from the least squares fit. Furthermore, since the gamma-rays were so weak, some difficulty arose in determining the centroid of the photopeaks, and therefore, an error in the establishment of C , denoted by S_c , was estimated. Including these errors, equation (3) becomes,

$$E \pm S_e = (a \pm S_a)(C \pm S_c) + (b \pm S_b) \quad , \quad (4)$$

from which S_e evolves as,

$$S_e = \left[(CS_a)^2 + (aS_c)^2 + S_b^2 \right]^{\frac{1}{2}} \quad . \quad (5)$$

Using the squared inverse of each of these errors, S_e , as weighting factors, an average energy value, \bar{E} , and standard deviation, σ , can be determined from the following two equations for each of the two weak gamma-rays,

$$\bar{E} = \frac{\sum_i E_i W_i}{\sum_i W_i} \quad , \quad (6)$$

$$\sigma^2 = \frac{\sum_i S_e^2 W_i}{\sum_i W_i} \quad , \quad (7)$$

where W_i is the weighting factor defined previously.

The resulting values are 761 ± 11 keV and 1170 ± 15 keV.

GAMMA-RAY RELATIVE INTENSITY MEASUREMENT

Apparatus

Intensity measurements of the 761-keV and 1170-keV gamma-rays relative to the positron emission were performed with the same pulse-height gamma-ray scintillation spectrometer as described in the previous section. However, in order to utilize the calculated detector efficiencies given by Heath (1964) for a 7.6 x 7.6 cm NaI(Tl) crystal, a different source-detector geometry was required which did not use the Pb-shield nor the collimation system previously described. The detector was operated in a vertical position and surrounded only by a framework to support the sources which were mounted axially in front of the detector at a distance of 10 cm from the face of the crystal. This particular geometry was chosen because it reproduced the system used by Heath in his gamma-ray studies and calculation of detector efficiencies.

Experiment and Results

The relative intensity of two gamma-rays is defined simply as the ratio of the absolute emission rate for each gamma-ray. Absolute emission rates can be determined experimentally from a gamma-ray pulse-height spectrum by using the following expression given by

Heath:

$$N_o = \frac{N_p}{T(E)PA} \quad (8)$$

where N_o is the emission rate, N_p is the area under the photopeak, P is the peak-to-total ratio, $T(E)$ is the total absolute detector efficiency, and A is a correction factor which allows for gamma-ray absorption in a beta-absorber. Figure 8 which shows a Cs^{137} gamma-ray spectrum illustrates by the shaded portion what is meant by the area under the photopeak. Peak-to-total ratios, P , are defined as the ratio of N_p to the total area contained in the gamma-ray spectrum. Total absolute detector efficiencies, $T(E)$, functions of the gamma-ray energy and the source-detector geometry, have been calculated and tabulated for various size NaI(Tl) crystals by Heath (1964).

Initially, peak-to-total ratios were measured for Cs^{137} , Cr^{51} , Mn^{54} , and Zn^{65} sources and compared with those reported by Heath for a 7.6 x 7.6 cm NaI(Tl) crystal. Figure 9 shows the excellent agreement obtained between the values determined in this experiment and those given by Heath. Relative intensity measurements for the 1170-keV and 1330-keV gamma-rays of Co^{60} and the 1280-keV and 511-keV gamma-rays of Na^{22} also were measured. These measurements too were in agreement with the accepted values which gave a measure of the reliability of the experimental system and

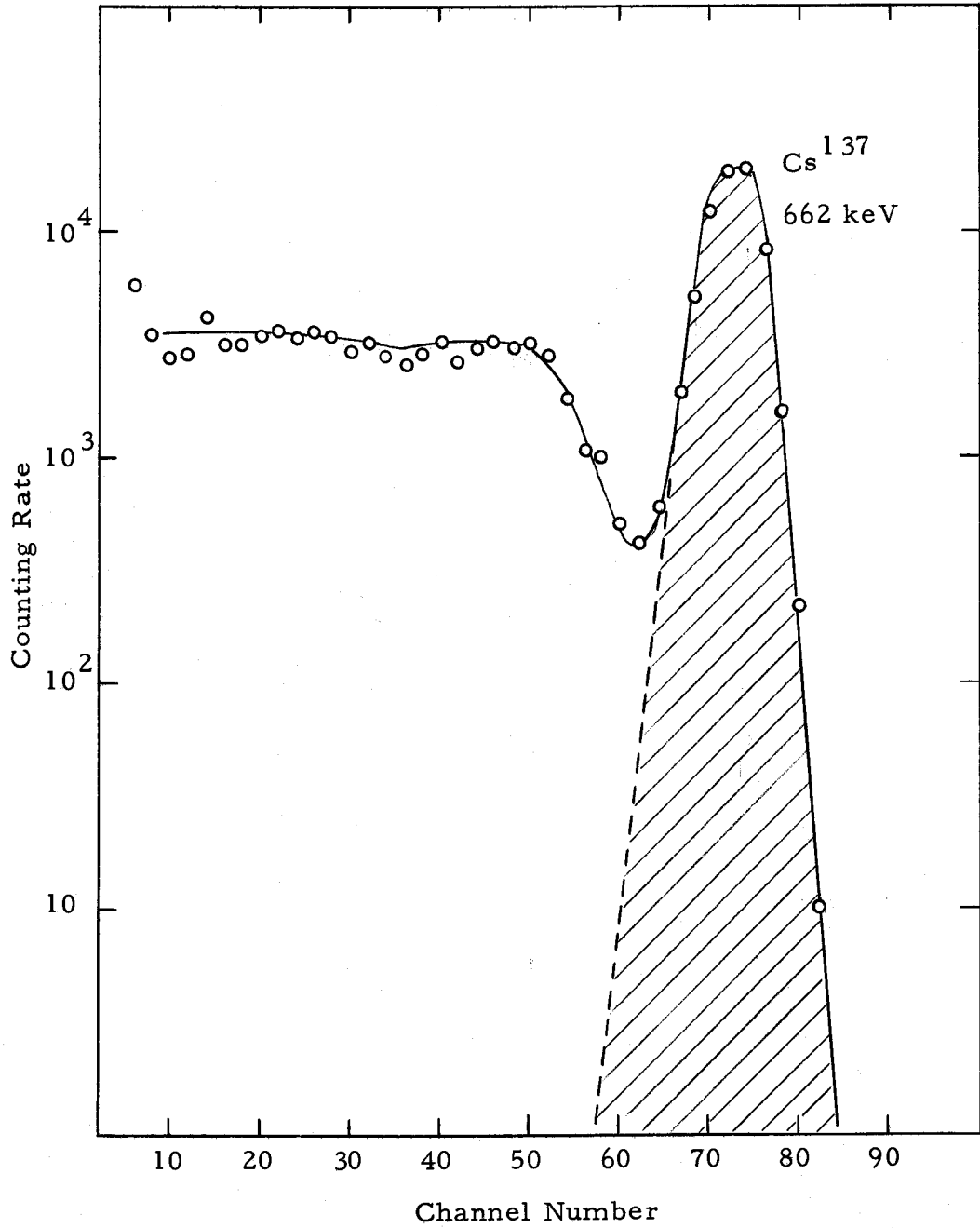


Figure 8. Gamma-ray spectrum for Cs¹³⁷.

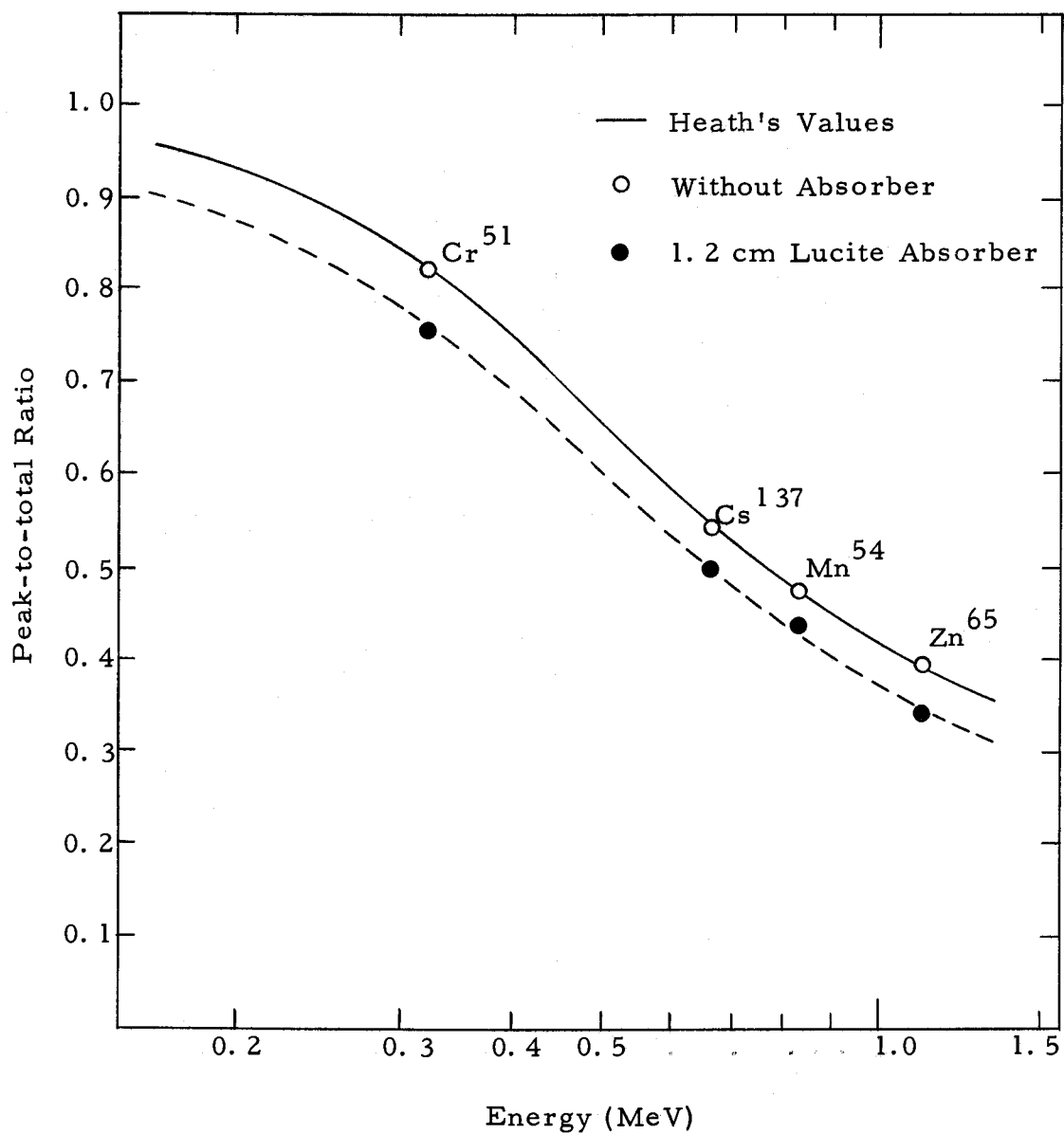


Figure 9. Peak-to-total ratios for a 7.6 x 7.6 cm NaI(Tl) crystal with a 10 cm source-to-detector distance.

the techniques used in this experiment.

For the intensity measurement of the 761-keV and 1170-keV gamma-rays relative to the 511-keV gamma-ray of Mn^{51} , the source was placed between two Lucite absorbers with a 1.2 cm thickness. This arrangement was designed to stop the 2.2 MeV positons which produced the annihilation radiation at a source-to-detector distance of 10 cm. Since Lucite absorbers were used here, peak-to-total ratio measurements which were described above were again made for Cs^{137} , Cr^{51} , Mn^{54} , and Zn^{65} sources using a 1.2 cm thick Lucite absorber. Figure 9 shows the results which are slightly less than the peak-to-total ratios obtained without the absorber. Comparing the peak-to-total ratios obtained with and without the absorber provides a means for determining the correction factor A listed in equation (8).

Figure 10 illustrates a Mn^{51} gamma-ray spectrum obtained with a geometry and source configuration described above during a 100 minute live-time analysis; room background has been subtracted. Shown in this figure too are the components which contribute to the composite Mn^{51} spectrum. Among these components are the 511-keV annihilation radiation, the 761-keV and 1170-keV gamma-rays of Mn^{51} , an 840-keV gamma-ray from Mn^{54} , a bremsstrahlung distribution produced by the energetic positon while passing through the Lucite absorber, and a 1.02-MeV coincidence sum-spectrum due to

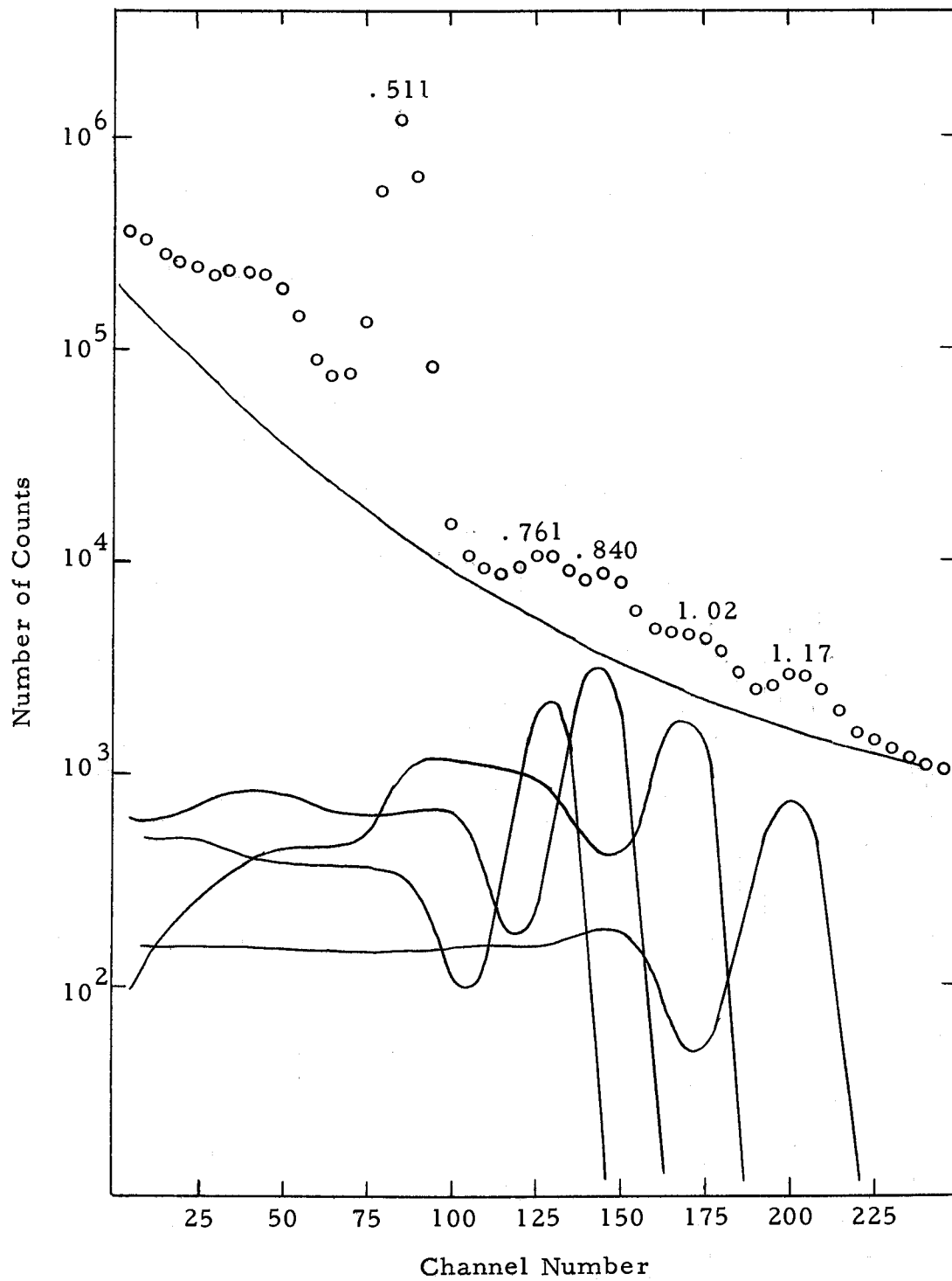


Figure 10. Mn^{51} gamma-ray spectrum.

the intense annihilation radiation. The bremsstrahlung distribution was determined experimentally with an Y^{90} source which emits a beta-ray with an end-point energy of 2.26 MeV, roughly the same as that emitted by Mn^{51} . Figure 11 shows the experimentally determined bremsstrahlung distribution. Gamma-ray spectra obtained in the peak-to-total ratio measurements using a Lucite absorber are shown in Figure 12 for Cs^{137} , Cr^{51} , Mn^{54} , and Zn^{65} sources. The 1170-keV component of Mn^{51} was approximated by the 1.114-MeV spectrum of Zn^{65} while the 761-keV line of Mn^{51} was constructed from the 662-keV line of Cs^{137} and the 840-keV line from Mn^{54} . Using a Na^{22} gamma-ray spectrum which exhibits a 511-keV and a 1280-keV gamma-ray, the 511-keV component was obtained by extending the Compton distribution of the 1280-keV gamma-ray back to zero energy and then subtracting from the composite distribution of Na^{22} . This procedure is illustrated in Figure 13 which shows a Na^{22} spectrum and the resulting single 511 keV component. The coincidence sum-spectrum, sometimes called pile-up, is produced by two gamma-rays interacting with a crystal in a time interval which is short compared with the resolving time of the detector. Consequently, the detector cannot distinguish between the two gamma-rays and the pulse-height produced is simply proportional to the sum of the energy lost in the crystal by the two gamma-rays. In the resulting spectrum one finds pulses of all sizes from the minimum

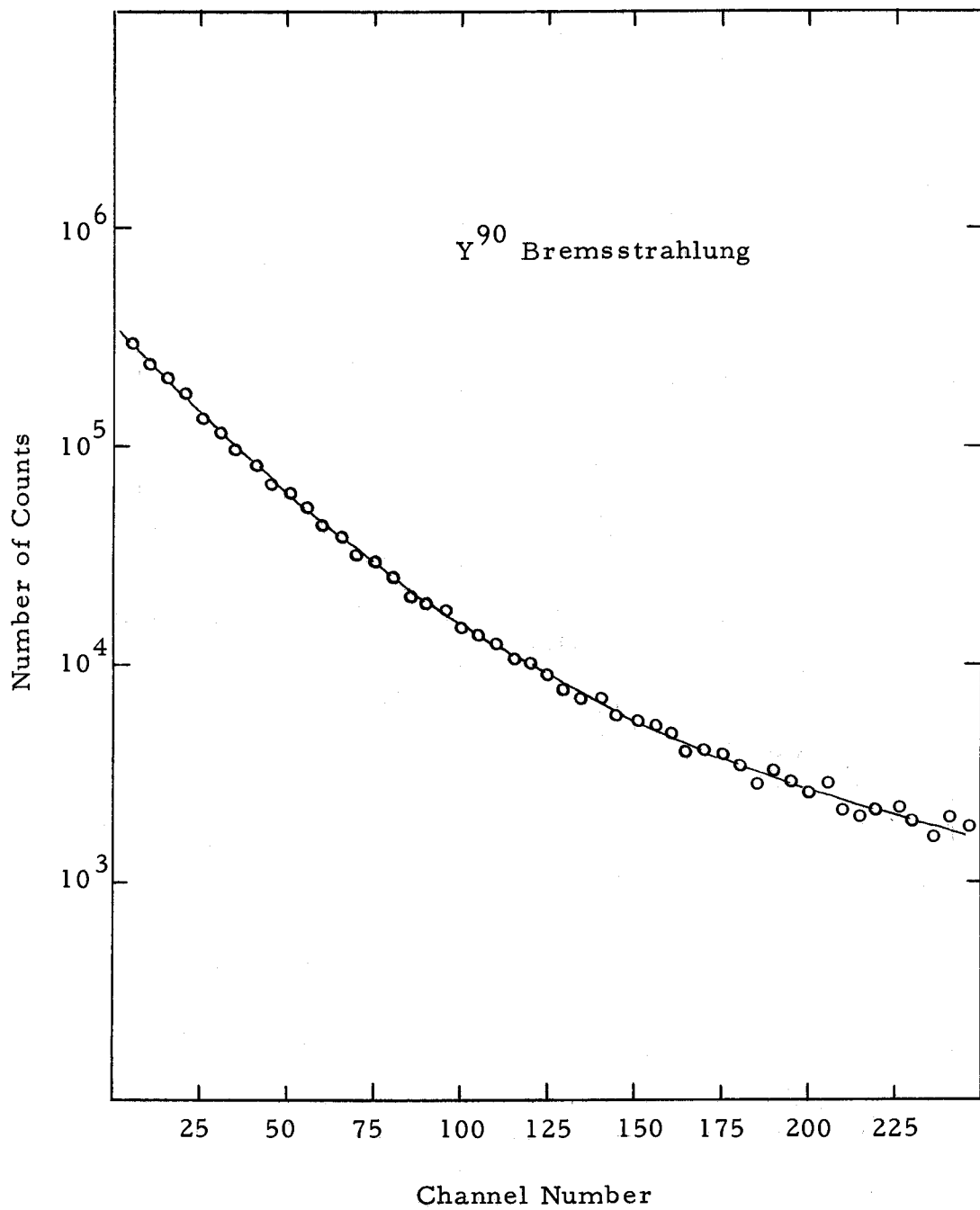


Figure 11. Y^{90} Bremsstrahlung distribution.

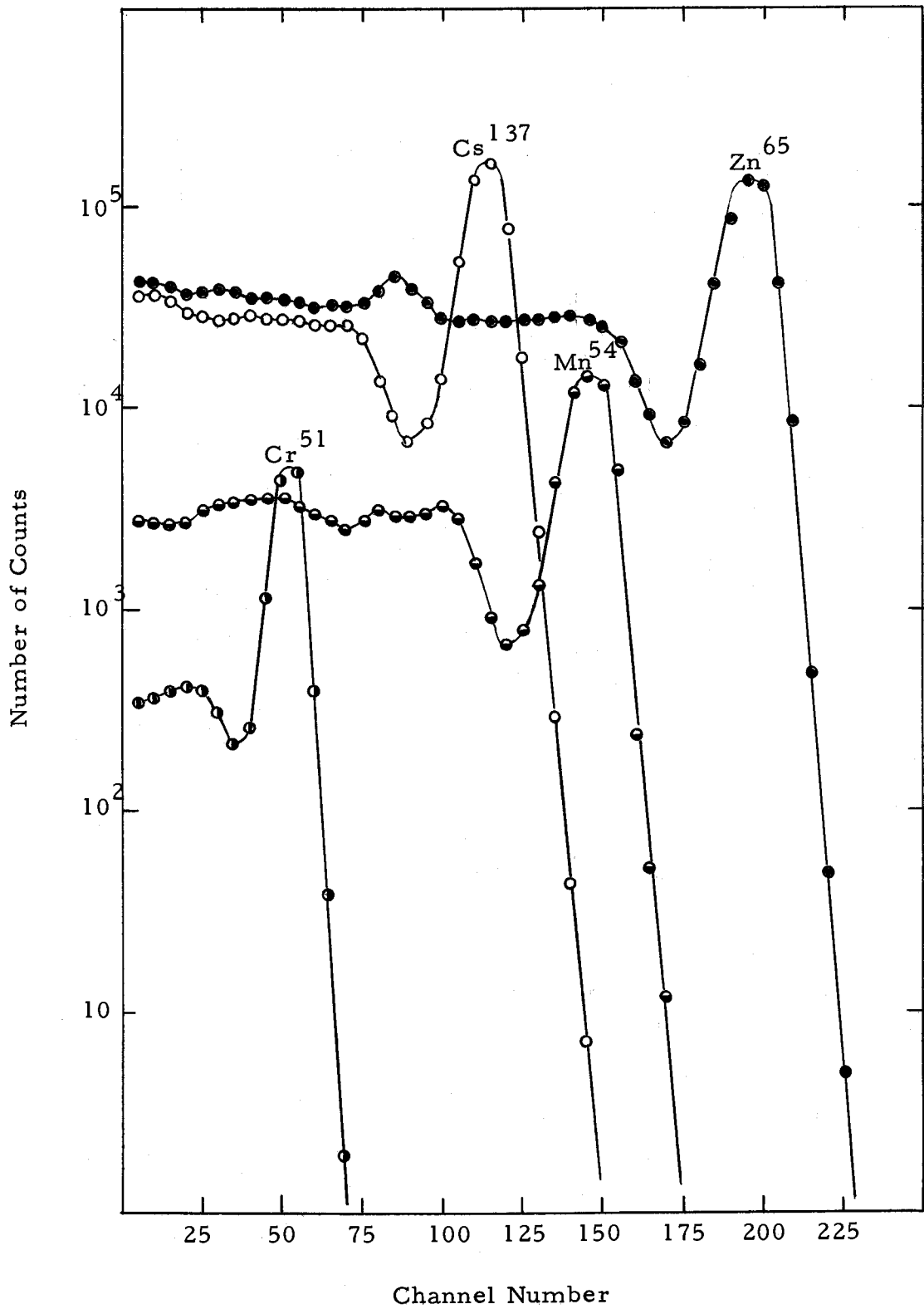


Figure 12. Gamma-ray spectra for Cs¹³⁷, Cr⁵¹, Mn⁵⁴, and Zn⁶⁵ sources.

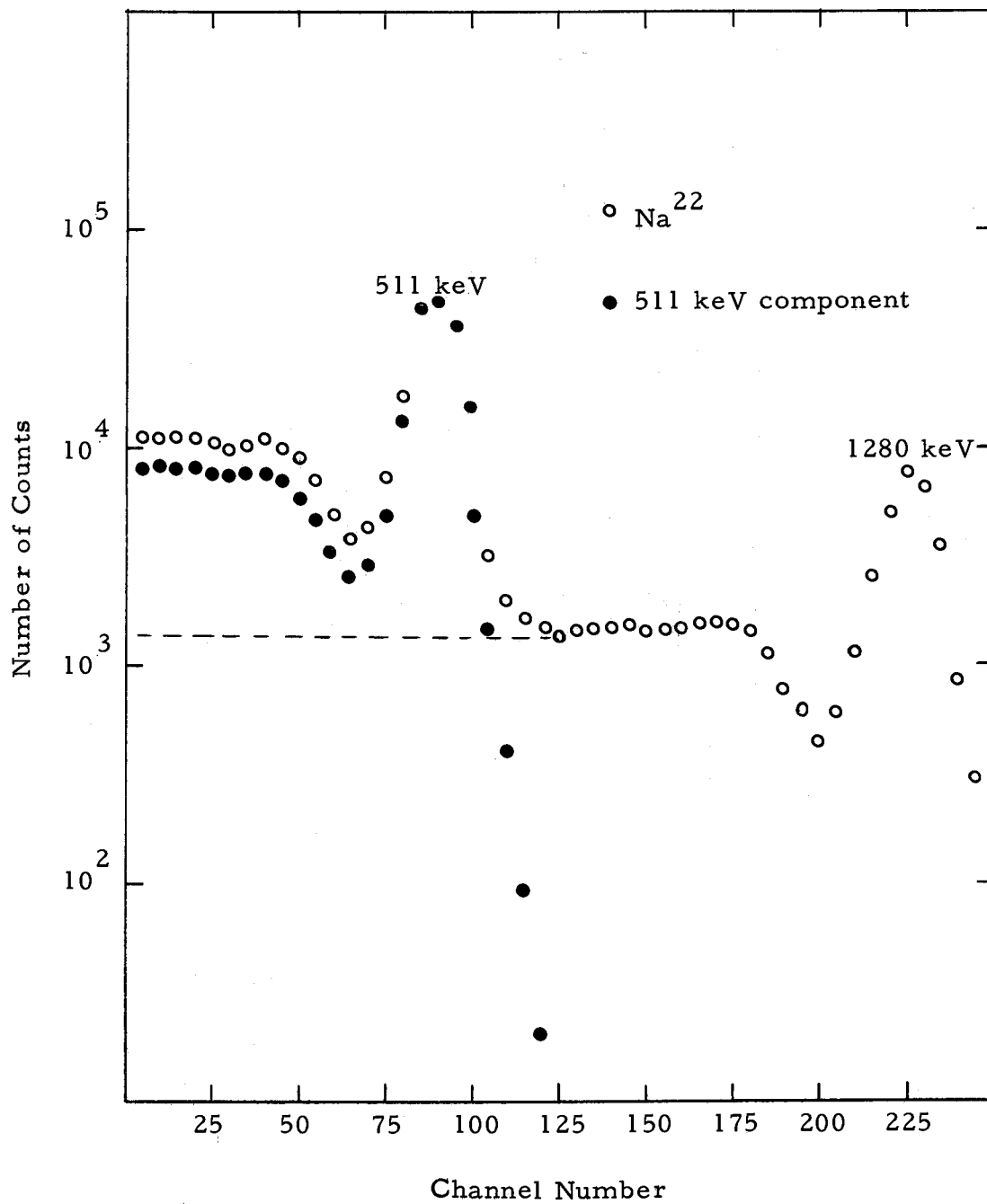


Figure 13. Na^{22} gamma-ray spectrum.

detectable height to the sum of the maximum pulse-heights obtainable from the individual gamma-rays. In the case of Mn^{51} , the intense 511-keV annihilation radiation produced the coincidence sum-spectrum. Using the 511-keV gamma-ray spectrum shown in Figure 13 and the techniques given by Heath (1964) the shape of the sum-spectrum can be calculated. Let $G_1(a)$ denote the probability of detecting a gamma-ray in channel a and $G_2(b)$ the probability of detecting a second gamma-ray in channel b . The probabilities used here are simply the counting rates in a particular channel number for the given 511-keV gamma-ray spectrum. Forming the product $G_1(a)G_2(b)$ gives the probability of detecting the sum of these two gamma-rays in channel c for which $a + b = c$. The total contribution to a particular channel c is determined by summing the product $G_1(a)G_2(b)$ over all possible pairs of a and b for which $a + b = c$, that is,

$$S(c) = \sum_{n=1}^c G_1(n)G_2(c-n) . \quad (9)$$

The resulting coincidence sum-spectrum obtained in this way for the 511-keV annihilation radiation is given in Figure 14.

To determine the intensity of the 761-keV and 1170-keV gamma-rays of Mn^{51} relative to the annihilation radiation, one must unfold the composite Mn^{51} spectrum, that is, determine the contribution of

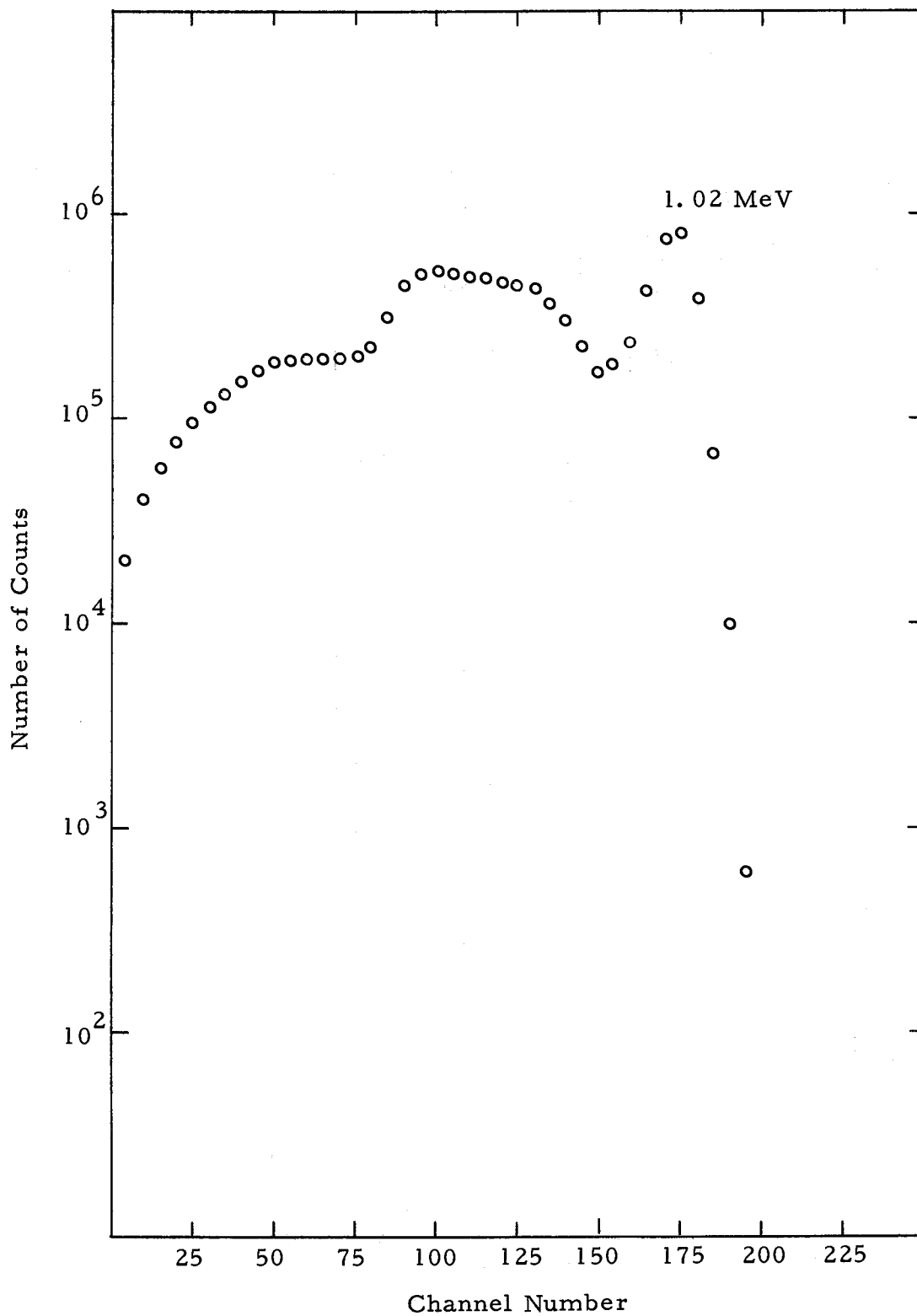


Figure 14. Coincidence sum-spectrum for 511-keV annihilation radiation.

each gamma-ray to the total spectrum. From the total spectrum the bremsstrahlung distribution was subtracted after matching this distribution with the high energy portion of the Mn^{51} spectrum. Next, the 1170-keV spectrum was subtracted after matching the photopeak of the 1114-keV gamma-ray of Zn^{65} with the 1170-keV photopeak appearing in the Mn^{51} gamma-ray spectrum minus the bremsstrahlung distribution. In successive order, the contribution of the coincidence sum-spectrum, the 840-keV line, the 761-keV line, and the 511-keV gamma-ray were subtracted. Figure 10 shows the result of the unfolding process. For each of the 511-keV, 761-keV, and 1170-keV gamma-rays shown in Figure 10, the area under the photopeak, N_p , was calculated. Using these values of N_p , the peak-to-total ratios from Figure 9 for gamma-ray energies of 511 keV, 761 keV, and 1170 keV, and the tabulated values of the absolute detector efficiencies, $T(E)$, given by Heath (1964), the absolute emission rate N_o for each of the gamma-rays listed above was determined from equation (8). Once these values N_o were calculated, the relative intensities of the 761-keV and 1170-keV gamma-rays to the 511-keV annihilation radiation were computed by taking the ratios of N_o . Table 3 lists the experimental results of six measurements. From these measurements an average value and error for the intensity of the 1170-keV gamma-ray relative to the 511-keV annihilation radiation of 0.24 ± 0.06 percent was determined while the value

for the 761-keV gamma-ray to the annihilation radiation of 0.35 ± 0.05 percent was obtained. To calculate the intensity of the 761-keV and 1170-keV gamma-rays relative to the positron emission, one doubles the values given below.

Table 3. Relative intensities of the 761-keV and 1170-keV gamma-rays to the 511-keV annihilation radiation for Mn^{51} .

Experiment Number	761 keV Relative Intensity %	1170 keV Relative Intensity %
1	0.29	0.14
2	0.34	0.27
3	0.36	0.24
4	0.41	0.30
5	0.40	0.30
6	0.28	0.20

END-POINT ENERGY MEASUREMENT

Apparatus

The investigation of the end-point energy of the positron which decays to the ground state of Cr^{51} was performed with a beta-ray scintillation spectrometer and a beta-gamma coincidence scintillation spectrometer. Figure 15 gives a block diagram of the electronics for the beta-gamma coincidence spectrometer which is easily converted to a beta-ray spectrometer by removing the gating signal supplied to the multichannel analyzer and the coincidence requirement on the analyzer. Beta-rays were detected with a 3.8 x 2.5 cm Pilot-B plastic scintillator optically coupled to an RCA 6655A photomultiplier while gamma-rays were detected with a 3.8 x 2.5 cm NaI(Tl) crystal optically coupled to an RCA 6655A photomultiplier. In order to avoid absorption in a crystal covering these detectors which had an angular separation of 90° were mounted inside a light-tight enclosure. Sources were prepared as described in Appendix I and mounted 2 cm from the Pilot-B detector and 10 cm from the NaI(Tl) detector. The coincidence spectrometer was used only in the study of line shapes for monoenergetic electrons supplied by conversion electrons from sources of Cs^{137} and Bi^{207} and operated in the following manner: Voltage pulses from the photomultipliers, resulting from the interaction of beta-rays and gamma-rays with the

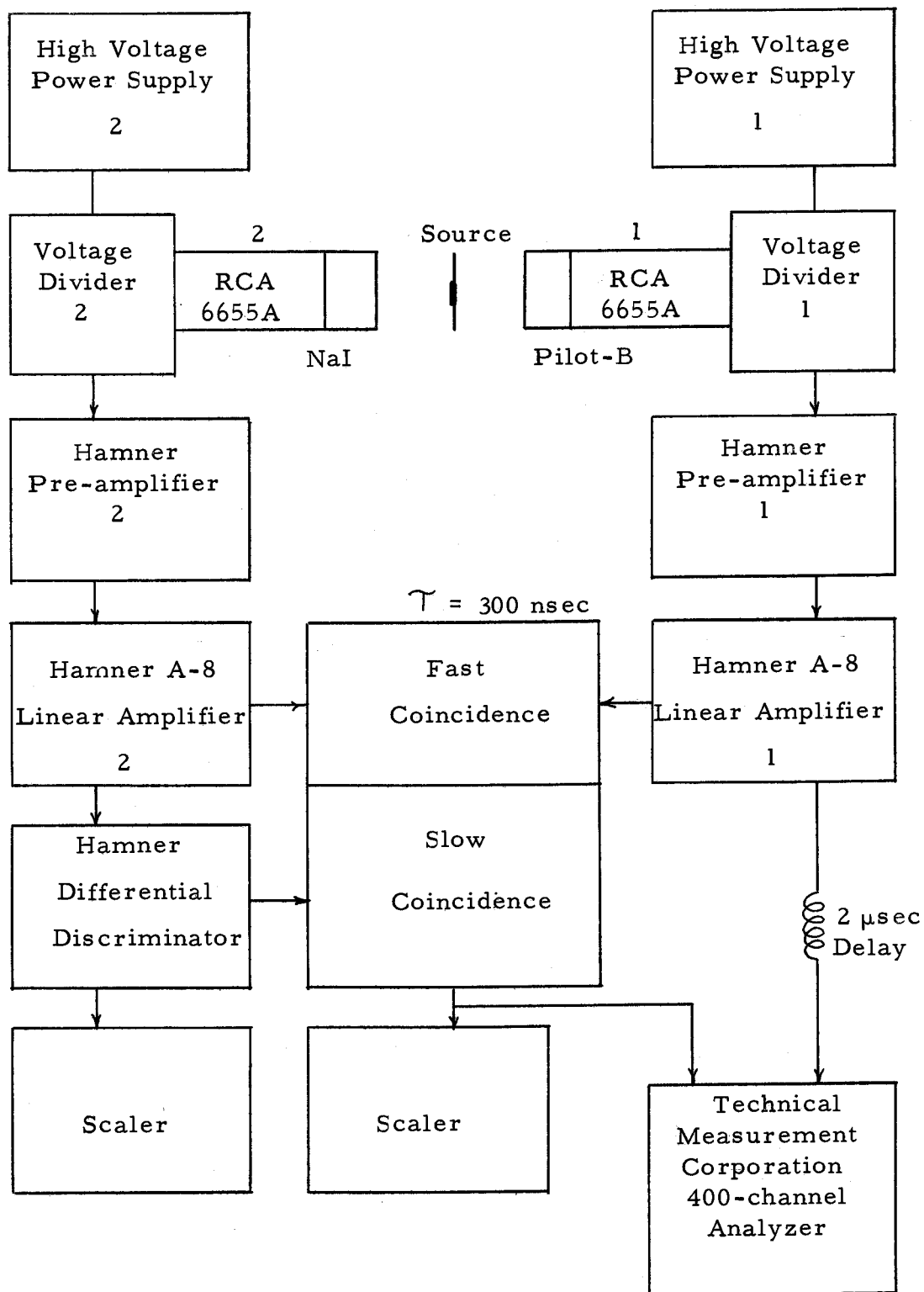


Figure 15. Block diagram of a beta-gamma coincidence spectrometer.

Pilot-B and NaI(Tl) scintillators, respectively, were amplified by two Hamner pre-amplifiers and A-8 linear amplifiers. From these signals, gating pulses were formed in each of the linear amplifiers and fed into the fast coincidence unit where an output pulse resulted if the two gating signals, one from each amplifier, arrived at the fast coincidence unit within a resolving time of 300 nsec. In addition to demanding fast coincidence, the system also required the pulses from detector 2 to satisfy a certain energy requirement which was provided by a differential energy discriminator whose baseline and window width were adjusted to bracket just the photopeak of the gamma-ray for which the beta-rays are in coincidence. The output of the differential discriminator was split to feed the slow coincidence circuit. Because the signal was divided in this manner, every signal from the differential discriminator provided the coincidence requirements necessary to trigger the slow coincidence unit. If the coincidence requirements were satisfied in both the fast and slow units by the occurrence of two events, one in detector 1 and the other in detector 2, then a gating pulse was supplied to the multichannel analyzer which turned the analyzer on for a duration of 4 μ sec, a period during which a pulse coming from linear amplifier 1 could be recorded. As shown in Figure 15, the pulses coming from amplifier 1 were delayed by 2 μ sec to allow for the inherent time required to generate the gating pulse for the multichannel analyzer.

Experiment and Results

The beta-ray scintillation spectrometer was energy calibrated with conversion electrons from sources of Cs^{137} and Bi^{207} ; the Pilot-B scintillator had an energy resolution of 15 percent for the 624-keV K-conversion line from Cs^{137} . Figure 16 shows typical beta-ray spectra used for energy calibration. In addition to Cs^{137} and Bi^{207} , calibration was also provided by sources of Y^{90} and P^{32} with end-point energies of 2.26 MeV and 1.704 MeV, respectively.

In the measurement of end-point energies of beta-rays and positons a difficulty arises which cannot be neglected; the recorded energy spectrum is not the true spectrum emitted by the source. This difference is illustrated most easily by Figure 17 which shows the energy response of a Pilot-B scintillator to a source of monoenergetic electrons from Cs^{137} . Centered around the energy 624 keV, the energy of the conversion electrons, is the normal statistical broadening which is approximately gaussian in shape (Palmer and Laslett, 1951). Along with this factor, however, is a low intensity backscatter contribution extending to zero energy caused by the electrons losing only part of their energy in the detector, the remainder being scattered out. Because of this energy response, a continuous beta-spectrum recorded in an experiment will exhibit a greater number of counts in the low energy part of the spectrum than

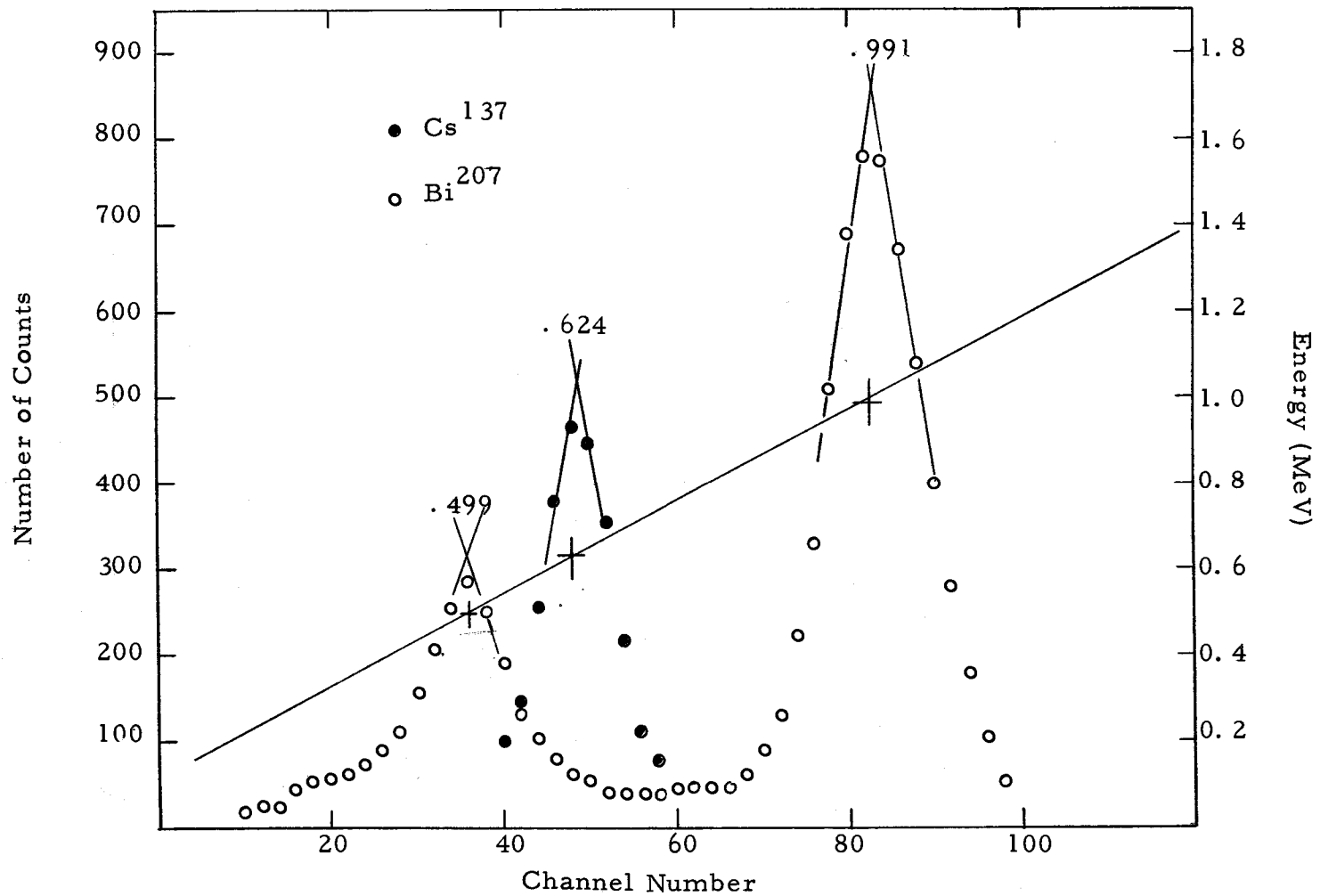


Figure 16. Beta-ray spectra for Cs^{137} and Bi^{207} and energy calibration.

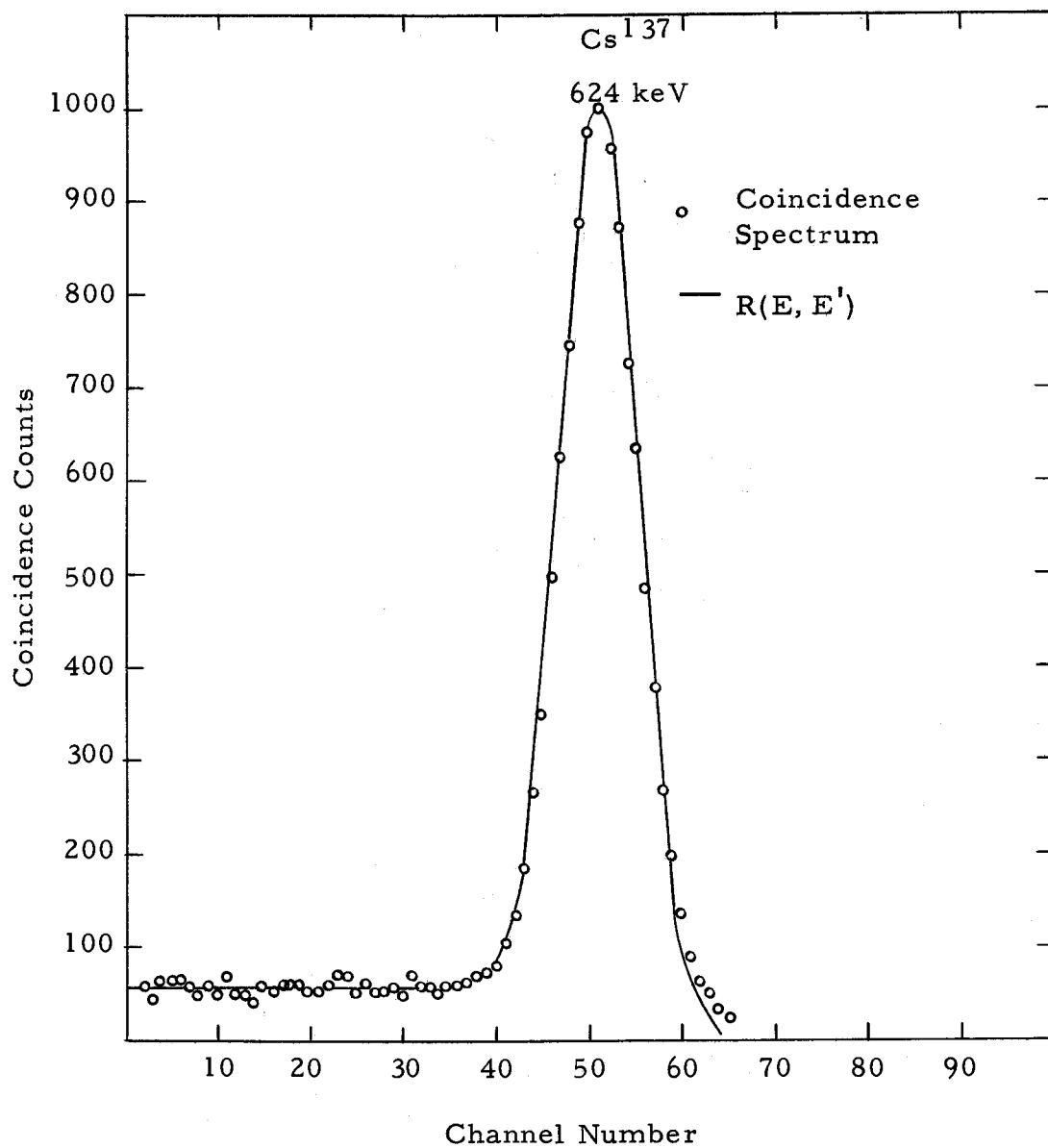


Figure 17. Beta-ray coincidence spectrum for Cs^{137} K-conversion electrons and the fit of the response function $R(E, E')$.

in the true energy spectrum while the high energy portion will be lacking counts. This effect of course can lead to an erroneous interpretation of the Kurie plot which will be discussed later. The energy response to the 624-keV conversion electron shown on Figure 17 actually represents the probability, $R(E, E')$, of recording the energy of an electron of energy E' in an energy interval E to $E + \Delta E$. Thus, it is imperative in the investigation of continuous beta-spectra to determine the energy response function $R(E, E')$ for various energies E' . The response function, $R(E, E')$, the experimental spectrum, $M(E)$ and the true energy spectrum, $N(E')$, are related by the following expression:

$$M(E) = \int_0^{E'} R(E, E') N(E') dE'. \quad (10)$$

Using the numerical approximation technique suggested by Freedman et al. (1956) and a high speed computer, the true energy spectrum can be determined from equation (10). This process is described completely in Appendix IV.

To determine the response function $R(E, E')$, line shapes from monoenergetic electrons were examined using beta-gamma coincidence techniques. The 624-keV K-conversion electron from Cs^{137} was isolated from the continuous beta-spectrum and the L-conversion electron by demanding coincidence between the conversion electron

and the Ba¹³⁷ K x-ray. In a similar study conversion electrons from Bi²⁰⁷ provided two additional lines. The 991-keV line of Bi²⁰⁷ (average energy of the K and L conversion electrons with K/L = 3.5) was observed in coincidence with the 570-keV gamma-ray while the 499-keV line (average energy of the K and L conversion electrons with K/L = 3.4) was separated by demanding coincidence with the 1064-keV gamma-ray. Figures 17, 18 and 19 show the coincidence spectra for these three energies, respectively. Note that the ratio of the height of the backscatter tail to the height of the photopeak is about the same for all three spectra.

Using these three experimentally determined line shapes and the arguments of Palmer and Laslett (1951) that the photopeak is approximately gaussian shaped and the half-width, α , at $1/e$ of the height of the photopeak varies as the square root of the electron energy E' , the following response function, $R(E, E')$, was constructed:

$$R(E, E') = \frac{k + (1 - m)e^{-(E - E')^2/\alpha^2}}{kE' + \alpha\sqrt{\pi} - \frac{1}{2}m\alpha\sqrt{\pi}} \quad (11)$$

where E' = maximum kinetic energy of the conversion electron,

k = constant for $0 \leq E \leq E'$,

k = 0 for all other E ,

m = constant for $E \leq E'$,

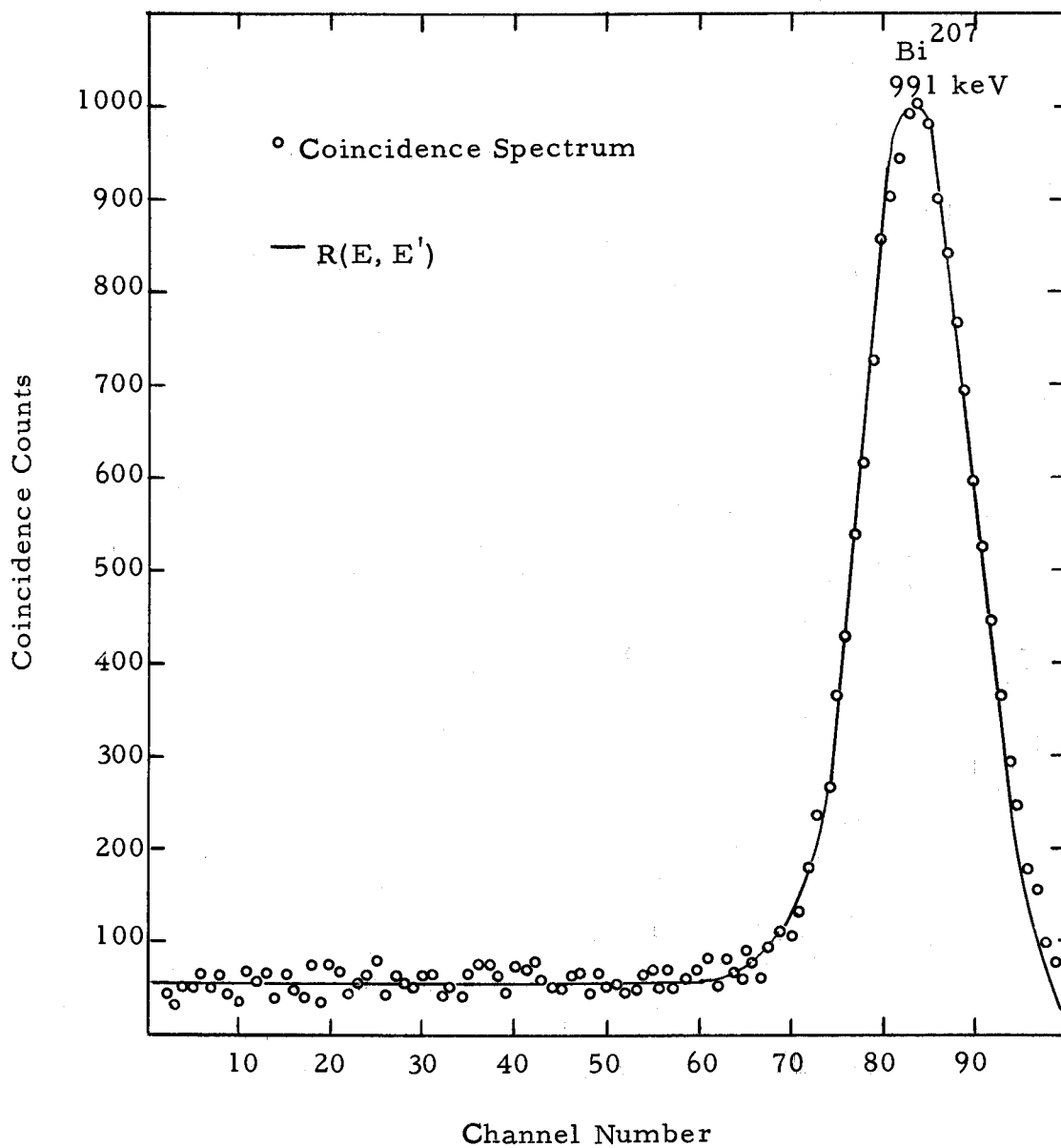


Figure 18. Beta-ray coincidence spectrum for Bi²⁰⁷ 991-keV conversion electrons and the fit to the response function $R(E, E')$.

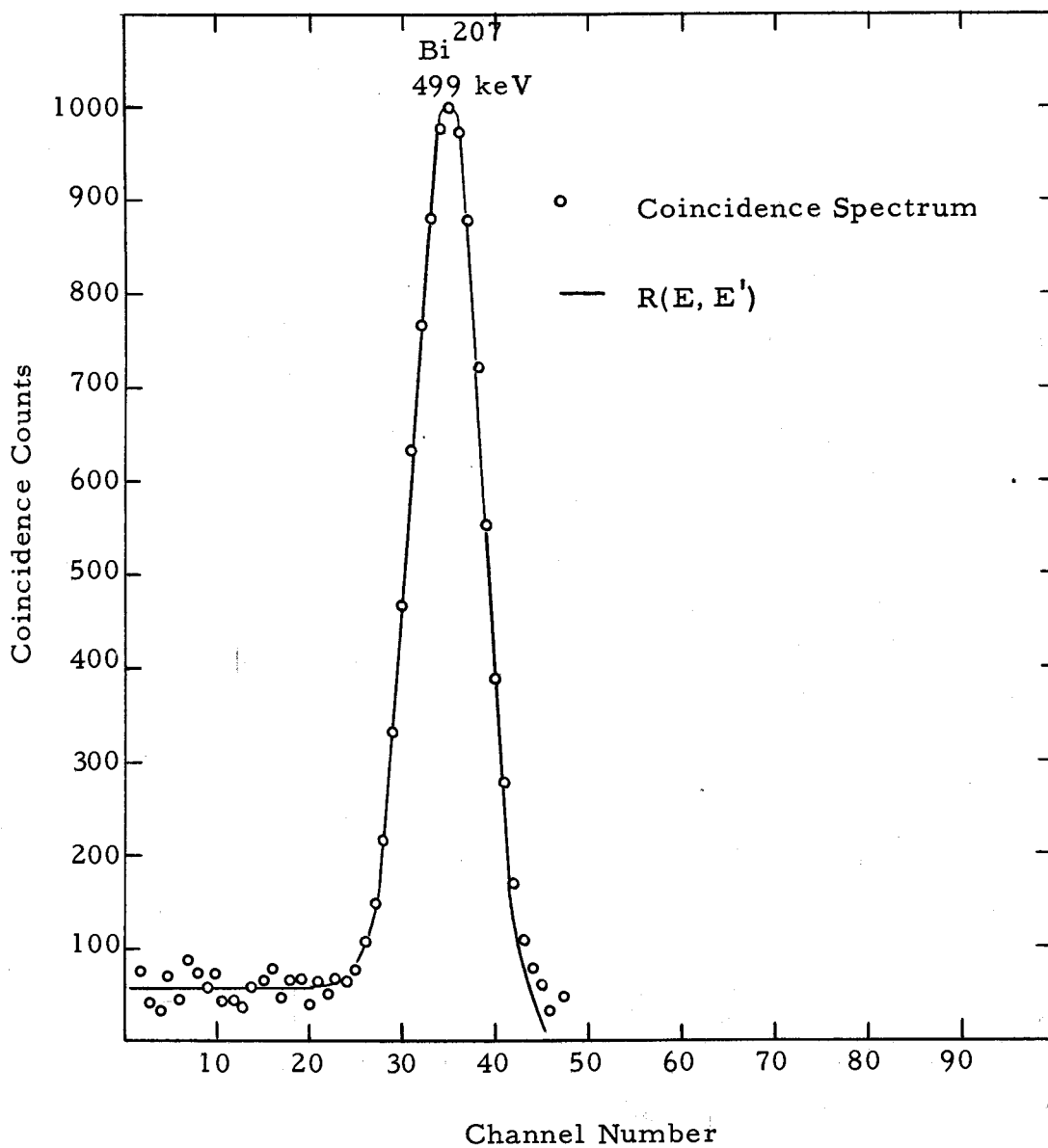


Figure 19. Beta-ray coincidence spectrum for Bi²⁰⁷ 499-keV conversion electrons and the fit of the response function $R(E, E')$.

$$m = 0 \text{ for } E > E',$$

$$a = a + b \sqrt{E'},$$

$$a = \text{constant},$$

$$b = \text{constant}.$$

This response function which has been normalized to unity was constructed in the following manner: For electron energies in the energy spectrum greater than E' , a pure gaussian function was fit, while on the low-energy side of E' , the response function consists of a constant intensity backscatter component of height k , the fractional height of the photopeak, extending from zero energy to the conversion electron energy E' , and a gaussian distribution. The gaussian distribution on the low energy side is the same as that fit to the high energy side of E' , but is multiplied by a constant $(1 - m)$ such that the sum of the gaussian component and the backscatter component will match the fit of the high energy side at E' . A non-zero value of 0.055 was determined from Figures 17, 18 and 19 for the parameters k and m which differ only in their range of definition. Included in each of the Figures 17, 18 and 19 is the fit of the response function $R(E, E')$ to the given spectrum.

Even though the response function formulated above fits the three line shapes in the energy region below 1000 keV quite well, its use in equation (10) and its application to higher energy regions was carefully checked. Its application to higher energy regions was

justified using sources of P^{32} and Y^{90} which have end-point energies of 1.704 MeV and 2.26 MeV, respectively. Before discussing this check, however, we must first consider the following.

From the theory of beta-decay the distribution of electron energies which arise from a continuous beta-emitter can be represented by (Howard, 1963):

$$N(W)dW = K'w(W)F(Z, W)pW(W_0 - W)^2dW, \quad (12)$$

where $N(W)dW$ = the number of electrons with energy in the interval W to $W + dW$,

W = total energy of electron emitted including its mass energy,

$w(W)$ = shape factor which is equal to unity for allowed transitions and equal to $(W^2 - 1) + (W_0 - W)^2$ for first forbidden transitions,

p = electron momentum,

W_0 = maximum electron energy,

$F(Z, W)$ = "Fermi Function" which takes account of the coulomb field of the daughter nucleus of atomic number Z .

Transforming equation (12) gives the following;

$$\frac{N(W)dW}{w(W)F(Z, W)pW} = K(W_0 - W)^2dW. \quad (13)$$

From equation (13) it is clear that a plot of $\left[\frac{N(W)}{w(W)F(Z, W)pW} \right]^{\frac{1}{2}}$ vs. W or $W - m_0c^2$ yields a linear curve in W . By extending this curve to

where $\left[\frac{N(W)}{w(W)F(Z, W)pW} \right]^{\frac{1}{2}}$ becomes zero, that is, at $W = W_0$, provides a means for determining the end-point energy, $W_0 - m_0 c^2$, of the electron. This is the plot which is defined as the Kurie plot in the analysis of continuous beta-spectra.

The Fermi functions, $F(Z, W)$, appearing above, functions of the atomic number, Z , of the daughter nucleus and the total energy W of the electron have been tabulated for numerous nuclei and electron energies (Siegbahn, 1964). In some cases rather than tabulating the Fermi function, $F(Z, W)$, however, a "reduced Fermi function", $f(Z, W)$, is listed which is related to the Fermi function $F(Z, W)$ by the following expression,

$$f(Z, W) = p^2 F(Z, W). \quad (14)$$

Thus, a plot of $\left[\frac{N(W)p}{w(W)f(Z, W)W} \right]^{\frac{1}{2}}$ vs. W gives the desired Kurie plot. The end-point energy is determined by substituting the true energy spectrum into the expression above for $N(W)$ and, using appropriate tabulated reduced Fermi functions, making a Kurie plot.

As mentioned previously the experimental approach and procedure used in this investigation was justified with sources of P^{32} and Y^{90} which have end-point energies of 1.704 MeV and 2.26 MeV, respectively. Calibrating the system with the conversion electrons from Bi^{207} and Cs^{137} , the experimental beta-spectra for sources of P^{32} and Y^{90} were recorded. Using the response function (11),

equation (10), and the procedure presented in Appendix IV, the true energy spectra for both sources were determined. Kurie plots, formed from these true energy spectra, were linear in energy (allowing for the forbidden shape of Y^{90}) and gave end-point energies of 1.70 MeV and 2.26 MeV for P^{32} and Y^{90} , respectively. These resulting end-point energies and linear Kurie plots rendered support for the response function and the correction process used to determine the true energy spectrum. Figures 20 and 21 show the Kurie plots for P^{32} and Y^{90} sources before and after subjecting the experimental spectra to the correction process. Clearly, without correcting for the energy response of the detector, the Kurie plots are not linear and lead to complications in determining the end-point energy and the nature of the decay, whether it is complex or not.

In a similar manner the end-point energy of the positron decaying from Mn^{51} to the ground state of Cr^{51} was measured. Since Mn^{51} is a positron emitter the beta-spectrum also contained a contribution due to annihilation radiation. The contribution to the beta-spectrum from the gamma-rays was determined by inserting a Lucite absorber between the source and the detector to absorb the beta-rays. Subtracting the gamma-spectrum from the composite gamma- and beta-ray spectrum recorded without the absorber produced the pure Mn^{51} beta-spectrum.

In analysing these continuous beta-spectra, the data points

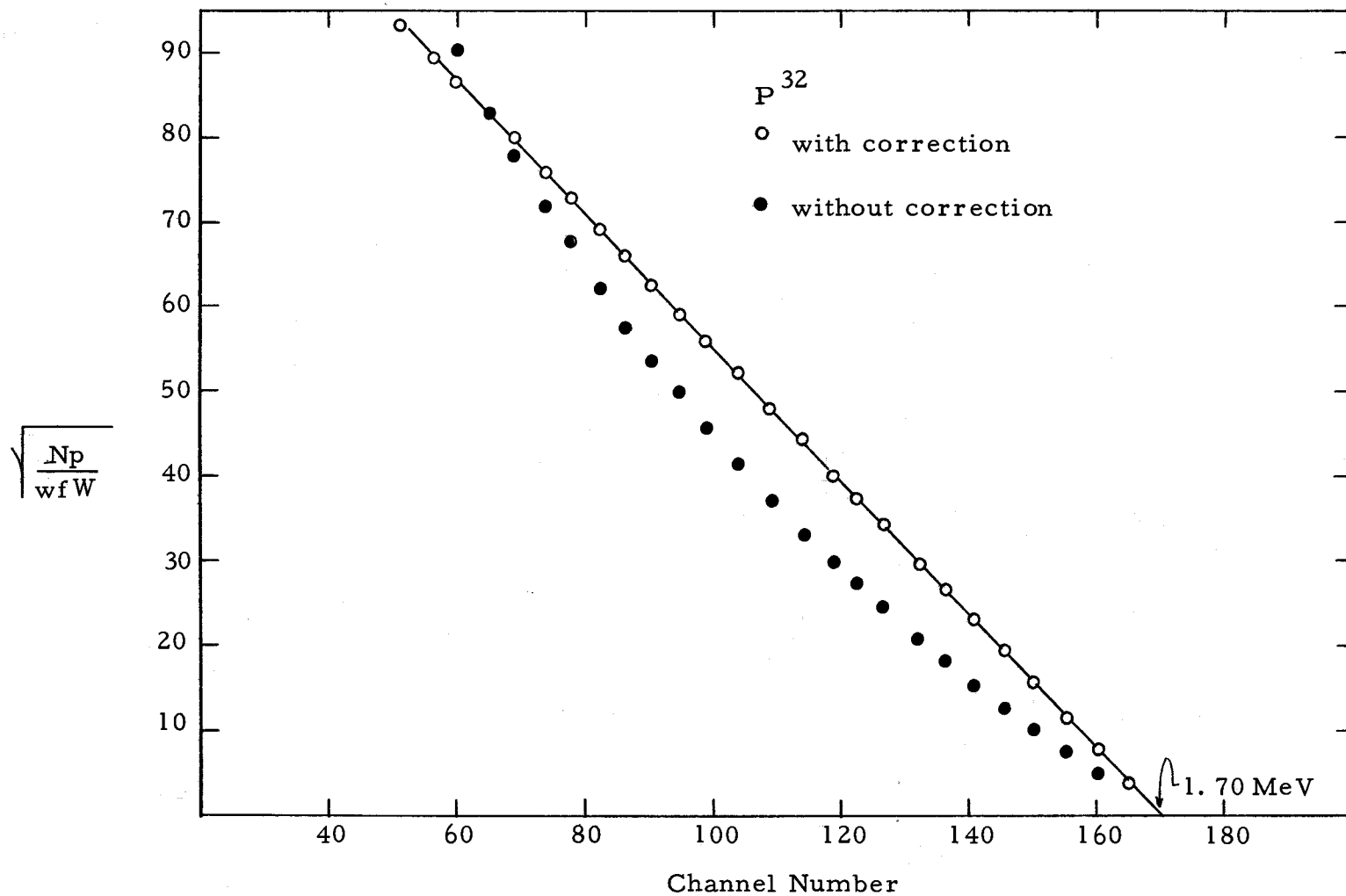


Figure 20. Kurie plots for P^{32} with and without correcting the experimental spectrum for the detector response.

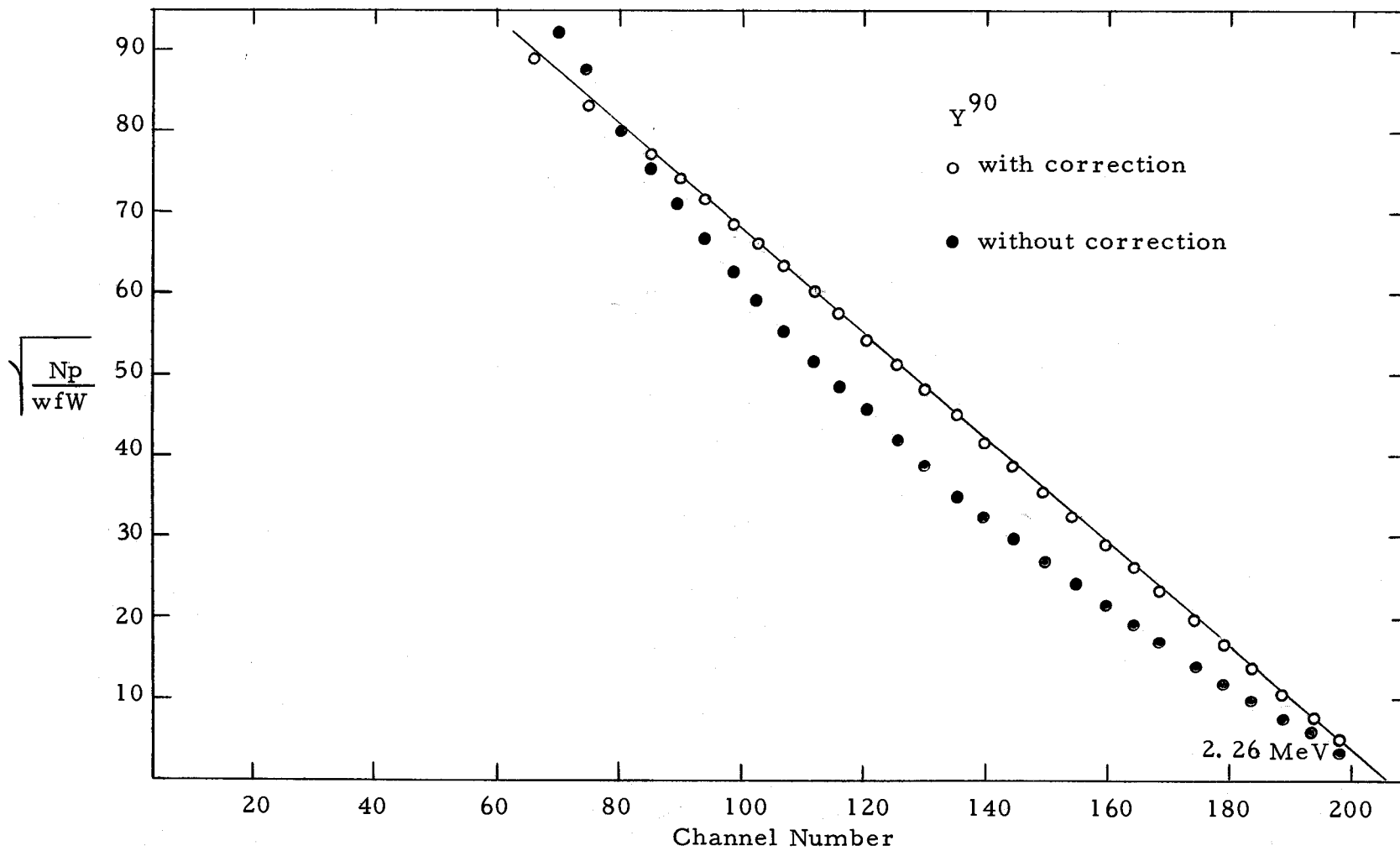


Figure 21. Kurie plots for Y⁹⁰ with and without correcting the experimental spectrum for the detector response.

were first fitted with a smooth curve calculated with a weighted least squares program as given in Appendix III and then corrected for the energy response of the detector from which a Kurie plot was made. Figure 22 shows a Mn^{51} experimental beta-spectrum and the fit of a smooth curve along with the true energy spectrum. Figure 23 gives the resulting Kurie plot which was energy calibrated with sources of Cs^{137} , Bi^{207} , P^{32} , and Y^{90} . Table 4 lists the experimental results of seven measurements of the Mn^{51} end-point energy from which an average value and error of 2.21 ± 0.02 MeV was determined.

Table 4. Experimental results of the end-point energy measurement for Mn^{51} .

Experimental Number	End-point Energy (MeV)
1	2.22
2	2.22
3	2.22
4	2.18
5	2.19
6	2.22
7	2.19

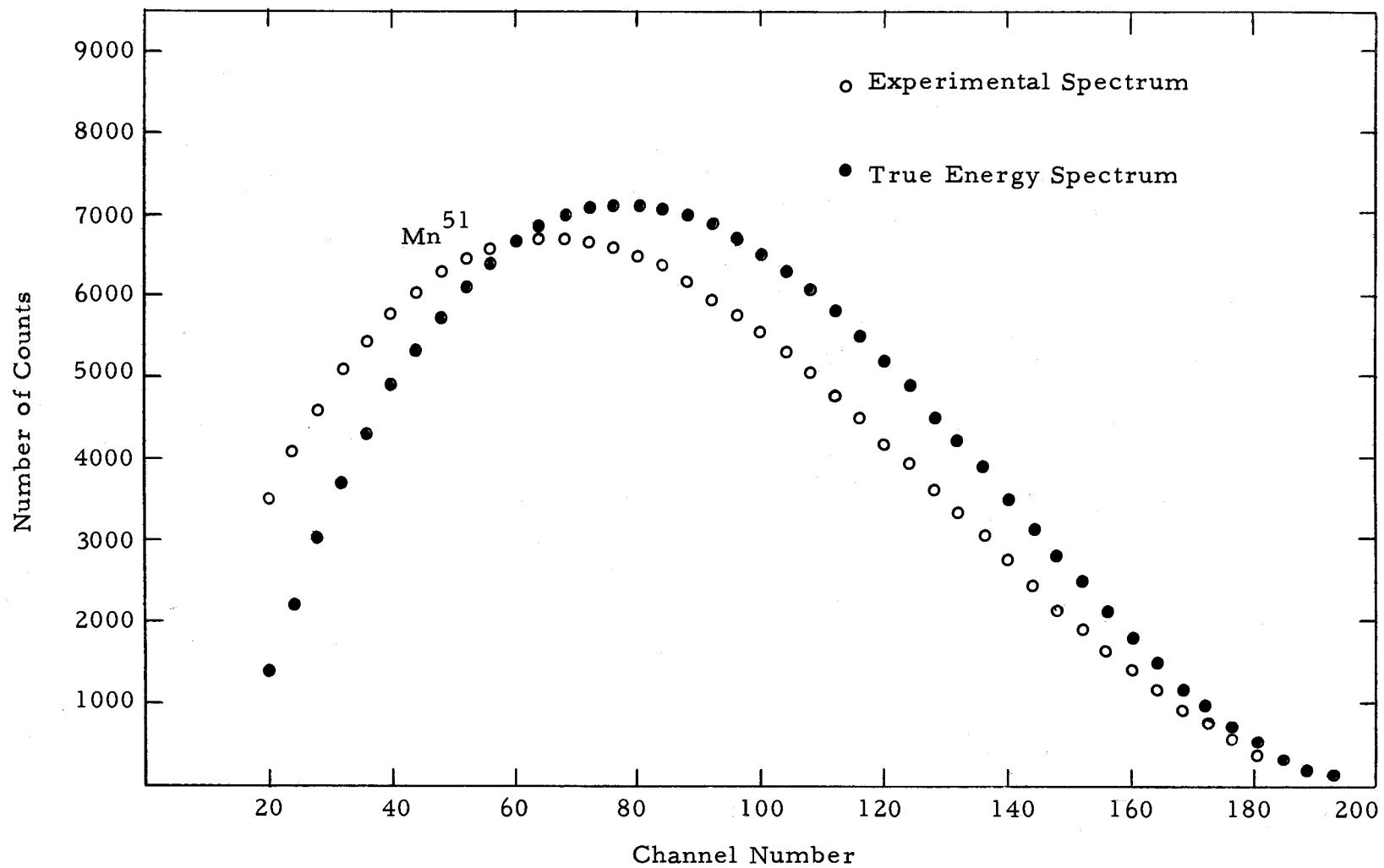


Figure 22. Mn⁵¹ experimental beta-spectrum and the calculated true energy spectrum.

$\sqrt{\frac{Np}{wfW}}$

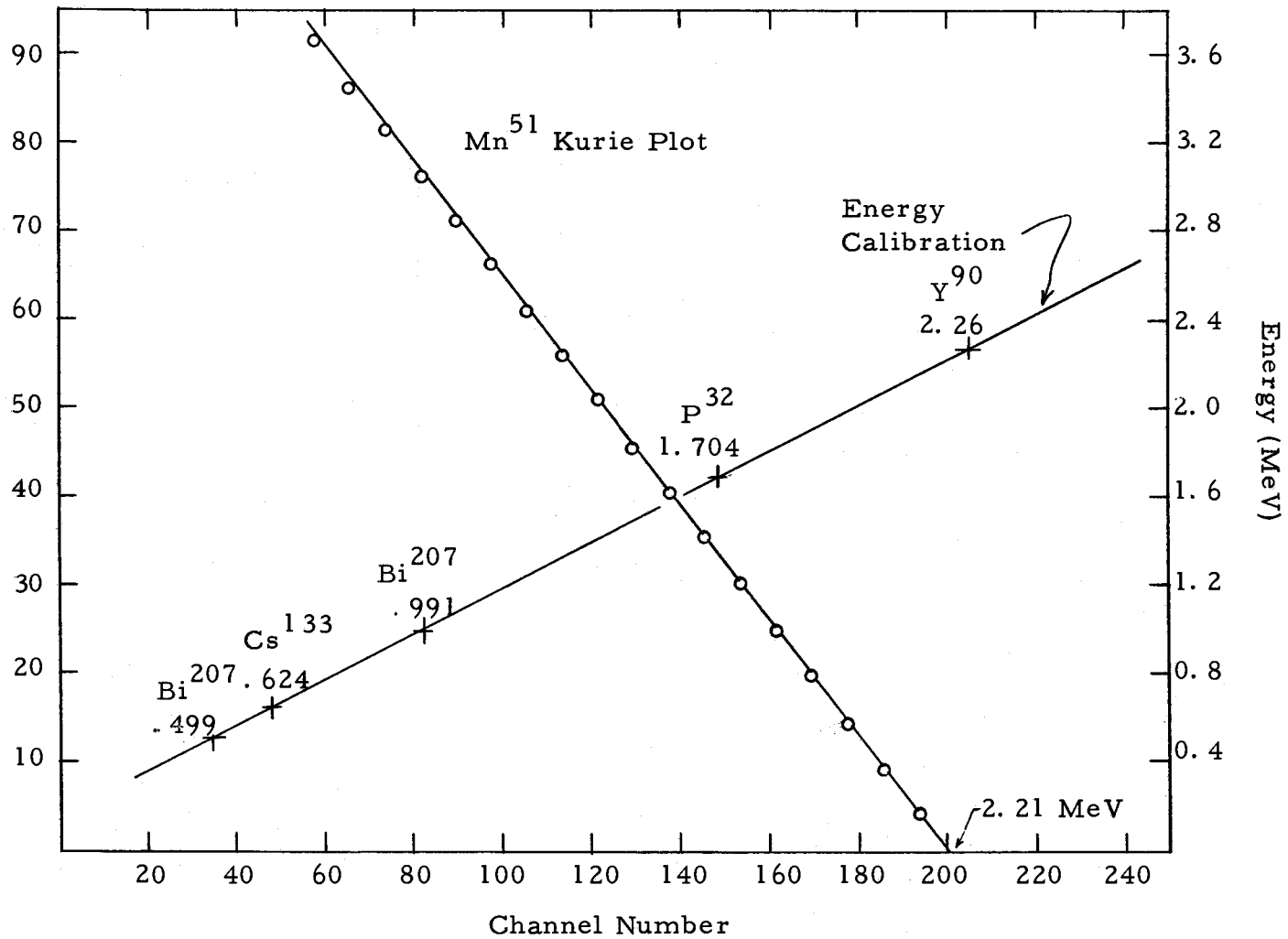


Figure 23. Mn⁵¹ Kurie plot and energy calibration curve.

MEAN-LIFE TIMES OF THE 761-keV AND 1170-keV LEVELS OF Cr-51

Apparatus

The mean-lives of the 761-keV and 1170-keV levels of Cr⁵¹ were investigated with a delayed coincidence spectrometer. A detailed description of this spectrometer, the procedure for time calibration, and the methods used in interpreting the experimental results are given by Sommerfeldt (1964).

Experiment and Results

Sources of Mn⁵¹ were first placed between two aluminum absorbers, each having a 2.5 cm thickness which was sufficient to stop the most energetic positons. The sources were then mounted between two gamma-ray detectors which had an angular separation of 180°.

For the mean-life measurement of the 761-keV level, the spectrometer was gated on the coincidence between the 511-keV annihilation and the 761-keV gamma-rays. The delayed coincidence spectrum obtained for Cr⁵¹ is shown in Figure 24 along with a prompt coincidence curve obtained for Na²² using the same spectrometer settings. Measuring the slope of the delayed coincidence spectrum in the region beyond the prompt coincidence curve using

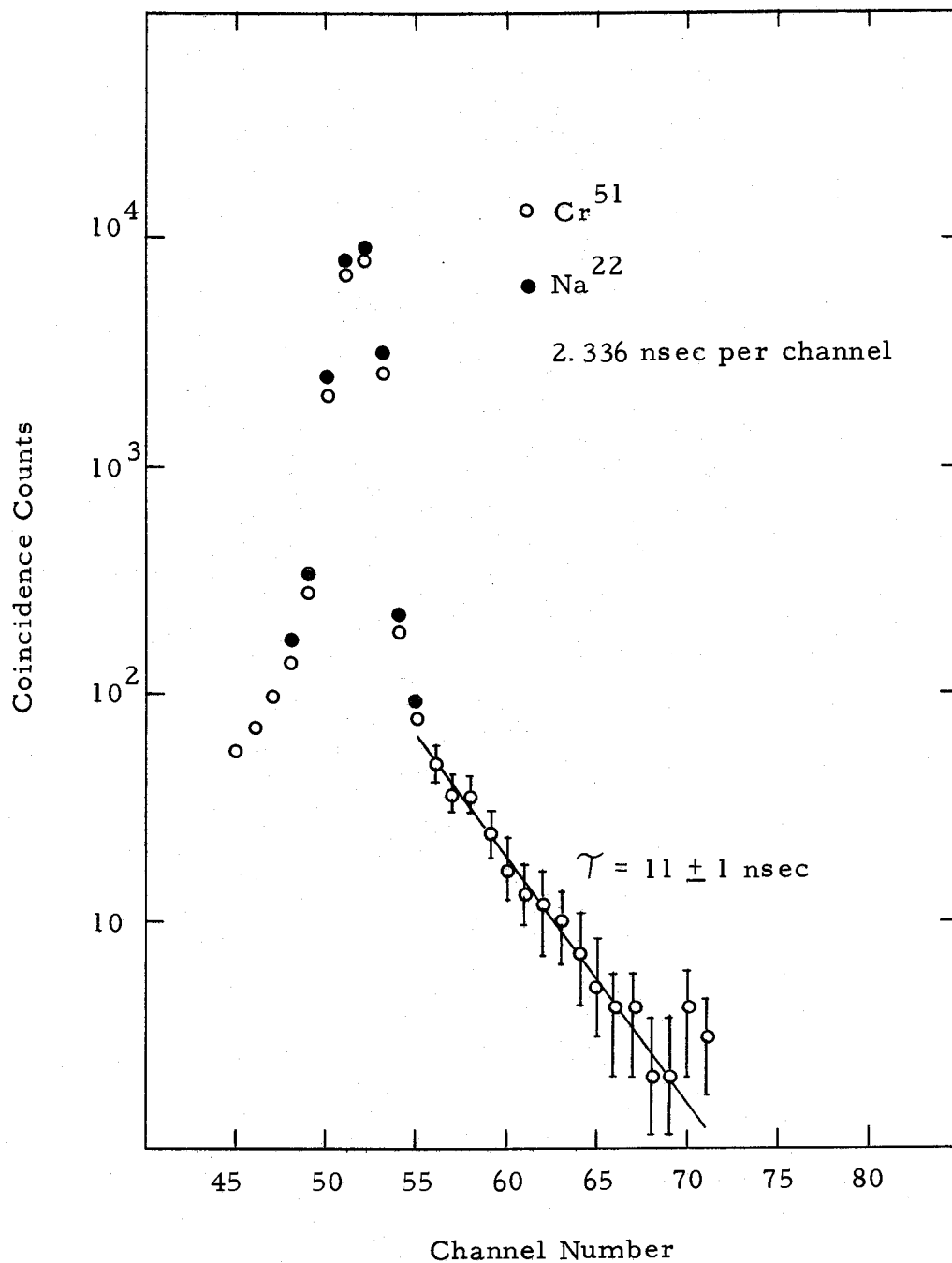


Figure 24. Delayed coincidence spectrum for the 761-keV level of Cr⁵¹ and the prompt coincidence curve for Na²².

the method of least squares provided a means for determining the mean-life of the 761-keV level. From Figure 24 a mean-life of 11 ± 1 nsec was measured for this level.

In a similar manner the mean-life of the 1170-keV level was investigated. For this measurement the spectrometer was gated on the coincidence between the 511-keV and 1170-keV gamma-rays; this procedure yielded a delayed coincidence spectrum which did not differ from the prompt coincidence curve obtained for Na^{22} using the same spectrometer settings. Both coincidence spectra are shown in Figure 25 from which the mean-life of the 1170-keV level of Cr^{51} has been estimated to have an upper-limit of one nanosecond.

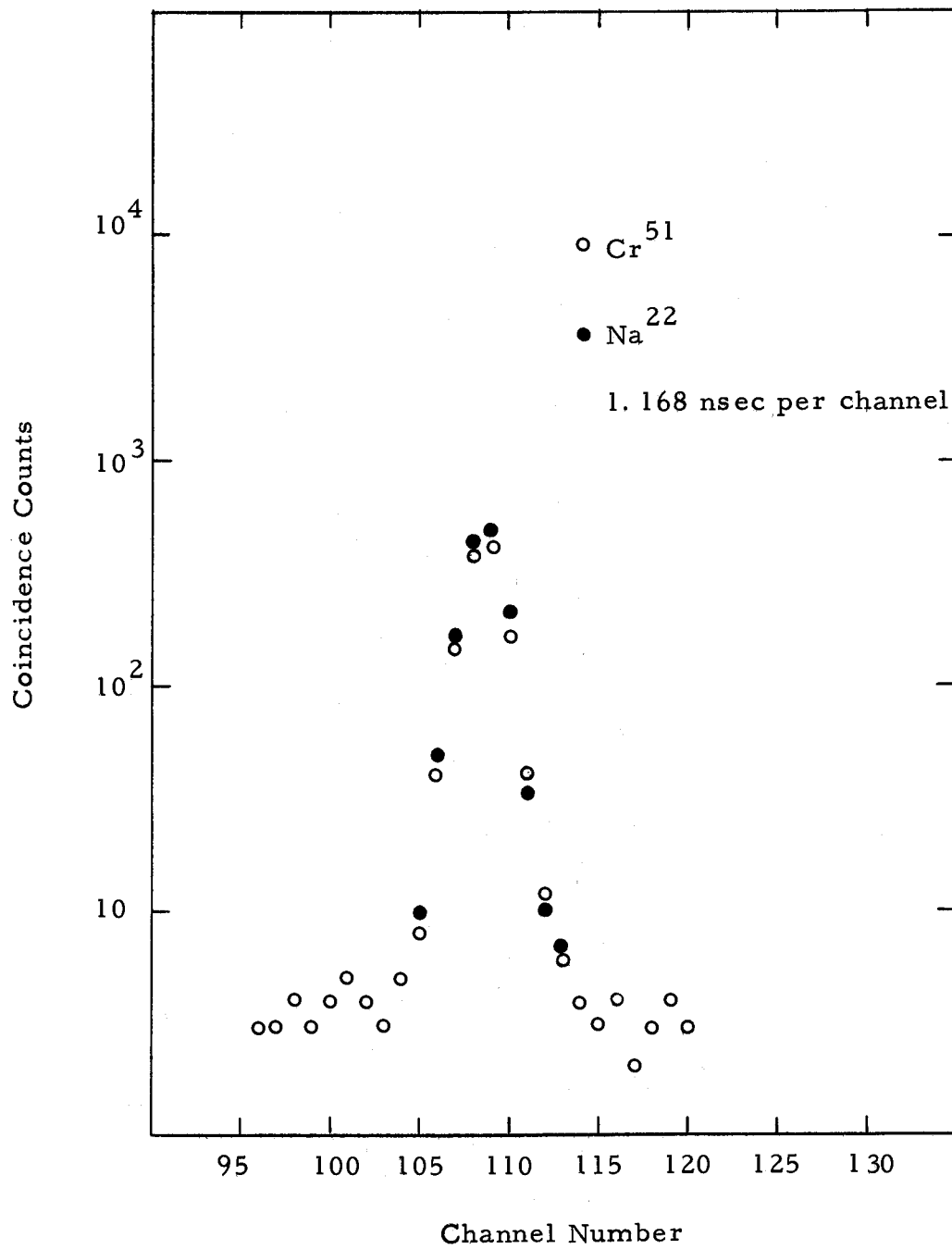


Figure 25. Delayed coincidence spectrum for the 1170-keV level of Cr⁵¹ and the prompt coincidence curve for Na²².

CONCLUSIONS

The experimental results discussed in the previous sections are combined with theory in this section in order to make spin and parity assignments for the ground state of Mn^{51} and to the low-lying levels of Cr^{51} inasmuch as spin and parity are the nuclear parameters which one compares with the predictions of the shell model. To make these assignments, however, additional properties are required which can be calculated from theory using the experimental results as a basis. Among these properties are the log ft values, transition probability ratios, branching intensities, mean-life times of excited nuclear states, and the multipolarity of the gamma-radiation. Log ft values, the common logarithm of the comparative half-periods, ft, are fundamental in determining the character of beta-decay, that is, the degree of forbiddenness of the transition. Beta-transitions are classified as allowed for log ft values in the region 3 to 6 and first-forbidden for values in the range 6 to 10. According to Gamow-Teller selection rules, allowed transitions have no parity change and spin changes limited to 0 or ± 1 units, while first-forbidden transitions have a parity change and spin changes restricted to 0, ± 1 , or ± 2 units. The comparative half-period, ft, appearing in log ft, is the product of the integral Fermi function, f, and the partial half-period, t, of the transition.

Transition probability ratios which are necessary in determining the branching intensities simply compare the probabilities for electron capture and positron emission to a definite energy state. The branching intensity is defined as the fractional number of transitions going to a particular energy level for a given number of decays. This includes transitions by electron capture and positron emission if the latter is energetically possible. The mean-life time of an excited nuclear state is defined as the average time interval that a nucleus remains in a specific energy level before decaying by gamma-emission to a lower energy state. Gamma-radiation emitted in the decay can be either electric or magnetic multipole radiation with different orders of multipolarity. The multipolarity and the mean-life time are related; the longer the life-time, the higher the order of the multipolarity. Associated with multipole radiation are definite rules governing changes of parity and spin. For this reason one attempts to determine the multipolarity of the radiation emitted and to distinguish between electric and magnetic radiation in order that spin and parity assignments can be made. In the discussion which follows, numerical values are determined and tabulated for the parameters which characterize the strong transition to the ground state of Cr^{51} and the weak population of the 761-keV and 1170-keV levels of Cr^{51} in the decay of Mn^{51} . In some cases, however, numerical values have been calculated for the parameters

describing possible transitions to energy states higher than 1170-keV in Cr^{51} . This has been done mainly to justify why evidence of these transitions are not observed in this experiment. The decay scheme shown in Figure 26 summarizes the results of this section along with the experimentally determined properties previously discussed.

Basic to the calculation of log ft values and branching intensities for transitions to each level shown in Figure 26 are the ratios of the transition probabilities for electron capture to positon emission, or equivalently, the ratios of the integral Fermi functions for electron capture to positon emission. Tabulated values for these ratios calculated from theory exist for a certain number of positon energies and daughter nuclei. For intermediate energies and atomic numbers one is required to use linear interpolation. The procedure followed here utilizes the tabulated ratios and linear interpolation method given by Wapstra et al. (1959). Table 5 lists the results. In addition to the ratio of the transition probabilities for electron capture to positon emission, denoted by f_{ϵ}/f_{+} , the quantities f_{ϵ}/f and f_{+}/f , the ratios of the electron capture and positon emission transition probabilities to the total transition probability, respectively, also are included. The integral Fermi function, f , is just the sum of f_{ϵ} and f_{+} . For transitions to energy states higher than 2.03 MeV in Cr^{51} , positon emission is energetically forbidden and the decay is by pure electron capture. This fact is indicated in

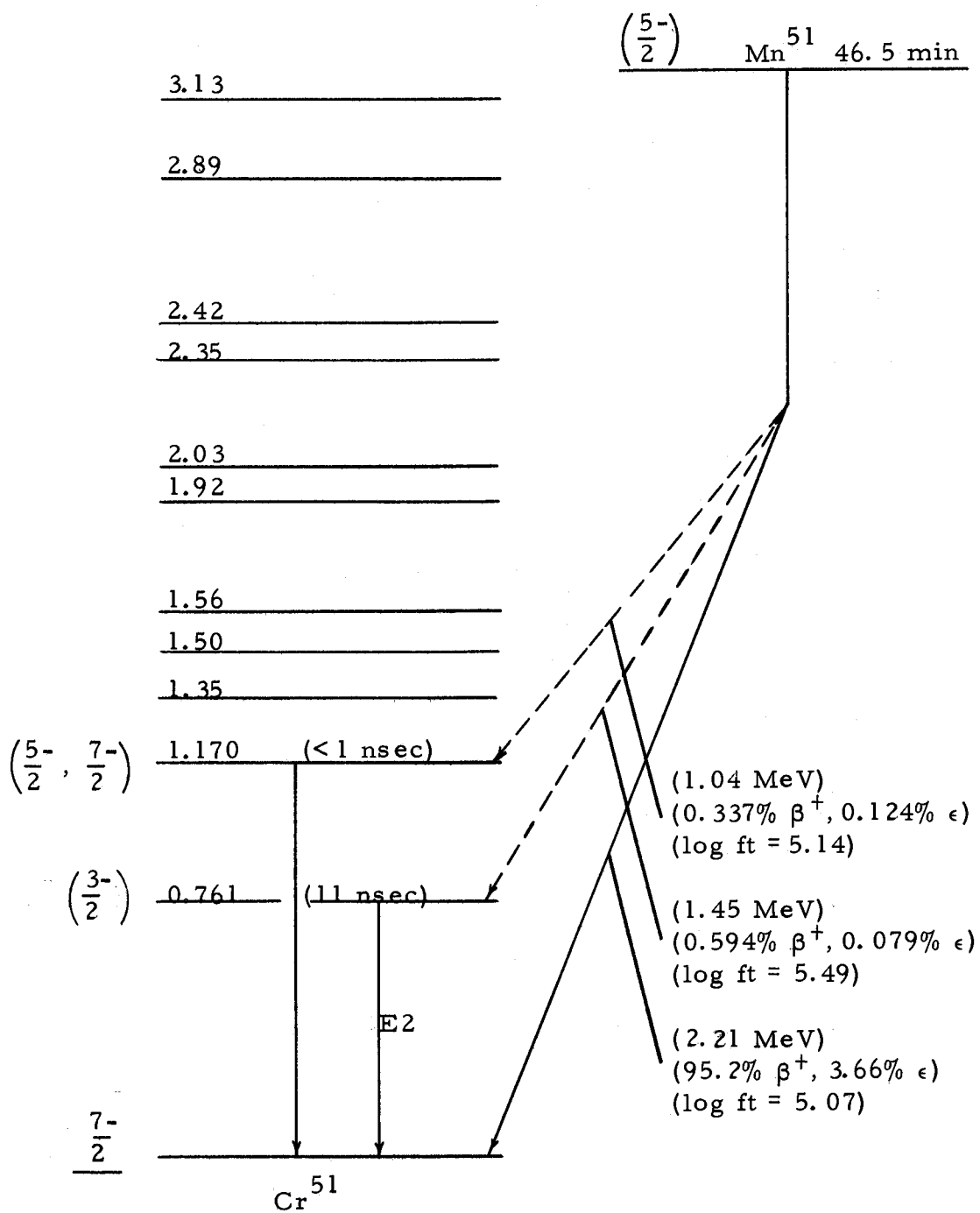


Figure 26. Decay scheme for Mn⁵¹ (present investigation).

Table 5 by the values of unity and zero for f_{ϵ}/f and f_{+}/f , respectively.

Table 5. Ratios of transition probabilities for electron capture and positron emission.

Transition to (MeV level)	f_{ϵ}/f_{+}	f_{ϵ}/f	f_{+}/f
Ground state	0.038	0.037	0.963
0.761	0.134	0.118	0.882
1.170	0.370	0.270	0.730
1.35	0.671	0.402	0.598
1.50	1.230	0.552	0.448
1.56	1.630	0.620	0.380
1.92	24.40	0.961	0.039
2.03	157.0	0.994	0.006
2.35	∞	1.0	0.0
2.42	∞	1.0	0.0
2.89	∞	1.0	0.0
3.13	∞	1.0	0.0

The determination of the transition probability ratios, f_{ϵ}/f , is the first step in obtaining values for the parameter $\log ft$. Using the ratios f_{ϵ}/f given in Table 5 and numerical values for f_{ϵ} permits the calculation of definite values for the function f for transitions to the ground state and first two excited levels of Cr^{51} . The following expression (Evans, 1955) provides a means of calculating the

quantities f_{ϵ} ,

$$f_{\epsilon} = 2\pi \left[\frac{Z}{137} \right]^3 \left[\frac{2+S}{\Gamma(3+2S)} \right] (W_0 + 1 + S)^2 \text{sec}^{-1}, \quad (15)$$

where Z = atomic number of the parent nucleus,

$$S = \left\{ 1 + \left[\frac{Z}{137} \right]^2 \right\}^{\frac{1}{2}} - 1,$$

$$W_0 = \frac{E_{\text{max}}}{m_0 c^2} + 1,$$

$m_0 c^2$ = rest mass energy of an electron,

E_{max} = maximum energy available for positron emission.

The resulting values for f are listed in Tables 7 and 8.

To determine the factor t in the comparative half-period, ft , requires additional information concerning the branching intensities. From the ratio of the transition probabilities and the experimentally determined gamma-ray relative intensities, the branching intensities for transitions to the ground state and to the first two excited levels of Cr^{51} can be computed. Let B_1 , B_2 , and B_3 denote the branching intensities for these transitions, respectively, and let I_2 and I_3 represent the intensity of the 761-keV and 1170-keV gamma-rays relative to the number of emitted positons, respectively. Finally, denote the ratios f_+/f given in Table 5 by R_1 , R_2 , and R_3 for transitions to the ground state and the first two excited levels of Cr^{51} ,

respectively. The branching intensities are related by the following set of simultaneous equations, the solution of which yields values for B_1 , B_2 , and B_3 .

$$\left. \begin{aligned} B_1 + B_2 + B_3 &= 1 \\ \frac{B_2}{B_1 R_1 + B_2 R_2 + B_3 R_3} &= I_2 \\ \frac{B_3}{B_1 R_1 + B_2 R_2 + B_3 R_3} &= I_3 \end{aligned} \right\} \quad (16)$$

From the total branching intensities B_1 , B_2 , and B_3 , and the ratios f_+/f and f_ϵ/f which appear in Table 5, the branching intensities for electron capture and positron emission can be determined. That is, for transitions to a particular energy state, one can specify the fractional number of decays which go by positron emission and the number which go by electron capture. The results for the decay of Mn^{51} are presented in Table 6.

Table 6. Branching intensities for transitions to the ground state and first two excited levels of Cr^{51} .

Transition to	Total Branching Intensity %	Positron Branching Intensity %	Electron Capture Branching Intensity %
Ground State	98.9	95.2	3.66
761-keV Level	0.673	0.594	0.079
1170-keV Level	0.461	0.337	0.124

The partial half-period, t , for transitions to each of the levels described above is determined from the ratio of the experimentally measured half-life and the corresponding total branching intensity. Table 7 lists these values along with the functions f and the comparative half-periods, ft . Since it is customary to compare the character of beta-emission by $\log ft$ rather than ft , values for $\log ft$ also are included in Table 7.

Table 7. Comparative half-periods and $\log ft$ values.

Transition to	f (sec^{-1})	t (sec)	ft ($\times 10^5$)	$\log ft$	Transition Character
Ground State	41.3	2,830	1.17	5.07	Allowed
761-keV Level	0.755	415,000	3.13	5.49	Allowed
1170-keV Level	0.299	606,000	1.39	5.14	Allowed

As previously stated, beta-decay is classified as allowed for $\log ft$ values in the range 3 to 6, and first-forbidden for the range 6 to 10. Table 7 indicates that the transitions to the ground state and first two excited levels of Cr^{51} are definitely allowed which, according to Gamow-Teller selection rules, means no parity change and that ΔI , the spin change, is limited to the values 0 or ± 1 . This information will be useful in making the spin and parity assignments to the ground state of Mn^{51} and to the low-lying levels of Cr^{51} .

Although the population of energy states higher than the 1170-keV level in Cr^{51} was not observed in this investigation, it is

interesting to estimate the branching intensity to these levels on the basis that each transition is allowed, that is, assuming a log ft value of 5 for each transition. Using the ratios f_{ϵ}/f listed in Table 5 and the calculated values for f_{ϵ} permits the determination of the theoretical branching intensities for transitions from Mn^{51} to these levels. The results are listed in Table 8.

Table 8. Theoretical branching intensities.

Transition to (MeV level)	f_{ϵ}/f	f ($\text{sec}^{\epsilon-1}$)	f (sec^{-1})	Branching Intensity (%)
1.35	0.402	51.5×10^{-3}	12.8×10^{-2}	0.354
1.50	0.552	43.6×10^{-3}	79.0×10^{-3}	0.220
1.56	0.620	40.6×10^{-3}	65.4×10^{-3}	0.183
1.92	0.961	24.9×10^{-3}	25.9×10^{-3}	0.072
2.03	0.994	20.8×10^{-3}	21.0×10^{-3}	0.059
2.35	1.0	11.1×10^{-3}	11.1×10^{-3}	0.031
2.42	1.0	93.7×10^{-4}	93.7×10^{-4}	0.026
2.89	1.0	16.7×10^{-4}	16.7×10^{-4}	0.005
3.13	1.0	11.3×10^{-5}	11.3×10^{-5}	0.003

If any of these states are populated in the decay of Mn^{51} , the weak branching intensity coupled with the low detector efficiency for gamma-rays in this range certainly indicates that detection would be quite difficult. Despite these difficulties Baskova et al. (1962) reported the observation of two weak gamma-rays from the higher states in the decay of Mn^{51} . They measured gamma-ray energies

of 1.56 MeV and 2.03 MeV which correspond to branching to the fifth and seventh excited levels of Cr^{51} , respectively. They also measured the relative intensities of these gamma-rays to be 1.0 percent and 0.5 percent of the positons, respectively. Converting these relative intensities to equivalent branching intensities and comparing the results with the values in Table 8 indicates the intensity measurements of Baskova et al. are an order of magnitude larger than expected. In addition to this discrepancy, Baskova and co-workers make no mention of observing the more intense 761-keV and 1170-keV gamma-rays previously reported by Nozawa et al. (1960) and also observed in this investigation.

Before establishing the spin and parity assignments for the decay scheme of Mn^{51} , the calculation of one additional parameter is required, namely, the mean-life times of the 761 keV and 1170-keV levels of Cr^{51} . These values of course depend upon knowing whether the gamma-radiation is electric or magnetic multipole and the multipolarity of the emitted radiation which results from the decay of these levels. Theoretical expressions for the mean-life times have been formulated by Weisskopf (1951) and are written below. The first expression gives the mean-life time for electric multipole radiation while the second is for magnetic multipole radiation,

$$T_e(\ell) = \frac{\ell[(2\ell + 1)!!]^2}{4 \cdot 4(\ell + 1)} \left[\frac{\ell + 3}{3} \right]^2 \left[\frac{197 \text{ MeV}}{E_\gamma} \right]^{2\ell + 1} \frac{10^{-21} \text{ sec}}{(1.4A^{1/3})^{2\ell}} \quad (17)$$

$$T_m(\ell) = \frac{\ell[(2\ell + 1)!!]^2}{1.9(\ell + 1)} \left[\frac{\ell + 3}{3} \right]^2 \left[\frac{197 \text{ MeV}}{E_\gamma} \right]^{2\ell + 1} \frac{10^{-21} \text{ sec}}{(1.4A^{1/3})^{2\ell - 2}}$$

where $\ell = \Delta I$, is the absolute value of the difference in spin between the initial and final states,

E_γ = energy of emitted gamma-ray in MeV,

A = atomic number of the nucleus.

Table 9 contains numerical values for T_e and T_m for transitions of various multiplicities from the 761-keV and 1170-keV levels to the ground state of Cr^{51} . Comparison of the measured life-times for these states with the values given in Table 9 assist in determining the spin and parity of the first two excited states of Cr^{51} .

Table 9. Theoretical mean-life times for the 761-keV and 1170-keV levels of Cr^{51} for various gamma-ray multiplicities.

Type of Transition	Parity Change	Mean-life for the 761-keV level (sec)	Mean-life for the 1170-keV level (sec)
E1	Yes	1.17×10^{-15}	3.20×10^{-16}
M1	No	7.33×10^{-14}	2.01×10^{-14}
E2	No	1.52×10^{-10}	1.76×10^{-11}
M2	Yes	9.50×10^{-9}	1.10×10^{-9}
E3	Yes	2.99×10^{-5}	1.46×10^{-6}
M3	No	1.87×10^{-3}	9.12×10^{-5}

The spin and parity of the ground state of Cr^{51} have been well established as $\frac{7-}{2}$ in agreement with the shell model prediction for the closed $1f_{7/2}$ shell minus one configuration. Using atomic-beam magnetic resonance techniques, Childs and co-workers (1959) measured the nuclear spin of Cr^{51} as $\frac{7}{2}$ while Zeidman et al. (1960) determined the parity from (d, t) reactions on Cr^{52} . The latter investigation determined the orbital angular momentum l_n of the odd neutron to be 3 with no mixture of $l_n = 1$, indicating the ground state to be a pure $1f_{7/2}$ level.

For the purpose of comparing theory with experiment, the nuclear level structure with spin-orbit coupling, which is fundamental in the description of the nuclear shell model, is illustrated in Figure 27 (Mayer and Jensen, 1955). The levels on the left, which do not include the spin-orbit splitting, are intermediate between the levels for a pure isotropic harmonic oscillator potential and those for an infinite square well potential. Utilizing the concept of spin-orbit coupling and the potential wells listed above, Maria Mayer was able to formulate a nuclear model capable of explaining the "magic numbers". In addition to giving an adequate explanation of the magic numbers, the nuclear shell model has been quite successful in predicting the spin and parity of the ground state of odd A nuclei, particularly for isotopes with nucleon numbers in the range 20 to 28. Table 10 lists the proton and neutron configurations for odd A nuclei

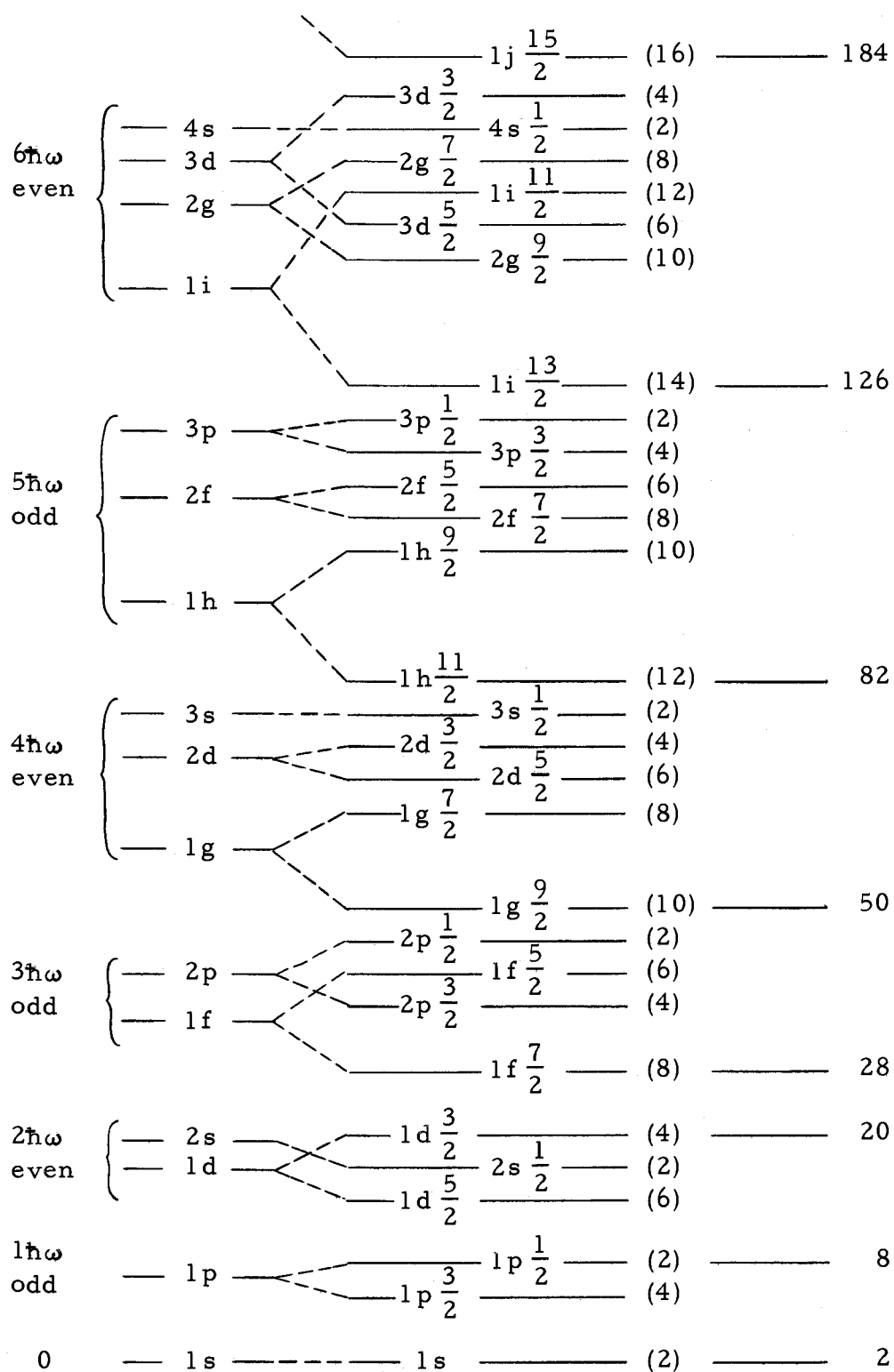


Figure 27. Shell model nuclear level structure with spin-orbit coupling.

Table 10. Ground state configurations for nuclei in the $1f_{7/2}$ region.

Odd Z	Even N	Proton Configuration	Spin and Parity
(20) $(1d_{5/2}), (2s_{1/2})$ and $(1d_{3/2})$ levels filled			
21	Sc 22	$(f_{7/2})^1$	$\frac{7}{2}^-$
	Sc 24	$(f_{7/2})^1$	$\frac{7}{2}^-$
23	V 26	$(f_{7/2})^3$	$\frac{7}{2}^-$
	V 28	$(f_{7/2})^3$	$\frac{7}{2}^-$
25	Mn 28	$(f_{7/2})^5$	$\frac{7}{2}^-$
	Mn 30	$(f_{7/2})^5_{5/2}$	$\frac{5}{2}^-$
27	Co 30	$(f_{7/2})^7$	$\frac{7}{2}^-$
	Co 32	$(f_{7/2})^7$	$\frac{7}{2}^-$
Odd N	Even Z	Neutron Configuration	Spin and Parity
23	Ca 20	$(f_{7/2})^3$	$\frac{7}{2}^-$
23	Ti 22	$(f_{7/2})^3$	$\frac{7}{2}^-$
25	Ti 22	$(f_{7/2})^5_{5/2}$	$\frac{5}{2}^-$
27	Ti 22	$(f_{7/2})^7$	$\frac{7}{2}^-$
27	Cr 24	$(f_{7/2})^7$	$\frac{7}{2}^-$
(28) $(1f_{7/2})$ level filled			

with proton and neutron numbers in the region 20 to 28 and the corresponding experimentally determined spin and parity assignments for the ground states of these nuclei (Siegbahn, 1964). According to Figure 27 the filling of the $1f_{7/2}$ level occurs in this region and one expects, from the simple pairing shell model prediction, the ground state spin and parity assignments for nuclei in this region to be $\frac{7^-}{2}$. With the exceptions of Mn^{55} , Ti^{47} , and perhaps Cr^{49} , theory and experiment agree. The latter isotopes, with $\frac{5^-}{2}$ ground state configurations, are classified as anomalies in the theory of the shell model. An interesting observation is that all three isotopes have either five protons or neutrons beyond the closed shell of 20 and that the first two have two neutrons and protons, respectively, beyond the closed shells of 28 and 20. The Cr^{49} isotope has four protons beyond the closed shell of 20. However, Mn^{53} with five protons beyond the closed shell of 20 and a closed neutron shell of 28 has a measured $\frac{7^-}{2}$ ground state configuration which is consistent with the shell model prediction. It appears that the coupling of the even nucleon numbers beyond the closed shells destroys the expected $\frac{7^-}{2}$ single particle configuration in favor of the $\frac{5^-}{2}$ coupling for the odd nucleon number five associated with the three anomalies listed above. As yet, however, a satisfactory theoretical explanation of this phenomenon does not exist.

On the basis of the simple pairing shell model one expects Mn^{51}

to have a $\frac{7^-}{2}$ ground state spin and parity assignment, but on the other hand, comparison with the three anomalies listed above, one might predict a $\frac{5^-}{2}$ ground state assignment since Mn^{51} has five protons beyond the closed shell of 20 and two neutron holes from the closed shell of 28, a configuration similar to Ti^{47} assuming holes and particles behave in the same manner. In the following discussion arguments are given which support the assignment of $\frac{5^-}{2}$.

The log ft value for the decay of Mn^{51} to the ground state of Cr^{51} , calculated as 5.07, certainly indicates this transition is allowed. The $\frac{7^-}{2}$ configuration for the Cr^{51} ground state and the Gamow-Teller selection rules for allowed transitions restrict the possible ground state assignment for Mn^{51} to the values $\frac{5^-}{2}$, $\frac{7^-}{2}$, or $\frac{9^-}{2}$.

Kane and co-workers (1962) using thermal neutron capture in Cr^{50} to study the level structure of Cr^{51} observed a strong 8.499-MeV capture gamma-ray transition to the 761-keV level of Cr^{51} .

Using the following reasoning they concluded the capture gamma-ray to have an E1 character:

From the systematics of capture-gamma-ray transition probabilities it is known that the great majority of strong, high-energy transitions have dipole character, chiefly E1. Furthermore, in the region near $A \sim 55$ the energy of the 3s single-particle level is close to the neutron binding energy, so that strong E1 transitions are expected to occur between the state formed in neutron capture and low-lying p states of the residual nucleus. Experimentally, capture-gamma-ray spectra in this

region are characterized by exceptionally intense transitions to low-lying levels.

The Cr^{51} state formed by thermal neutron capture in the even-even nucleus of Cr^{50} has the intrinsic spin and parity of the captured neutron, that is, $\frac{1}{2}^+$. Assuming the 8.499-MeV transition from this $\frac{1}{2}^+$ level to the 761-keV level of Cr^{51} is E1, the spin of the 761-keV level is either $\frac{1}{2}$ or $\frac{3}{2}$ since a spin change of one unit is associated with E1 transitions. If the spin for the 761-keV level is taken as $\frac{1}{2}$, then the 761-keV transition to the $\frac{7}{2}^-$ ground state must be either E3 or M3 since a spin change of three units is involved. The calculated mean-life times for E3 and M3 transitions shown in Table 9 are accurate within two orders of magnitude. Comparing the experimentally determined 11 ± 1 nsec life-time for the 761-keV level with the calculated values reveals that both E3 and M3 transitions have mean-life times that are much larger than the experimentally measured value. For this reason, the $\frac{1}{2}$ spin assignment to the 761-keV level is rejected. For a $\frac{3}{2}$ spin assignment to the level, the 761-keV transition to the $\frac{7}{2}^-$ ground state must be either E2 or M2 since the two levels differ by two units of spin. However, arguments given below show that an M2 transition is parity forbidden and therefore must be eliminated from consideration. Comparing the calculated mean-life time for an E2 transition from this level with the experimentally determined life-time shows good agreement and strongly

supports the $\frac{3}{2}$ spin assignment to the 761-keV level of Cr^{51} .

Since only f- and possibly p-orbitals are involved, the parity for this level is odd and is in agreement with the assumption of the E1 character of the 8.499-MeV capture gamma-ray. Additional support is given by the log ft value of 5.49 (Table 8) for the decay of Mn^{51} to the 761-keV level of Cr^{51} , an allowed transition with no parity change from the odd parity of the ground state of Mn^{51} . It is therefore concluded that the spin and parity assignment for the 761-keV level of Cr^{51} is $\frac{3^-}{2}$.

On the basis that transitions from Mn^{51} to the $\frac{3^-}{2}$ 761-keV level and to the $\frac{7^-}{2}$ ground state of Cr^{51} are both allowed, the spin and parity assignment for the ground state of Mn^{51} can be only $\frac{5^-}{2}$, the result expected from the previous discussion.

The decay of Mn^{51} to the second excited state of Cr^{51} is allowed with a log ft value of 5.14 which means the 1170-keV level of Cr^{51} has a probable spin and parity of $\frac{3^-}{2}$, $\frac{5^-}{2}$, or $\frac{7^-}{2}$. Since capture gamma-rays from thermal neutron studies of Cr^{50} have not been observed for the 1170-keV level, the $\frac{3^-}{2}$ assignment is rejected. The upper-limit for the mean-life of the 1170-keV state is consistent with the conclusion of a $\frac{5^-}{2}$ or $\frac{7^-}{2}$ spin and parity assignment for this level.

In summary, the decay scheme of Mn^{51} has been studied experimentally yielding the following results:

1. A new half-life value of 46.5 ± 0.2 minutes has been measured, a value which compares favorably with only the 46 ± 2 minute half-life reported by Livingood and Seaborg (1938). This comparison is shown in Figure 28 along with the previously determined half-life values.

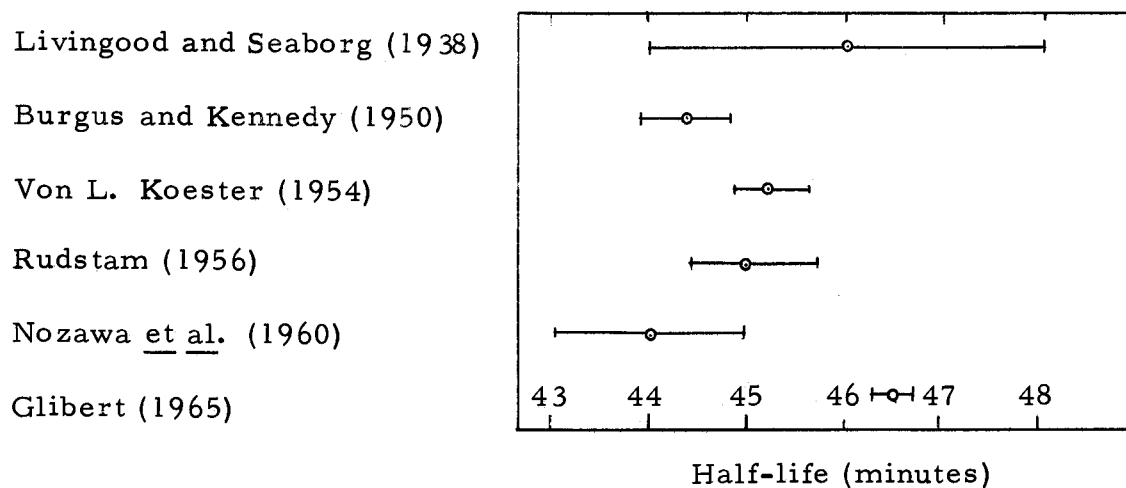


Figure 28. Comparison of experimentally determined half-lives for Mn^{51} .

2. An end-point energy of 2.21 ± 0.02 MeV for the ground state positron transition has been determined which agrees with the experimentally measured values of 2.17 ± 0.05 MeV and 2.16 ± 0.15 MeV given by Baskova et al. (1962) and Koester (1954), respectively. However, in addition to having a smaller error, the numerical value determined in this investigation is in better agreement with the 2.20-MeV value expected from the mass difference of Mn^{51} and

Cr^{51} (Howard, 1963) than the two previously reported end-point energies.

3. Gamma-ray energies of 761 ± 11 keV and 1170 ± 15 keV and corresponding relative intensities of 0.70 ± 0.10 and 0.48 ± 0.12 percent of the positons, respectively, have been measured. The measured 1170-keV gamma-ray energy reported by Nozawa et al. (1960) agrees with the value determined in this investigation. However, their measured 740-keV gamma-ray energy and the estimated relative intensities of 0.4 ± 0.2 and 0.2 ± 0.1 do not agree with the values determined here.
4. A mean-life time of 11 ± 1 nsec has been determined for the 761-keV level of Cr^{51} and an upper-limit of 1 nsec has been given to the 1170-keV level.

Combining these experimental results with theory, spin and parity assignments were given to the low-lying levels of Cr^{51} and to the ground state of Mn^{51} . The $\frac{5-}{2}$ ground state spin and parity assignment for Mn^{51} is not consistent with the $\frac{7-}{2}$ prediction of the simple shell model theory and, therefore, Mn^{51} must be classified as an anomaly along with the isotopes Mn^{55} , Ti^{47} and Cr^{49} .

Improvements are expected to be made in the measurements reported in this investigation in the future with the advanced techniques now being developed. First, enriched Cr^{50} targets

(prohibitive cost for this investigation) should be used to reduce the Mn^{54} contamination and any other impurities which might be present as a result of bombarding natural chromium with deuterons. Second, the gamma-ray energy measurements can be improved by using high-resolution solid state detectors provided the detector efficiency of the present models is increased. An attempt was made to use a Li-drifted Ge-detector in this investigation to measure the gamma-ray energies, but the extremely low detector efficiency did not reveal the low intensity 761-keV and 1170-keV gamma-rays. Similarly, a solid state beta-ray detector could be used in the end-point energy measurement provided it is capable of stopping high-energy positons and its efficiency is increased. The presently available Li-drifted Si-detectors have the undesirable effect of having a high-intensity backscatter component in their response to monoenergetic electrons a factor which cannot be tolerated in the investigation of continuous beta-spectra. The limitations of the electronics in the measurement of the mean-life time for the 1170-keV level of Cr^{51} should be removed in the future with the advances being made with fast solid state circuitry.

BIBLIOGRAPHY

1. Bahn, E. L. et al. 1964. Decay of 20-minute Ag^{115} . Physical Review 136:603-617.
2. Baskova, K. A. et al. 1962. Investigation of some radioactive nuclei in the region of the filled $1f_{7/2}$ shell. Soviet Physics, JETP 15:289-296.
3. Bauer, R. W., J. D. Anderson and L. J. Christensen. 1963. Lifetimes of excited nuclear states using delayed-reaction gamma rays. Physical Review 130:312-319.
4. Beers, Yardley. 1957. Introduction to the theory of error. 2d ed. Reading, Massachusetts, Addison-Wesley. 66 p.
5. Berger, Martin J. and Stephan M. Seltzer. 1964. Tables of energy losses and ranges of electrons and positons. Washington, National Bureau of Standards. 127 p. (National Aeronautics and Space Administration, SP-3012)
6. Bertolini, G., F. Cappellani and A. Rota. 1960. Corrections for backscattering and energy resolution in beta spectroscopy by scintillation detectors. Nuclear Instruments and Methods 9:107-110.
7. Blatt, John M. and Victor F. Weisskopf. 1952. Theoretical nuclear physics. New York, Wiley. 864 p.
8. Bosch, H. E. and T. Urstein. 1963. Nuclear studies by means of beta spectroscopy with scintillation counters. Nuclear Instruments and Methods 24:109-121.
9. Bunker, M. E. and J. W. Starner. 1955. Decay of Ti^{51} and Cr^{51} . Physical Review 97:1272-1275.
10. Burgus, W. H. and J. W. Kennedy. 1950. Chemical effects accompanying the decay of Mn^{51} . Journal of Chemical Physics 18:97-105.
11. Childs, W. J., L. S. Goudman and L. J. Kieffer. 1959. Nuclear spin of Cr^{51} . Bulletin of the American Physical Society 4:151.

12. Eisberg, Robert Martin. 1961. Fundamentals of modern physics. New York, Wiley, 729 p.
13. Evans, Robley D. 1955. The atomic nucleus. New York, McGraw-Hill. 972 p.
14. Everling, F. 1963. Mass and level systematics of $1f_{7/2}$ shell nuclei. Nuclear Physics 47:561-583.
15. Feenberg, Eugene. 1955. Shell theory of the nucleus. Princeton, Princeton University Press. 211 p.
16. Freedman, M. S. et al. 1956. Correction for phosphor back-scattering in electron scintillation spectrometry. Review of Scientific Instruments 27:716-719.
17. Heath, R. L. 1964. Scintillation spectrometry gamma-ray spectrum catalogue. vol. 1. 2d ed. Washington. 264 p. (IDO-16880-1, AEC Research and Development Report, Physics, TID-4500 (31 st ed.))
18. Hoel, Paul G. 1954. Introduction to mathematical statistics. 2d ed. New York, Wiley, 321 p.
19. Howard, Robert A. 1963. Nuclear physics. Belmont, California, Wadsworth. 578 p.
20. Johnson, R. G., O. E. Johnson and L. M. Langer. 1956. Beta spectrum of $C1^{36}$. Physical Review 102:1142-1148.
21. Kane, W. R., N. F. Fiebiger and J. D. Fox. 1962. Coincidence studies of the thermal neutron capture gamma rays of chromium. Physical Review 125:2037-2048.
22. Kennett, T. J. and G. L. Keech. 1963. An anti-coincidence β -ray scintillation spectrometer. Nuclear Instruments and Methods 24:142-148.
23. Koester, Von L. 1954. Bestimmung der Zerfallsenergie einiger leichter Elemente mit Zählrohr-Absorptionsmethoden. Zeitschrift für Naturforschung 9a:104-114.
24. Livingood, J. J., F. Fairbrother and G. T. Seaborg. 1937. Radioactive isotopes of manganese, iron, and cobalt. Physical Review 52:135.

25. Livingood, J. J. and G. T. Seaborg. 1938. Radioactive manganese isotopes. *Physical Review* 54:391-397.
26. Mayer, Maria Goeppert and J. Hans D. Jensen. 1955. Elementary theory of nuclear shell structure. New York, Wiley. 269 p.
27. McCullen, J. D., B. F. Bayman and Larry Zamick. 1964. Spectroscopy in the nuclear $1f_{7/2}$ shell. *Physical Review* 134:515-538.
28. Miller, D R., R. C. Thompson and B. B. Cunningham. 1948. Products of high energy deuteron and helium ion bombardments of copper. *Physical Review* 74:347-348.
29. National Research Council, Nuclear Data Group. 1955 et seq. Nuclear Data Sheets. Washington. various paging.
30. Nozawa, Masao, Hisashi Yamamoto and Yasukazu Yoshizawa. 1960. Search for weak gamma-rays in the positon decay of Mn^{51} . *Journal of the Physical Society of Japan* 15:2137-2139.
31. Owen, G. E. and H. Primakoff. 1948. Relation between apparent shapes of monoenergetic conversion lines and of continuous β -spectra in a magnetic spectrometer. *Physical Review* 74:1406-1412.
32. Owen, G. E. and H. Primakoff. 1950. Relation between apparent shapes of monoenergetic conversion lines and continuous beta-spectra in a magnetic spectrometer. II. Review of *Scientific Instruments* 21:447-450.
33. Palmer, James P. and L. Jackson Laslett. 1950. Application of scintillation counters to beta-ray spectroscopy. Oak Ridge. 69 p. (United States Atomic Energy Commission, ISC-174)
34. Persson, B. 1964. An electron scintillation spectrometer. *Nuclear Instruments and Methods* 27:1-9.
35. Rose, M. E. 1953. The analysis of angular correlation and angular distribution data. *Physical Review* 91:610-615.
36. Russell, H. T. 1960. Isolation of carrier-free Mn^{54} and I^{125} from cyclotron targets. *Nuclear Science and Engineering* 7:323.

37. Schwarcz, Ervin H. 1963. Shell-model study of Mn^{55} .
Physical Review 129:727-732.
38. Siegbahn, K. 1965. Alpha-, beta- and gamma-ray spectroscopy. vol. 1. Amsterdam, North-Holland. 862 p.
39. Sommerfeldt, Raymond Walter. 1964. Perturbed directional correlation in Ta-181. Ph. D. thesis. Corvallis, Oregon State University. 110 numb. leaves.
40. U. S. Department of Commerce. 1952. Tables of the analysis of beta spectra. Washington. 61 p. (National Bureau of Standards, Applied Mathematics Series - 13)
41. Van Patter, D. M. and S. M. Shafroth. 1964. Decay of 78.4 h Zr^{89} and 4.18 min Zr^{89m} . Nuclear Physics 50:113-135.
42. Wapstra, A. H., G. J. Nijgh and R. Van Lieshout. 1959. Nuclear spectroscopy tables. New York, Interscience. 135 p.
43. Weisskopf, V. F. 1951. Radiative transition probabilities in nuclei. Physical Review 83:1073.
44. Zeidman, B., J. L. Yntema and B. J. Raz. 1960. (d, t) reactions on nuclei with $A \approx 60$. Physical Review 120:1723-1730.
45. Zweifel, P. F. 1957. Allowed capture-positron branching ratios. Physical Review 107:329-330.

APPENDICES

APPENDIX I

SOURCE PREPARATION

Sources of Mn^{51} were produced from the $Cr^{50}(d, n)$ reaction by bombarding natural chromium which contains 4.31 percent Cr^{50} (Howard, 1963) with 7-MeV deuterons provided by the Oregon State University cyclotron. Chromium disks 10 mm diameter by 1 mm thick were exposed for 15 minutes to a 20 μ A beam of deuterons. These disks were mounted on stainless steel backings which served as water jackets for the cyclotron probe.

For the determination of the ground state positron end-point energy, the Mn^{51} was removed from the target material after the bombardment by a radiochemical process. The procedure followed here was a carrier-free ion-exchange separation given by Russell (1960) and is described in the following paragraph.

The exposed target material was first dissolved in a minimal amount of 12N HCl after which the solution was boiled to dryness. To the resulting residue, 30 ml of five percent oxalic acid was added and again the solution was boiled to dryness. This latter step was repeated. After the evaporation process in the last step, 50 ml of five percent oxalic acid was added to the residue and again was heated to dissolve the solids. This solution was then filtered

through a 5 mm by 75 mm column of Dowex 50W-X4, 100-200 mesh, strongly acidic, cation exchange resin which had been activated with five percent oxalic acid. In this process the manganese isotope remains in the column of resin while the chromium and any other elements present pass through. The column was then washed with 100 ml of five percent oxalic acid to remove traces of chromium or any additional elements. The oxalic acid was extracted from the column by flushing with 100 ml of distilled water. To release the manganese from the resin, 20 ml of 0.1N HCl was passed through the column. The solution was collected in a small beaker and was heated if necessary to increase the specific activity. In most cases, however, the specific activity was of sufficient strength that heating was not necessary. The extraction of manganese by this method required approximately 60 minutes.

After this separation, the Mn^{51} was liquid-deposited on backings of Au-coated mylar over an area of $\sim 0.3 \text{ cm}^2$ which previously had been wetted with a dilute solution of insulin. Source thicknesses of less than $100 \mu\text{g}/\text{cm}^2$ were obtained with this process.

APPENDIX II

WEIGHTED LEAST SQUARES FIT PROGRAM

It has been well established that the decay of a single radioactive isotope follows the exponential decay law and that a graph of the natural logarithm of the activity or the counting rate $N(t)$ as a function of time yields a linear curve which can be expressed by the following equation.

$$\ln N(t) = \text{const.} - \lambda t \quad (\text{A1})$$

A measure of the slope of the decay curve gives the decay constant λ which is proportional to the half-life of the isotope.

The following discussion pertains to a description of the data analysis in the half-life measurement of Mn^{51} . In this analysis it is desired to fit the relationship

$$\ln N = a + bt \quad (\text{A2})$$

to a set of data points, $\ln N_i, t_i$, by the method of least squares in which each data point is weighted inversely to the square of its standard deviation. The procedure followed here, developed by Rose (1953), is to determine the parameters a and b which minimize the expression

$$\sum_{i=1}^n w_i (\ln N_i - a - bt_i)^2. \quad (\text{A3})$$

The quantity w_i is the weighting factor which in this analysis is just equal to N_i , the counting rate at time t_i . n is the number of observations.

Rose derived the following equations as a consequence of minimizing (A3) with respect to a and b , respectively.

$$a = \frac{\sum_{i=1}^n t_i^2 N_i \sum_{i=1}^n N_i \ln N_i - \sum_{i=1}^n t_i N_i \sum_{i=1}^n t_i N_i \ln N_i}{\sum_{i=1}^n N_i \sum_{i=1}^n t_i^2 N_i - \sum_{i=1}^n t_i N_i \sum_{i=1}^n t_i N_i} \quad (\text{A4})$$

$$b = \frac{\sum_{i=1}^n N_i \sum_{i=1}^n t_i N_i \ln N_i - \sum_{i=1}^n t_i N_i \sum_{i=1}^n N_i \ln N_i}{\sum_{i=1}^n N_i \sum_{i=1}^n t_i^2 N_i - \sum_{i=1}^n t_i N_i \sum_{i=1}^n t_i N_i} \quad (\text{A5})$$

The RMS errors in a and b also developed by Rose (1953) are given by

$$S_a = \left[\frac{\sum_{i=1}^n t_i^2 N_i}{\sum_{i=1}^n N_i \sum_{i=1}^n t_i^2 N_i - \sum_{i=1}^n t_i N_i \sum_{i=1}^n t_i N_i} \right]^{\frac{1}{2}}, \quad (\text{A6})$$

$$S_b = \left[\frac{\sum_{i=1}^n N_i}{\sum_{i=1}^n N_i \sum_{i=1}^n t_i^2 N_i - \sum_{i=1}^n t_i N_i \sum_{i=1}^n t_i N_i} \right]^{\frac{1}{2}} \quad (A7)$$

From these parameters, the half-life and its error are calculated from

$$T = \frac{-0.69315}{b} \quad (A8)$$

$$S_t = \frac{-T S_b}{b} \quad (A9)$$

The program to be described was written to perform the above calculations on an IBM 1620 computer and is compatible with Fortran II. Before discussing the operation of the program, however, an introduction to the nomenclature is in order.

Y(I) - counting rate N_i

YL(I) - natural logarithm of the counting rate N_i

C(I) - time interval t_i

BGD - background counting rate

J - total number of data points to be fit

$$SY = \sum_{i=1}^J Y(I) = \sum_{i=1}^J N_i$$

$$SCTY = \sum_{i=1}^J C(I)Y(I) = \sum_{i=1}^J t_i N_i$$

$$SC2TY = \sum_{i=1}^J C(I)C(I)Y(I) = \sum_{i=1}^J t_i^2 N_i$$

$$SCYYL = \sum_{i=1}^J C(I)Y(I)YL(I) = \sum_{i=1}^J t_i N_i \ln N_i$$

$$SYTYL = \sum_{i=1}^J Y(I)YL(I) = \sum_{i=1}^J N_i \ln N_i$$

D - denominator in (A5) and (A6)

A - corresponds to a in (A4)

B - corresponds to b in (A5)

$$CX = -A/B$$

SA - RMS error in a, see (A6)

SB - RMS error in b, see (A7)

T - half-life from least squares fit, see (A8)

ST - error in half-life value, see (A9)

$$RST = 1/ST^2$$

$$RAT = T/ST^2$$


```

103 FORMAT(5HA  =E14. 6/5HB  =E14. 6/5HCX  =E14. 6/   41
      15HSA  =E14. 6/ 5HSB  =E14. 6)
104 FORMAT(5HRST=E14. 6/5HRAT=E14. 6)                 43
105 FORMAT(5HT  =E14. 6/5HST =E14. 6)                 44
      END

```

The card numbers in the right-hand margin are not part of the program but have been included here for convenience in describing the program operation.

The function of each card or statement is given below.

- Card 1. Comment card. Identifies only the listing.
- Card 2. Sets aside 1200 storage locations for $C(I)$, $Y(I)$, and $YL(I)$, the time intervals t_i , the counting rates N_i , and the logarithm $\ln N_i$, respectively. The program is restricted to a maximum number of four-hundred data points by this card.
- Card 3. Input statement. Reads the first card in the data input which identifies the data. For example, MN-51, JUNE 1, 1964. This identification is limited to a statement of 42 characters and spaces by the FORMAT statement 100, card 38.
- Card 4. Output statement. Prints out the identification statement read in by line 3.
- Cards 5-6. This do-loop generates the time intervals t_i which are denoted by $C(I)$.

- Card 7. Input statement. Reads value for J.
- Card 8. Input statement. Reads value for BGD.
- Cards 9-13. Clears memory locations for SY, SCTY, SC2TY, SCYYL, and SYTYL.
- Cards 14-17. Input do-loop. Reads in the data cards which contain the counting rates N_i , corrects each N_i for the background counting rate, and then computes the natural logarithms of the corrected counting rates.
- Cards 18-23. Do-loop which calculates all the summations which occur in equations (A4), (A5), (A6) and (A7).
- Card 24. Computes D, the denominator in (A4).
- Card 25. Computes A.
- Card 26. Computes B.
- Card 27. Computes CX.
- Card 28. Computes SA.
- Card 29. Computes SB.
- Card 30. Output statement. Prints out the numerical values for A, B, CX, SA, SB.
- Card 31. Computes the half-life T.
- Card 32. Computes the standard deviation ST in the half-life T.
- Card 33. Computes RST.
- Card 34. Computes RAT.

- Card 35. Output statement. Prints out the numerical values for RST and RAT.
- Card 36. Output statement. Prints out the numerical values for T and ST.
- Card 37. Returns the program to statement 1 (card 3) for the analysis of another set of data.
- Cards 38-44. FORMAT statements which control the form of the data input and output.
- Card 45. End of program card.

A sample format of the data input and output is listed below.

Each line represents an IBM card on which this information is punched.

Sample Input

```
MN-51, JUNE 1, 1964
210
0002500.
0923547.
.
.
.
0043066.
```

Sample Output

MN-51, JUNE 1, 1964
 A = 13.770985E 00
 B = -14.905720E-03
 CX = 92.387251E 01
 SA = 19.912163E-05
 SB = 26.283498E-07
 RST = 14.872743E 03
 RAT = 69.161648E 04
 T = 46.502282E 00
 ST = 81.998226E-04

With the results provided by this program, the average values of the half-life and the standard deviation were obtained from the following relations (Beers, 1957).

$$\bar{T} = \frac{\sum_{i=1}^J (T_i / ST_i^2)}{\sum_{i=1}^J (1 / ST_i^2)} \quad (A10)$$

$$\overline{ST} = \frac{\sum_{i=1}^J (T_i - \bar{T})^2 (1 / ST_i^2)}{\sum_{i=1}^J (1 / ST_i^2)} \quad (A11)$$

APPENDIX III

POLYNOMIAL CURVE FITTING

The program described in this section is one in which a polynomial is fit to a set of data points (X_i, Y_i) by the method of least squares where each data point is weighted inversely to the square of its standard deviation. The problem is to determine the coefficients a_0, a_1, \dots, a_n in

$$Y = a_0 + a_1X + a_2X^2 + a_3X^3 + \dots + a_nX^n, \quad (B1)$$

which minimize the relationship

$$\sum_{i=1}^N w_i (Y_i - a_0 - a_1X_i - a_2X_i^2 - a_3X_i^3 - \dots - a_nX_i^n)^2, \quad (B2)$$

where w_i is the weighting factor. In this analysis w_i is equal to Y_i .

In a manner similar to the one used in Appendix II, minimizing (B2) with respect to a_0, a_1, \dots, a_n yields the normal equations from which the coefficients a_0, \dots, a_n can be determined.

$$\begin{aligned}
 a_0 \sum_{i=1}^N w_i &+ a_1 \sum_{i=1}^N w_i X_i + \dots + a_n \sum_{i=1}^N w_i X_i^n = \sum_{i=1}^N w_i Y_i \\
 a_0 \sum_{i=1}^N w_i X_i &+ a_1 \sum_{i=1}^N w_i X_i^2 + \dots + a_n \sum_{i=1}^N w_i X_i^{n+1} = \sum_{i=1}^N w_i Y_i X_i \quad (B3) \\
 &\vdots \\
 a_0 \sum_{i=1}^N w_i X_i^n &+ a_1 \sum_{i=1}^N w_i X_i^{n+1} + \dots + a_n \sum_{i=1}^N w_i X_i^{2n} = \sum_{i=1}^N w_i Y_i X_i^n
 \end{aligned}$$

The function of this program written in Fortran II for an IBM 1620 computer is to solve the above set of simultaneous equations for the coefficients a_0, a_1, \dots, a_n , and once these are determined, to calculate new values of Y_i for each X_i from (B1). The data input for this polynomial curve fit is limited to a maximum of 250 points (X_i, Y_i) to which a polynomial with a degree as high as nine can be fit.

The program begins by finding the best straight line that fits the data. It then fits successively higher order polynomials until the order designated in the input by LAST is reached, or until the value of the standard error of the polynomial fitted is less than TOL, the allowable value of the standard error. When either of these conditions is met, the coefficients a_0, a_1, \dots, a_n and the

calculated values of Y_i along with each X_i are printed out. The output format for the values of (X_i, Y_i) is compatible with the input format for the analysis described in Appendix IV. Therefore, this output can be used directly as input data for the program listed in Appendix IV.

The nomenclature for the polynomial curve fit program is defined below.

Y(I) - Counting rate in channel X(I).

X(I) - Channel number.

A(I, J) - Matrix of coefficients of normal equations.

$$\text{SUMX}(J) = \sum_{i=1}^N w_i X_i^J - 1$$

$$\text{SUMY}(J) = \sum_{i=1}^N w_i Y_i X_i^J - 1$$

TOL - Maximum allowable value of standard error.

LAST - Highest order polynomial to be fit.

MM - First channel number in analysis.

MMM - Last channel number in analysis.

N - Total number of data points being fitted.

NORD - Order of polynomial being fitted.

S1 - Calculated value of Y_i for each X_i as determined from (B1).

$$\text{S2} = \left(\sum_{i=1}^N w_i (Y_i - \hat{Y}_i)^2 \right) / \sum_{i=1}^N w_i \quad \text{Standard error in fit of}$$

polynomial. Here Y_i denotes the observed counting rate and \hat{Y}_i is the calculated value.

S3 = $Y_i - \hat{Y}_i$. Difference between observed and calculated counting rates.

Below is a listing of the polynomial curve fit program. Again, as in Appendix II, each line or card has been given a number only for convenience in describing the program operation.

```

C   POLYNOMIAL CURVE FIT PROGRAM                               1
    DIMENSION X(250), Y(250), A(10, 10), SUMX(19), SUMY(10)   2
  1  READ 5                                                    3
    READ 2, TOL, LAST                                         4
  2  FORMAT(E10.4, I5)                                         5
    PUNCH 5                                                    6
  5  FORMAT(35H IDENTIFICATION OF CURVE )                     7
    READ 22, MM, MMM                                           8
 22  FORMAT(2I5)                                               9
    N=MMM-MM+1                                                10
    DO 40 I=1, N                                              11
 20  READ 21, Y(I)                                           12
 21  FORMAT(F8.0)                                             13
    X(I)=MM+I-1                                               14
 40  CONTINUE                                                 15
 70  SUMX(1)=0.                                               16
    SUMX(2)=0.                                               17
    SUMX(3)=0.                                               18
    SUMY(1)=0.                                               19
    SUMY(2)=0.                                               20
    DO 90 I=1, N                                             21
    SUMX(1)=SUMX(1)+1./Y(I)                                   22
    SUMX(2)=SUMX(2)+X(I)/Y(I)                                23
    SUMX(3)=SUMX(3)+X(I)*X(I)/Y(I)                           24
    SUMY(1)=SUMY(1)+1.                                       25
 90  SUMY(2)=SUMY(2)+X(I)                                     26
    NORD=1                                                    27
 93  L=NORD+1                                                 28
    KK=L+1                                                    29
    DO 101 I=1, L                                            30
    DO 100 J=1, L                                            31
    IK=J-1+I                                                 32
100  A(I, J)=SUMX(IK)                                        33

```

101	A(I, KK)=SUMY(I)	34
	DO 140 I=1, L	35
	A(KK, I)=-1.	36
	KKK=I+1	37
	DO 110 J=KKK, KK	38
110	A(KK, J)=0.	39
	SS=1. /A(1, I)	40
	DO 120 II=2, KK	41
	DO 120 J=KKK, KK	42
120	A(II, J)=A(II, J)-A(1, J)*A(II, I)*SS	43
	DO 140 II=1, L	44
	DO 140 J=KKK, KK	45
140	A(II, J)=A(II+1, J)	46
	S2=0.	47
	DO 160 J=1, N	48
	S1=0.	49
	S1=S1+A(1, KK)	50
	DO 150 I=1, NORD	51
150	S1=S1+A(I+1, KK)*X(J)**I	52
160	S2=S2+(S1-Y(J))*(S1-Y(J))/Y(J)	53
	B=SUMX(1)	54
	S2=(S2/B)**. 5	55
161	IF(NORD-LAST)162, 163, 162	56
162	IF(S2-TOL)163, 163. 171	57
163	PUNCH 41, NORD, TOL, S2, N	58
	41 FORMAT(I 3, 15H ORDER EQUATION/10HTOLERANCE	
	=E14. 7/	59
	115HSTANDARD ERROR=E14. 7/2HN=15/)	60
	DO 164 I=1, L	61
	J=I-1	62
164	PUNCH 42, J, A(I, KK)	63
	42 FORMAT(1HAI2 1H=E14. 7)	64
165	IF(NORD-LAST)166 167, 166	65
166	IF(S2-TOL)167, 167, 171	66
167	DO 169 I=1, N	67
	S1=0.	68
	S1=A(1, KK)	69
	DO 168 J=1, NORD	70
168	S1=S1+A(J+1, KK)*X(I)**J	71
	S3=Y(I)-S1	72
169	PUNCH 43, X(I), Y(I), S1, S3	73
	43 FORMAT(E10. 3, 3XE14. 7, 3XE14. 7, 3XE14. 7)	74
112	IF(NORD-LAST) 170, 173, 173	75
170	IF(S2-TOL)173, 173, 171	76
171	NORD=NORD+1	77

J=2*NORD	78
SUMX(J)=0.	79
SUMX(J+1)=0.	80
SUMY(NORD+1)=0.	81
DO 172 I=1, N	82
SUMX(J)=SUMX(J)+(X(I)**(J-1))/Y(I)	83
SUMX(J+1)=SUMX(J+1)+(X(I)**J)/Y(I)	84
172 SUMY(NORD+1)=SUMY(NORD+1)+X(I)**NORD	85
GO TO 93	86
173 P=1.	87
GO TO 1	88
END	89

The function of each card or group of cards in the operation of this program is discussed below.

- Card 1. Comment card. Identifies only the program listing.
- Card 2. Dimension statement. Provides memory locations for X(I), Y(I), A(I, J), SUMX(I), and SUMY(I).
- Card 3. Input statement. Reads in identification statement, for example, MN-51, JUNE 1, 1964. This statement is limited to 35 characters including spacing.
- Card 4. Input statement. Reads in TOL and LAST.
- Card 5. Format statement. Establishes the form of the input for TOL and LAST.
- Card 6. Output statement. Prints out statement read in by card 3.
- Card 7. Format statement for input and output from cards 3 and 5, respectively.

- Card 8. Input statement. Reads in MM and MMM, the first and last channel numbers in the analysis, respectively.
- Card 9. Format statement for input of MM and MMM.
- Card 10. Calculates the total number of data points using the first and last channel numbers.
- Cards 11-15. Do-loop in which the counting rates $Y(I)$ are read in and the corresponding channel numbers $X(I)$ are calculated. The Format statement is for the $Y(I)$ input.
- Cards 21-26. Calculate the summations present in the normal equations when a first order polynomial is fit. The additional summations which are required in the fit of higher order polynomials are calculated by cards 82-85.
- Card 27. Establishes the order of the polynomial to be fit as unity.
- Cards 28-29. Establishes values for the control parameters L and KK.
- Cards 30-34. Do-loop in which the matrix of coefficients of normal equations is calculated.
- Cards 35-46. Do-loop in which the $a_0, a_1, a_2 \dots a_n$ coefficients in the normal equations are determined.
- Card 47. Clears the memory location for S2.
- Cards 48-55. Do-loop which calculates the standard error S2.

- Card 56. Compares `NORD` the order of the polynomial being fitted with the highest order specified by `LAST` in the input. If `NORD` is not equal to `LAST`, the program continues to the next statement on card 57. If `NORD` is equal to `LAST`, however, the program skips card 57 and proceeds to card 58.
- Card 57. Compares the calculated standard error `S2` with the maximum allowable error `TOL` specified in the input. If `S2` is less than or equal to `TOL`, then the program is directed to card 77, statement 171, where the calculations for the fit of the next higher order polynomial begins.
- Cards 58-74. Output statements. The values for `NORD`, `TOL`, `S2`, `N`, the coefficients $a_0, a_1, a_2, \dots, a_n$ in the normal equations (B3), each channel number `X(I)` along with the observed counting rate `Y(I)` and the calculated counting rate `S1`, and `S3` the difference between `Y(I)` and `S1` are printed out.
- Cards 75-76. Control statements. If the program passes through cards 58-74, then cards 75 and 76 transfer the program to card 87. Otherwise, the program proceeds to card 77.

- Cards 77-86. Calculate the additional summations required for the fit of the next higher order polynomial and then transfer the program back to card 28.
- Cards 87-88. Transfer program to card 3 where a new set of data can be read in and analysed.
- Card 89. End statement required for compiler control.

APPENDIX IV

BACKSCATTER CORRECTION AND KURIE
FUNCTION CALCULATION

The analysis of the Mn⁵¹ beta-spectrum consists of three steps, the first of which fits a polynomial to the experimental spectrum by the method of least squares. In Appendix III this process is described in detail. The second step which allows for the energy response of the detector system determines the true beta-spectrum from the experimentally observed spectrum by a numerical integration process. From the true beta-spectrum the Kurie functions are computed, the third step in the beta-analysis. In this section a program is described which performs the latter two steps. It is written in Fortran IV for an IBM 7094 computer.

The first part of the program pertains to determining the true spectrum. The experimentally measured spectrum is related to the true spectrum by the equation

$$M(E) = \int_0^{E'_{\max}} N(E')R(E, E')dE' \tag{C1}$$

$$\approx \sum N(E'_i)R(E, E'_i)\Delta_i E'$$

where $M(E)$ is the observed counting rate at spectrometer setting E , $N(E')$ is the true energy spectrum, and $R(E, E')$ is the probability that an electron hitting the crystal detector with energy E' will be recorded in the energy interval E to $E + \Delta E$, the same interval in which $M(E)$ is measured. The response function $R(E, E')$ is approximated by

$$R(E, E') = \frac{k + (1 - m) \exp(-(E - E')^2 / a^2)}{kE' + a \sqrt{\pi} - \frac{1}{2} m a \sqrt{\pi}} \quad (C2)$$

and is normalized to unity.

The true spectrum $N(E')$ is determined by a simple iteration process by matching the experimental spectrum $M(E)$ with that calculated from (C1) using suitably selected trial functions $N_1(E)$ and the response function $R(E, E')$. As a zero-order approximation to $N(E')$, $M(E)/\Delta E$ is used and numerical integration yields a new $M_1(E)$. A first approximation to the true spectrum is then obtained by subtracting from the original experimental spectrum the difference between the new $M_1(E)$ and the original $M(E)$,

$$N_1(E)\Delta E = M(E) - [M_1(E) - M(E)]. \quad (C3)$$

This first approximation $N_1(E)$ is put into the integral (C1), the numerical integration is repeated and, as in the first step, a second approximation is obtained. Similarly, higher order approximations

can be made using (C1) and the following relationship which is a generalization of (C3).

$$N_i(E)\Delta E = N_{i-1}(E)\Delta E - [M_i(E) - M(E)] \quad (C4)$$

In the program listed below, the input for the experimentally observed spectrum $M(E)$ is taken as the output from the program described in Appendix III.

Once the true energy spectrum is determined, the final step in the beta-analysis is to calculate the Kurie functions from

$$K(E) = \left[\frac{\eta(E)N(E)}{f(E)(E + m_0 c^2)} \right]^{\frac{1}{2}} \quad (C5)$$

where $\eta(E)$ is the electron momentum in $m_0 c$ units, $f(E)$ is the Fermi function, E is the kinetic energy of the electron, and $N(E)$ is the counting rate in the energy interval E to $E + \Delta E$. Since the Fermi functions $f(E)$ are tabulated as functions of $\eta(E)$ or E and not channel numbers, the counting rate $N(E)$ is computed by linear interpolation from the counting rates $N(C)$ and $N(C + 1)$ in channels C and $C+1$, respectively, which bracket the energy E . A corresponding channel number for E also is calculated.

The remainder of this section pertains to a listing of the program and its nomenclature, and a discussion which describes the function of each card or group of cards. Card numbers have been

included in the listing for convenience in this discussion.

Nomenclature

- E(I) - Electron kinetic energy.
- ZN(I) - Electron momentum in units of $m_0 c$.
- F(I) - Fermi function corresponding to energy E(I).
- X(I) - Channel number.
- Y(I) - Experimentally observed counting rate in channel X(I).
- TRU(I) - Approximated true energy spectrum $N_i(E)$.
- XPER(I) - Calculated experimental spectrum $M_i(E)$.
- MM - First channel number in the beta-analysis.
- MMM - Last channel number in the beta-analysis.
- N - Total number of data points.
- X1 - Channel number for energy calibration.
- Y1 - Energy value in MeV corresponding to channel X1.
- X2 - Channel number for energy calibration.
- Y2 - Energy value in MeV corresponding to channel X2.
- X3 - Coefficient a in $a = a + b \sqrt{E'}$.
- X4 - Coefficient b in $a = a + B \sqrt{E'}$.
- X5 - Numerical value of m and k in equation (C2).
- X6 - Total number of iterations to be performed or the order of approximation desired in determining the true energy spectrum.
- CNT - Control parameter.

- X8 = $\sqrt{\pi}$
- X9 = $\frac{1}{2} X8(2 - X5)$ Part of denominator in (C2).
- ALPHA = $a = a + b \sqrt{E}$ See equation (C2).
- FRAC - Denominator in (C2).
- RATIO - Exponential in (C2).
- R - Slope in energy calibration equation.
- B - Intercept in energy calibration equation.
- C - Calculated channel number corresponding to energy E(I).
- ZNE - Calculated counting rate N(E) corresponding to energy E(I). This is the counting rate used in calculating the Kurie function.
- ZK - Kurie function

Program Listing

```

DIMENSION E(66), ZN(66), F(66), X(250), G(250), TRU(250) 1
DIMENSION XPER(250), NAME(7) 2
00200 FORMAT(1X, 13HENERGY IN MEV, 6X, 17HCALCULATED 3
COUNTS, 4
16X, 15HCHANNEL NUMBER, 6X, 14HKURIE FUNCTION) 5
00023 FORMAT(F6. 1, F6. 3, F6. 1, F6. 3, F6. 3, F6. 3, F6. 4, F6. 1) 6
00024 FORMAT(1H1, 3HX1=, F6. 1/1X, 3HY1=, F6. 3/1X, 3HX2=, 7
F6. 1/ 8
11X, 3HY2=, F6. 3) 9
00209 FORMAT(1X, 3HX3=, F6. 3/1X, 3HX4=, F6. 3/1X, 3HX5=, 10
F6. 4/ 11
11X, 3HX6=, F6. 1) 12
00206 FORMAT(E10. 3, 3X, E14. 7, 3X, E14. 7, 3X, E14. 7) 13
00025 FORMAT(F6. 3) 14
00026 FORMAT(F8. 3) 15
00027 FORMAT(F4. 1)
00028 FORMAT(5X, F6. 3, 13X, F9.0, 13X, F8. 3, 10X, F10. 3)
00029 FORMAT(F3. 0)

```

00022	FORMAT(2I5)	16
00043	FORMAT(E10. 3, 20X, E14. 7)	17
00502	FORMAT(7A5)	18
00602	FORMAT(1H , 7A5)	19
	READ(5, 27)(Z.N(I), I=1, 66)	20
	READ(5, 25)(E(I), I=1, 66)	21
00500	READ(5, 26)(F(I), I=1, 66)	22
00503	READ(5, 502)NAME	23
	WRITE(6, 602)NAME	24
	READ(5, 22)MM, MMM	25
	N=MMM-MM+1	26
00173	READ(5, 23)X1, Y1, X2, Y2, X3, X4, X5, X6	27
	WRITE(6, 24)X1, Y1, X2, Y2	28
	WRITE(6, 209)X3, X4, X5, X6	29
	READ(5, 43)(X(I), Y(I), I=1, N)	30
	READ(5, 29)CNT	31
	PI=3. 14159	32
	X8=SQRT(PI)	33
	X9=X8*(2. -X5)/2.	34
	DO 2 I=1, N	35
00002	TRU(I)=Y(I)	36
	LL=X6	37
	DO 3 L=1, LL	38
00304	DO 4 I 1, N	39
00004	XPER(I)=0.	40
	DN=X(N)	41
	ALPHA=X ³ +X ⁴ *(SQRT(DN))	42
	XPER(N)=(X ⁵ *TRU(N))/(X ⁵ *DN+X ⁹ *ALPHA)	43
	K=N-1	44
	DO 20 I=1, K	45
	J=N-1	46
	DJ=X(J)	47
	ALPHA=X ³ +X ⁴ *(SQRT(DJ))	48
00201	XPER(J)=XPER(J+1)+(X ⁵ *TRU(J))/(X ⁵ *DJ+X ⁹ *ALPHA)	49
	DO 400 I=1, N	50
	DI=X(I)	51
	ALPHA=X ³ +X ⁴ *(SQRT(DI))	52
00400	XPER(I)=XPER(I)+(1. -X ⁵)*(TRU(I))/(X ⁵ *DI+X ⁹ *ALPHA)	53
	DO 401 I=1, N	54
	DI=X(I)	55
	ALPHA=X ³ +X ⁴ *(SQRT(DI))	56
	FRAC=1. / (X ⁵ *DI+X ⁹ *ALPHA)	57
	JJ=3. *ALPHA	58
	DO 401 J=1, JJ	59
	DIFF=J	60

JJJ=I+J	61
RATIO=DIFF*DIFF/(ALPHA*ALPHA)	62
GAUSS=1./(EXP(RATIO))	63
J1=I-J	64
J2=I+J	65
IF(I-J)403, 403, 402	66
00402 XPER(J1)=XPER(J1)+FRAC*(1.-X5)*GAUSS*TRU(I)	67
00403 IF(JJJ.GT.MMM)GO TO 401	68
00404 XPER(J2)=XPER(J2)+FRAC*GAUSS*TRU(I)	69
00401 CONTINUE	70
DO 205 I=1, N	71
00205 TRU(I)=TRU(I)-XPER(I)+Y(I)	72
00202 WRITE(6, 206)(X(I), TRU(I), Y(I), XPER(I), I=1, N)	73
WRITE(6, 200)	74
R=(Y2-Y1)/(X2-X1)	75
B=Y2-R*X2	76
DO 3 I=1, 66	77
C=(E(I)-B)/R	78
FINAL=MMM	79
ZZ=MM	80
IF(ZZ.GT.C)GO TO 3	81
00008 IF(C.GT.FINAL)GO TO 3	82
00210 NLOW=C	83
GLOW=NLOW	84
NLOW=NLOW-MM+1	85
NUP=NLOW+1	86
ZNE=TRU(NLOW)+(C-GLOW)*(TRU(NUP)-TRU(NLOW))	87
ZK=SQRT(ZN(I)*ZNE/(F(I)*(E(I)+.511E+00)))	88
WRITE(6, 28)E(I), ZNE, C, ZK	89
00003 CONTINUE	90
IF(CNT-2.)503, 500, 501	91
00501 STOP	92
END	93

The following specifies the function of each card or group of cards in the program listed above.

Cards 1-2. Dimension statements. Provide adequate memory locations for E(I), ZN(I), F(I), X(I), Y(I), TRU(I), XPER(I), and NAME.

- Cards 3-19. Format statements. Establish form of input and output parameters, and provide captions for data output.
- Card 20. Input statement. Reads in 66 tabulated values of the electron momentum $ZN(I)$.
- Card 21. Input statement. Reads in 66 values of energy $E(I)$ which correspond to $ZN(I)$.
- Card 22. Input statement. Reads in 66 tabulated values of the Fermi function $F(I)$.
- Card 23. Input statement. Reads in comment identifying data, for example, MN-51.
- Card 24. Output statement. Prints out comment read in by card 23.
- Card 25. Input statement. Reads in numerical values for MM and MMM.
- Card 26. Calculates the total number of data points to be considered from MM and MMM.
- Card 27. Input statement. Reads in numerical values for $X1$, $Y1$, $X2$, $Y2$, $X3$, $X4$, $X5$, and $X6$.
- Cards 28-29. Output statements. Print out the numerical values read in by card 27.
- Card 30. Input statement. Reads in N numerical values for $X(I)$ and $Y(I)$. In the beta-analysis of Mn^{51} these data points were supplied from the output of the program

listed in Appendix III.

- Card 31. Input statement. Reads in numerical value for CNT.
- Card 32. Assigns numerical value to PI.
- Card 33. Calculates square-root of PI.
- Card 34. Calculates value for X9.
- Cards 35-36. Do-loop. Establishes as a zero-order approximation that the true spectrum is equal to the experimentally observed spectrum.
- Card 37. Converts value of X6 from fixed point form to integer form.
- Card 38. Beginning of the do-loop in which the true energy spectrum is approximated and the Kurie functions are calculated.
- Cards 39-40. Do-loop. Clears memory locations for XPER(I).
- Cards 41-70. Iteration process in which one approximation to XPER(I) is made.
- Cards 71-72. Do-loop. Calculation of approximation for true energy spectrum using the results of the iteration process indicated by cards 41-70.
- Card 73. Output statement. Prints out values for X(I), TRU(I), Y(I), and XPER(I).
- Card 74. Output statement. Prints out captions listed in Format statement 200, cards 3 and 4.

- Card 75. Calculates numerical value for R.
- Card 76. Calculates numerical value for B.
- Card 77. Beginning of do-loop in which the Kurie functions are computed. Do-loop ends with card 90.
- Card 78. Calculates channel number corresponding to a given energy $E(I)$.
- Card 79. Converts MMM from integer form to fixed point form.
- Card 80. Converts MM from integer form to fixed point form.
- Cards 81-82. Control statements.
- Cards 83-86. Determine the channel numbers $X(I)$ and $X(I-1)$ which bracket the energy $E(I)$.
- Card 87. Calculates the counting rate used in (C5) by linear interpolation.
- Card 88. Calculates Kurie Function for a given energy $E(I)$.
- Card 89. Output statement. Prints out numerical values for $E(I)$, ZNE, C, and ZK.
- Card 90. Continue statement required for do-loop.
- Card 91. Control statement. If CNT=1 the program is transferred to statement 503, card 23, where a new set of data can be entered. However, this data must then use the same set of Fermi functions from the previous analysis. If CNT=2, the program is transferred to statement 500 where a new set of Fermi functions

and data points can be entered. If CNT=3, the program goes to statement 501 which stops the program.

Card 92. Stop statement. Indicates to the computer that no more calculations are to be made.

Card 93. End statement. Required for compiler control.